November 2020

Computational Investigations of Battery Electrolytes

Ke Li

COMPUTATIONAL INVESTIGATIONS OF BATTERY ELECTROLYTES

A Dissertation

Submitted to the Graduate Faculty of the
Louisiana State University and
Agricultural and Mechanical College
in partial fulfillment of the
requirements for the degree of
Doctor of Philosophy

in

The Department of Chemistry

by
Ke Li
B.S., Lanzhou University, 2015
December 2020

Acknowledgments

I would like to express my sincere gratitude to my Ph.D. advisor Professor Revati Kumar, who put forward a lot of valuable opinions on my research, which gave me a goal and direction for writing the dissertation. She always inspires and encourages me to figure out the hidden physicals behind a phenomenon that helps me discover my potential and guide me to be a real scientist. Prof. Kumar's rigorous academic attitude and profound knowledge, unpretentious, and approachable personality has a significant impact on me, and is a role model worth learning in my life!

I am thankful to Professor Christopher G. Arges and Professor Daniel Kuroda for their great suggestions in our collaborative projects. It has been a great experience to work in close collaboration with their experimental group and a great opportunity for me to using theory to explain their experiment phenomenon. I also would like to thank my committee members Prof. Doug Gilman, Prof. Robin L McCarley, Prof. Daniel Kuroda, Prof. Gerald M. Knapp, and all the professors who have taught me. Their probing questions and useful suggestions motivated me to think about the depth of my understanding of problem areas. Their methodical teaching has given me endless enlightenment.

I am grateful to Dr. Rolf David who is always helpful whenever I have any questions. I send my thanks to Dr. Pu Du who guided me a lot when I just joined the computational chemistry field. I also want to thank Visal Subasinghege Don who is always willing to help when I need it. I am thankful to all other my group members and my friends who accompanied me in the last five and half years, thank them for all the useful suggestions and comments for me and thank them for helping me find the information during my research. Thank them for their support and help in my life!

Last but not least, I want to express my appreciation to my parents and my family who showed their support and love in my 5 and a half years in the US. Their altruistic love and encouragement help me overcome the struggles in my life.

Table of Contents

Acknowledgments iii

Abstract vii

Chapter 1. Introduction to Battery Electrolytes 1
1.1. Background 1
1.2. Solvation Structures and Dynamics of Battery Electrolytes 4
1.3. Effect of Salt Concentration on Battery Electrolytes 6
1.4. Previous Studies and Motivation 7
1.5. Computational Study of Electrolytes 8
1.6. Purview of This Dissertation 9

Chapter 2. Molecular Dynamics Simulations 11
2.1. Introduction 11
2.2. Molecular Dynamics Simulation Scheme 12
2.3. Thermostats and Barostats 18
2.4. Periodic Boundary Conditions 19
2.5. Non-Bonded Interactions 20
2.6. Enhanced Sampling 21
2.7. Analysis of Simulation Data 21

Chapter 3. Computational Study of Structure and Dynamics of Glyme Based Electrolytes for Sodium Rechargeable Batteries 25
3.1. Introduction 25
3.2. Computational Methodologies 30
3.3. Results and Discussion 31
3.4. Conclusion 47

Chapter 4. Computational Study of Block Copolymer Electrolytes 48
4.1. Introduction 48
4.2. Computational Methodologies 50
4.3. Results and Discussions 53
4.4. Conclusion 63

Chapter 5. Ionic Conductivity of Nanoconfined Polycation and Polyanion Brushes – A Computational Study 64
5.1. Introduction 64
5.2. Computational Methods 65
5.3. Atomistic Molecular Dynamics Simulation Results 68
5.4. Conclusion 71

Chapter 6. Outlook and Future Directions 72
6.1. Future Work 72

Appendix A. Supplementary Material for Chapter 3 75

Appendix B. Supplementary Material for Chapter 5 82

Appendix C. Publication Agreements and Permissions 84

References 88

Vita 110

Abstract

In this dissertation, the structure and dynamics of battery electrolytes were investigated using atomistic molecular dynamics (MD) simulations. Battery electrolytes play a key role in transporting ions between the cathode and anode. The chemical stability and ionic conductivity of electrolytes influence battery performance. In order to design better electrolytes, one needs an understanding of the relationship between electrolyte structure, dynamics, and bulk properties. To bridge the gap between the macroscopic phenomenon and the hidden molecular physics, in the first project we focused on probing an ether-based electrolyte, chosen for its relevance in sodium-based batteries. Through studying the impact of concentration and glyme chain length in tandem with chelation, we were able to provide insights to develop guidelines for the design of better batteries. Examining the ion transport mechanism behind different glyme systems, we found a non-vehicular triflate hopping mechanism, which is attributed to the high conductivity at high concentration for the diglyme system. In the remaining two projects, we focused on polymer electrolytes and used MD simulations to complement and interpret experimental results. We studied how macromolecular architectures affect the polymer electrolytes' bulk properties from a molecular point of view. Block copolymer electrolytes (BCEs) have better ionic conductivity when compared to their random copolymer electrolytes (RCEs) counterpart and this is caused by the percolated water, which leads to faster ion migration, inside BCEs. Finally, nano-confined polymer electrolyte brushes exhibited excellent ionic conductivity that can be attributed to the low counterion condensation and faster ion transportation caused by a large concentration of water in the charged domains. The manner in which water molecules affect the counterion condensation and ion transport dynamics are also discussed in this dissertation.

Chapter 1. Introduction to Battery Electrolytes

1.1. Background

An electrolyte is a compound that can generate free ions and conduct electricity when in an aqueous or molten state. As an important component of a battery, electrolyte materials have been extensively investigated[1–12] and major developments in this area have favorably impacted performance in battery systems.[13] Lithium-based and sodium-based rechargeable battery technologies have been an intense area of research for many years.[1–12,14,15] Lithium-based batteries have received a widely attention by the scientific communities because of their high energy density,[16] while sodium-based batteries have a cost effective advantage in a large scale energy-storage system since sodium is a cheaper and a more abundant material when compared to lithium.[17–19] In the case of battery electrolytes, there are usually five types of electrolytes, namely, ionic liquids based electrolytes,[4,20] aqueous electrolytes,[5,6] organic electrolytes,[2,7,8,21,22] solid polymer electrolytes[9,10] and inorganic solid electrolytes.[23,24] Those electrolytes have been extensively studied for applications to lithium/sodium-based batteries.

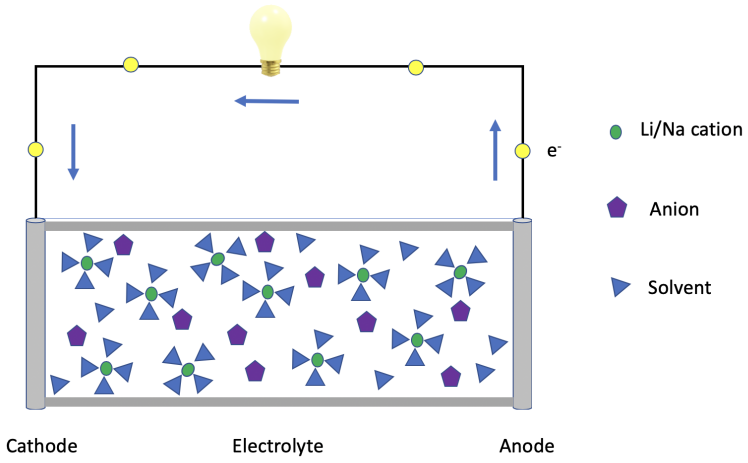

Figure 1.1. Li/Na-based Battery electrolyte

Generally speaking, liquid electrolytes have better ionic conductivity when compared to that of solid electrolytes because liquid electrolytes have better fluidity which means ions in liquid electrolytes have faster migrations.[1] However, it is not only the ionic conductivity of the battery electrolytes that will affect battery performance but also its stability. Solid electrolytes show a excellent thermal stability[11,12,25] and low flammability,[12,25,26] indicating that they are safer. The superior electrochemical stability of solid electrolytes can provide a potentially better battery life.[12,27] For aqueous electrolytes, they exhibit some excellent properties such as low cost, high ionic conductivity, environmental friendliness, good safety, etc.[28–30] However, their practical application is severely restricted by the low energy density of these electrolytes.[31,32]

The use of organic electrolytes is one of the most promising options for the industrial application of battery electrolytes.[1] These electrolytes have many advantages such as a sufficiently high ionic conductivity, excellent compatibility with various electrode materials, stable electrochemical performance and are economic for industrial-scale production.[1,33] Organics electrolytes can be mostly divided into two groups: carbonate-based electrolytes and ether-based electrolytes. Carbonate-based electrolytes usually contains cyclic carbonates (ethylene carbonate (EC), propylene carbonate (PC)) and linear carbonates (ethyl methyl carbonate (EMC), dimethyl carbonate (DMC), and diethyl carbonate (DEC)).[34–37] The most popular ether-based electrolytes are the glyme family such as monoglyme, diglyme, triglyme, tetraglyme, etc.[22,38–42] For lithium-ion batteries, electrolytes with a lithium salt dissolved within a mixture of cyclic and linear carbonates tend to be favored.[43] For example, a mixture of EC and DMC/EMC has been successful in optimizing both the viscosity and electrochemical stability.[27] In the case of sodium-based batteries, ether-based electrolytes

are more favorable to be used because of their nonflammability, chelation effect with sodium ions.[21,44] Kajita et al. have shown that sodium-ion battery electrochemical performance can be significantly improved by replacing the carbonate-based solvent with ether-based solvent.[45] Ionic liquids, which only consist of cations and anions, is a salt in the liquid state below 100 degree Celsius or even at room temperature. Recently these materials have received significant attention as battery electrolytes due to their high thermal stability,[46,47] environmental friendliness[48] and a broad electrochemical stability window.[46,47,49] Although ionic liquids based electrolytes have a lot of advantages, they are not without flaws. The strong Coulombic interactions between the ions increases the viscosity and lowers the conductivity of the electrolytes solution.[1,50] Li et al.[51] have proposed an aqueous rechargeable lithium-ion battery in the mid of the 1990s. The goal is to use greener and safer aqueous-based electrolytes to replace the organic-based electrolytes but their system had poor cycling performance issues. Since then, a lot of progress has been made to enhance the electrochemical performance of the aqueous-based electrolytes battery. For example, Liu et al[52] have proposed a water-in-salt electrolyte which uses a highly concentrated HCOOK solution. This environmental friendly and economic aqueous-based electrolyte provides a high electrochemical stability potential window (about 4V) and a good cycling performance which retains about 64% of the initial capacity after 200 cycles. Although liquid electrolytes based Li/Na batteries are very promising storage systems,[22,53,54] the safety issue caused by the volatile and flammable liquid electrolytes still hinders the applications to large-scale energy storage systems.[1,27] On the other hand, the nonflammability of solid electrolytes makes them more appealing because it can ensure better safety. Solid electrolytes, as previously mentioned, can be divided into two parts: solid polymer electrolytes and inorganic solid electrolytes.

For solid polymer electrolytes, block copolymer electrolytes (BCEs) provide a good solution having both good conductivity and good mechanical properties at the same time.[55–59] Devaux et al.[60] showed that linear polystyrene-poly(ethylene oxide)-polystyrene BCEs present good cycling performance, excellent faradic efficiency and resistance to dendrite growth. In addition, using a lithium metal negative electrode together with solid polymer electrolytes can achieve a high energy densities.[60,61] In the case of inorganic solid electrolytes, the reason why develop them is to address security and reliability issues and enhance energy density.[1] Currently, the main challenges are the solid–solid(electrode and electrolyte) interface compatibility[62,63] and how to obtain high ionic conductivity at room temperature.[23]

1.2. Solvation Structures and Dynamics of Battery Electrolytes

Many electrolyte properties affect the battery performance but there is no doubt that the structures and dynamics play significant roles. A microscopic level understanding of the effect of the interaction between solute and solvent on solvation structures and dynamics can aid in developing design principles for next generation battery electrolytes with better battery performance.

The solvation structures and dynamics of battery electrolytes have been extensively investigated over the last several years and those properties are more likely to be obtained through molecular dynamics (MD) simulations combined with spectroscopic experiments.[2,21,22] For example, a solvent-in-salt system has been investigated by Popov and coworkers.[64] By examining the system of lithium bis(fluorosulfonyl)imide (Li-FSI) and lithium bis(trifluoromethanesulfonyl)imide (Li-TFSI) in water, they highlighted that viscosity is not the only factor that affect the conductivity and that the strong interactions,

which slow down the dynamics for the entire solution, between TFSI anions and the solvent is related to the lower conductivity of $TFSI^-$ system. They concluded that salts with FSI anions would be a better choise for batteries when compared with those with TFSI anions. In addition, the solvation structures of NaTFSI in Dimethyl sulfoxide (DMSO) solution were studied with ab-initio MD simulations coupled with experiments by He et al.[65] The authors have shown that $Na(DMSO)_3(TFSI)$-like solvation structure was formed at high concentrations whcih reduced the available free DMSO molecules. Fewer free DMSO molecules enhance Na electrode and electrolyte stability and hence increase the cycle life, because these free DMSO molecules can react with Na. With the help of solvation structures, we can also obtain counterion condensation of BCEs.[66,67] Counterion condensation is defined as the evaluation of counterions condensed to the polymer backbone.[68,69] The counterion condensation of BCEs was commonly determined from experiments using Manning's Theory in the previous studies,[70–73] however, MD simulations can provide a more intuitive way to examine this property. How counterion condensation impacts ionic conductivity and selectivity in polymer electrolyte membranes have been studied within the past few year.[69,71–76] For example, Kamcev and his coworkers[76] have shown that condensed counterions migrate along the polymer backbone with an external electric field and hence contribute to the conductivity for cross-linked ion exchange membranes. Additionally, they found that condensed counterions diffuse 2-2.5 times faster than those for non-condensed counterions.

1.3. Effect of Salt Concentration on Battery Electrolytes

The optimal salt concentration used in metal-ion batteries has long focused on 1M electrolytes for reasons of optimal performance.[77–79] Owing to the poor ionic conductivity caused by the high viscosity of concentrated electrolytes, they have not been studied in great detail at the beginning. However, recent research on concentrated electrolytes revealed that the high salt concentration electrolytes provide extremely good thermal reactive stabilities[80,81] and even an excellent conductivity(up to 2M).[22]

These researches mostly focused on the how salt concentration affects the solvation structures of the electrolyte and hence affects battery performance. Ravikumar and coworkers investigated how salt concentration affects the lithium-ion battery electrolytes via MD simulations.[78] $LiPF_6$-EC electrolyte system with salt concentration ranging from 0.06 to 4 M has been studied. They found that solvent separated ion pairs were the main structures at low concentrations while contact ion pairs and aggregates are dominant at high salt concentrations. Moreover, the ionic conductivity increases with concentration until 1 M and then decrease. In 2019, Ren et al.[82] have reported a concentrated ether based electrolytes that can work at high voltage (> 4.3 V). They discover a unique cathode electrolyte interphase which is formed by the synergistic reactions between the LiFSI salt and the ether solvent. This interphase has been proven to be effective in reducing the catalytic oxidation of the electrolyte and preserves the cathode structural integrity under high voltages. As a result, this lithium-ion battery can retain 92% of its initial capacity after 500 cycles at high voltage and there is very limited Li consumption at the same time.

1.4. Previous Studies and Motivation

There are abundant reports on the study of battery electrolytes. However, computational studies, especially condensed-phase atomostic MD simulations regarding the trend of ion association for glyme electrolytes, are limited.[2,83] Several studies about gas-phase quantum calculations have been reported. For example, in 2006, Kaulgud et al.[84] have carried out a series of gas-phase ab-initio Hartree-Fock calculations of Li/Na salt in the glyme system. They studied the coordination structure of Li/Na salt in glymes of varying chain lengths. Dhumal et al.[85] studied the cation-anion binding with different glyme chain. They found that the binding weakens as the glyme length increases.

Given the fact that ether-based electrolytes have become very popular candidates for sodium rechargeable battery, Wahlers and coworkers[2] developed a new force-field for the system of soidum triflate in diglyme based on ab-initio MD simulations results using the variational force-matching algorithm[86–88] and they explored how the salt concentration affects the solvation structures and dynamics of the system. They concluded that the accuracy of the new model was validated by Fourier transform infrared (FTIR) experiments and shows excellent transferability between different concentrations. In addition, increasing the salt concentration will change the solvation structures from solvent separated ion pairs to contact ion pairs. How solvation environments (chelation, ion-pairing) change as a function of glyme chain length and salt concentration still need to be resolved. Additionally, whether the new model reported by Wahlers et al. can be transferred to other glymes is unknown. Finally, the ion transport mechanism behind the glyme electrolytes system is also a mystery.

In the case of BCEs, several studies exist comparing the ionic conductivity of ran-

dom/amorphous polymer electrolytes (RCEs) and microphase separated BCEs have been reported.[89–91] For example, Kim et al.[91] presented a BCEs in which ionic conductivity is an order of magnitude higher than that of the random copolymer electrolyte. They ascribed the high ionic conductivity of BCEs to the formation of effective nanoscale ion-conducting channels. However, there is a lack of computational studies regarding to the molecular understanding behind this phenomenon. How water affects the charge transport and how the ion hopping through the polymer backbone have not been revealed.

1.5. Computational Study of Electrolytes

Different approaches can be used to investigate the structure and dynamics of electrolytes systems. Experimental methodologies like Fourier-transform infrared spectroscopy (FTIR),[2,92–94] Two Dimensional infrared spectroscopy (2DIR),[93,95–98] Nuclear magnetic resonance spectroscopy (NMR)[99–102] have been widely used to study electrolytes system. While very informative, it is often hard to tease out specific molecular interactions from these experiments. Simulations can offer both a clear molecular understanding and an interpretation of experimental results.[103] Additionally, for the experiments which are costly, time-consuming, or sometimes difficult to access in the laboratory, performing simulations can be extremely helpful. Hence simulations have become of significant importance in order to understand battery electrolytes system. Simulation can help to interpret the experiments at a molecular level, while the results of the experiments can also validate the accuracy of the simulations. Owing to the mutually beneficial relationship between experiments and simulations, experiments working in tandem with simulations is the trend to explain atomistic insight into the macroscopic behavior of electrolytes systems.

Simulations can be performed in either the gas-phase or the condensed-phase. Gas-phase calculations are usually carried out using quantum mechanics to get optimised geometry,[104,105] partial charge,[104,106] coordination structure,[84,85,107,108] etc. To get the solvation structures and dynamics, condensed phase MD simulations, which account for both enthalpic and entropic contributions, need to be performed. For MD simulations, the interactions between the atoms are ideally described by quantum mechanics, however, it is computationally expensive which limits the accessible time and length scales. Fortunately, one can use simpler and more efficient representation of the intermolecular and intramolecular forces through empirical force-fields,[109–112] which have been parameterized by AIMD results or experimental results, for electrolytes system. Using these force-fields can drastically increase the simulation capacity and lower the cost. For systems for which force-field parameters for the non-bonded interactions have not yet been developed, the parameters can be obtained by fitting to ab initio/quantum data using methods such as force-matching.[86–88]

1.6. Purview of This Dissertation

The focus of the work described in this thesis is to investigate solvation structures and dynamics of electrolytes system using atomistic MD simulation. Chapter 2 introduces the theory of molecular dynamics simulation. The algorithms behind the MD simulations are described. The analysis methods used in the MD simulation are also presented.

In Chapter 3, the transferability of the model, which was developed by Wahlers et al. for diglyme, to glymes of varying length and salt concentration is validated. In addition, the solvation environments, such as chelation effect and ion-pairing, as a function of glyme chain length and salt concentration are also described. Finally, a triflate hopping mechanism, which

involves the making and breaking of ion-pairs and/or aggregates, is proposed to contribute to the conductivity of the Na-triflate in glyme system.

In Chapter 4, my studies focus on how water affects the ion association/dissociation in the BCEs and the difference between block copolymer electrolytes and random copolymer electrolytes. During these investigations, the difference in the counterion condensation between different copolymers, as well as the effect of water connectivity on both counterion condensation and charge transport in these polymer electrolytes are described.

Chapter 5 provides the molecular-level understanding of the difference between nano-confined polymer electrolyte brushes and non-confined polymer electrolyte brushes through molecular dynamics simulations. Through this study, the diffusion coefficient for the condensed ions and the non-condensed ions, couterion condensation, and solvation structure for the ionic groups are presented.

Chapter 2. Molecular Dynamics Simulations

2.1. Introduction

Molecular dynamics (MD) simulations are essentially virtual experiments wherein the atoms of the system are propagated using Newton's equations of motion. Briefly, the force at each time step is evaluated from the potential of interaction between particles and Newton's equation of motion is integrated numerically to give the position of particles in the next time step. The potential of interaction between the particles and the atomic forces is again evaluated from the new positions and Newton's equations are integrated to give the next set of positions and hence the system is propagated in time. It is a deterministic method which means once the positions and velocities of each atom are known, the state of the system can be predicted at any time in the future or the past. Unlike single-point energy calculation and geometric configuration optimization, in MD simulations, the thermal motion of the molecules needs to be considered. The molecules should contain enough thermal energy to cross the potential energy barrier during MD simulations. According to the statistical analysis of the motion of each particle, the various properties of the system can be inferred, such as possible conformations,[113–117] thermodynamic properties,[118–120] transport properties,[121–123] various equilibrium properties,[124–126] spectroscopic properties,[127–129] etc.

Newton's equation of motion is given by

$$F_i = m_i a_i \tag{2.1}$$

$$F_i = -\frac{\partial U}{\partial r_i} \tag{2.2}$$

where F_i is the force acting on atom i, m_i is the mass of atom i and a_i is the acceleration of atom i. U is the total potential energy of the system, r_i is the position of atom i.

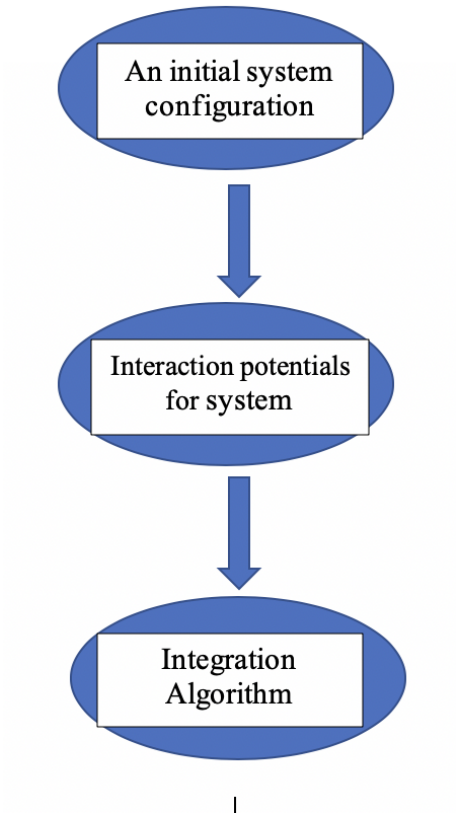

Figure 2.1. MD simulation scheme

2.2. Molecular Dynamics Simulation Scheme

2.2.1. Initial Structures

As shown in Figure 2.1, to start an MD simulation, there are usually three steps. First step is to build the initial configuration for the studying system. In an MD simulation, the initial configuration is of great significance. If the initial structure is further away from its equilibrium state, it will take longer simulation time to get to the equilibrium, which means more computational resources will be used. The initial system configuration contains two-parts, one is coordinates and the other is velocities. The initial coordinates can be generated with the help of Packmol Software.[130] For the initial velocities, the standard approach is to

draw velocities randomly from a Maxwell-Boltzmann distribution at the temperature T.

$$f(v)d^3v = \left(\frac{m}{2\pi k_b T}\right)^{3/2} e^{-\frac{mv^2}{2k_b T}} d^3v \tag{2.3}$$

Where m is the mass of the atom, k_b is the Boltzmann constant, v is the velocity, T is the temperature.

2.2.2. Force-Field

After initializing the system, the second step is to select a force-field which is the interaction potential for the system. Ideally, the potential of interaction and hence the atomic forces (given by the negative gradient of the potential of interaction) should be calculated using quantum mechanics, but the computational expense is prohibitive for system sizes larger than a nanometer and for simulations longer than a few tens of picoseconds. Instead simpler mathematical functional forms, which are functions of the atomic positions, are used to represent the key interatomic interactions. These functions with their associated parameters are referred to as force-fields. Force-field can be effective two-body potentials or can include many-body terms including polarization resulting in greater complexity and hence computational cost. There are three different levels of force-fields with increasing complexity ranging from class I to class III. Class I refers to force-fields with the simplest functional forms while class II and class III are more complex compared to class I force-fields. Most of the time, considering computational efficiency, the force-fields that we use to model our system are class I force fields, such as CHARMM,[131–135] AMBER,[136] OPLS,[111] etc. The potential energy functions in class I force field are primarily harmonic in nature. The intramolecular interactions can be seen from E.Q.(2.4-2.7) and Figure 2.2, while the intermolecular interactions consist of Lennard Jones potential (Van der Waals interactions)

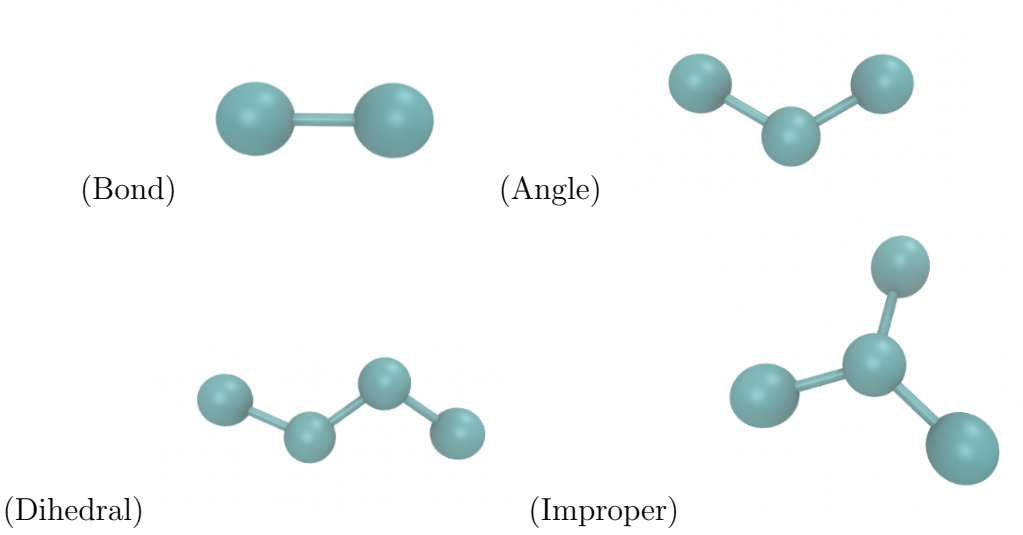

Figure 2.2. Intramolecular Interactions

and electrostatic potential (Coulomb interactions) which is shown in E.Q.(2.8-2.9).

$$E_{\text{bonds}} = \sum_{\text{bonds}} k_b \left(b - b_0\right)^2 \tag{2.4}$$

$$E_{\text{angles}} = \sum_{\text{angles}} k_b \left(\theta - \theta_0\right)^2 \tag{2.5}$$

$$E_{\text{dihedrals}} = \sum_{\text{dihedrals}} \frac{V_n}{2}(1 + \cos n\phi - \psi) \tag{2.6}$$

$$E_{\text{impropers}} = \sum_{\text{impropers}} k_w \left(\omega - \omega_0\right)^2 \tag{2.7}$$

$$E_{\text{LJ}} = 4\epsilon \left[\left(\frac{\sigma}{r}\right)^{12} - \left(\frac{\sigma}{r}\right)^{6}\right] \tag{2.8}$$

$$E_{\text{elec}} = \frac{1}{4\pi\epsilon_0}\frac{q_i q_j}{r_{ij}} \tag{2.9}$$

Class II force-fields, such as PCFF,[137] contain higher-order terms and cross terms in the intramolecular interaction part. These extra parameters and functions can reproduce Potential Energy Surfaces (PES) from quantum mechanics and experimental properties more accurately. The functional terms for class II force-field is shown in E.Q.(2.10-2.13). Class III force-field includes hyperconjugation and polarization effects. For example, AMOEBA,[138]

polarizable versions of CHARMM, AMBER, etc. In this dissertation only class I and class II force-fields are considered.

$$E_{\text{bonds}} = K_2 (r - r_0)^2 + K_3 (r - r_0)^3 + K_4 (r - r_0)^4 \tag{2.10}$$

$$\begin{aligned}
E_{\text{angles}} &= E_a + E_{bb} + E_{ba} \\
E_a &= K_2 (\theta - \theta_0)^2 + K_3 (\theta - \theta_0)^3 + K_4 (\theta - \theta_0)^4 \\
E_{bb} &= M (r_{ij} - r_1) (r_{jk} - r_2) \\
E_{ba} &= N_1 (r_{ij} - r_1) (\theta - \theta_0) + N_2 (r_{jk} - r_2) (\theta - \theta_0)
\end{aligned} \tag{2.11}$$

$$\begin{aligned}
E_{\text{dihedrals}} &= E_d + E_{mbt} + E_{ebt} + E_{at} + E_{aat} + E_{bb13} \\
E_d &= \sum_{n=1}^{3} K_n [1 - \cos (n\phi - \phi_n)] \\
E_{mbt} &= (r_{jk} - r_2) [A_1 \cos(\phi) + A_2 \cos(2\phi) + A_3 \cos(3\phi)] \\
E_{ebt} &= (r_{ij} - r_1) [B_1 \cos(\phi) + B_2 \cos(2\phi) + B_3 \cos(3\phi)] + \\
&\quad (r_{kl} - r_3) [C_1 \cos(\phi) + C_2 \cos(2\phi) + C_3 \cos(3\phi)] \\
E_{at} &= (\theta_{ijk} - \theta_1) [D_1 \cos(\phi) + D_2 \cos(2\phi) + D_3 \cos(3\phi)] + \\
&\quad (\theta_{jkl} - \theta_2) [E_1 \cos(\phi) + E_2 \cos(2\phi) + E_3 \cos(3\phi)] \\
E_{aat} &= M (\theta_{ijk} - \theta_1) (\theta_{jkl} - \theta_2) \cos(\phi) \\
E_{bb13} &= N (r_{ij} - r_1) (r_{kl} - r_3)
\end{aligned} \tag{2.12}$$

$$
\begin{aligned}
E_{\text{impropers}} =& E_i + E_{aa} \\
E_i =& K\left[\frac{\chi_{ijkl} + \chi_{kjli} + \chi_{ljik}}{3} - \chi_0\right]^2 \\
E_{aa} =& M_1\left(\theta_{ijk} - \theta_1\right)\left(\theta_{kjl} - \theta_3\right) + \\
& M_2\left(\theta_{ijk} - \theta_1\right)\left(\theta_{ijl} - \theta_2\right) + \\
& M_3\left(\theta_{ijl} - \theta_2\right)\left(\theta_{kjl} - \theta_3\right)
\end{aligned}
\tag{2.13}
$$

2.2.3. Integration Algorithm

The last step for MD simulation is to select integration algorithm. The potential energy is a function of the atomic positions (3N) of all the atoms in the system. Due to the complicated nature of this function, there is no analytical solution to the equations of motion; they must be solved numerically.

Verlet algorithm

The basic idea of the Verlet algorithm[139] is that the positions (r), velocities (v), and accelerations (a) can be approximated by a Taylor series expansion, one forward and one backward in time (t).

$$r(t + \Delta t) = r(t) + v(t)\Delta t + \left(\frac{1}{2}\right) a(t)\Delta t^2 + \left(\frac{1}{6}\right) a'(t)\Delta t^3 + \mathcal{O}\left(\Delta t^4\right) \tag{2.14}$$

$$r(t - \Delta t) = r(t) - v(t)\Delta t + \left(\frac{1}{2}\right) a(t)\Delta t^2 - \left(\frac{1}{6}\right) a'(t)\Delta t^3 + \mathcal{O}\left(\Delta t^4\right) \tag{2.15}$$

Summing these two equations, one obtains

$$r(t + \Delta t) = 2r(t) - r(t - \Delta t) + a(t)\Delta t^2 + \mathcal{O}\left(\Delta t^4\right) \tag{2.16}$$

This is the basic form of the Verlet algorithm, it can be seen from the equation the error of the algorithm when evolving the system by Δt is the order of Δt^4. One problem of the Verlet

algorithm is that the velocities cannot be generated directly from the equation. Although they are not required to update the position, they are required to calculate the kinetic energy which is the composition of total energy. Testing the conservation of the total energy is one of the most important tests to verify that an MD simulation is proceeding correctly. The velocities can be got from the position by using

$$v(t) = \frac{r(t+\Delta t) - r(t-\Delta t)}{2\Delta t} \tag{2.17}$$

The error of $v(t)$ is not the order of Δt^4 but Δt^2.

Leap-frog Integration Algorithm

The advantage of leap-frog algorithm[140] is that the velocities are explicitly calculated, but they are not calculated at the same time as the positions.

$$r(t+\Delta t) = r(t) + v\left(t+\frac{1}{2}\Delta t\right)\Delta t \tag{2.18}$$

$$v\left(t+\frac{1}{2}\Delta t\right) = v\left(t-\frac{1}{2}\Delta t\right) + a(t)\Delta t + \left(\frac{1}{2}\right)a'(t)\Delta t^2 + \left(\frac{1}{6}\right)a''(t)\Delta t^3 + \mathcal{O}\left(\Delta t^4\right) \tag{2.19}$$

$$v(t) = \frac{1}{2}\left[v\left(t+\frac{1}{2}\Delta t\right) + v\left(t-\frac{1}{2}\Delta t\right)\right] \tag{2.20}$$

Velocity-Verlet Algorithm

In this algorithm, positions, velocities and accelerations at time are obtained from the same quantities at time t in the following way:

$$r(t+\Delta t) = r(t) + v(t)\Delta t + \left(\frac{1}{2}\right)a(t)\Delta t^2 \tag{2.21}$$

$$v(t+\Delta t) = v(t) + \left(\frac{1}{2}\right)[a(t) + a(t+\Delta t)\Delta t] \tag{2.22}$$

The error of $v(t)$ and $r(t)$ are both the order of Δt^3

2.3. Thermostats and Barostats

For a many-body system associated with energy E, the ensemble average is the average over all possible quantum states of the system. The system in this case is not allowed to exchange energy or particles with its environment. This is what we called microcanonical ensemble (NVE). In the circumstance where the system evolution is ergodic the ensemble averages are equivalent to the time averages obtained in the MD simulation.

In order to run MD simulation at other non-NVE statistical ensembles we must introduce a thermostat and barostat. For example, a system in canonical ensemble (NVT) has constant volume (V), fixed atoms number (N) and in thermal contact with heat bath. The initial velocities can be generated from a Maxwell-Boltzmann distribution at the target temperature. Since the temperature of a particle system is related to the time average of the velocity of the particles as shown in E.Q. (2.23), so the most intuitive way to keep the temperature as a constant is to multiply a scaling factor at a certain step. This is a very rough approach, which rescaling on all velocities by the same factor and it is not time reversible, however, there are improved ways for maintaining the temperature like Andersen thermostat[141] and Berendsen thermostat.[142] The former introduces the stochastic collisions method while the latter uses a coupling parameter to an external bath. The most popular and an accurate strategy which is also used in this dissertation is the Nosé-Hoover thermostat[143–145] which introduced by Andersen, Nosé and reformulated by Hoover. It leads to canonical distribution and it is time reversible.

$$\left\langle \sum_{i}^{n} \frac{1}{2} m_i v_i^2 \right\rangle = \frac{3}{2} n k_B T \tag{2.23}$$

Where m_i, v_i are the mass and velocity for atom i respectively, n is the number of the atoms, k_b is the Boltzmann constant, T is the temperature.

The method to maintain a constant pressure is to change its volume for a microscopic system. Instead of scaling the velocity in the thermostat, re-scaling the simulation box size occurs in the presence of a barostat. Many methods used to control the pressure are similar to the ones used in maintaining the temperature. The most common barostats used in the MD simulations are Berendsen barostat[142] and Parrinello-Rahman Barostat.[146]

$$P = \frac{2}{3V}\left\langle \sum_{i}^{n} \frac{1}{2} m_i v_i^2 \right\rangle - \left\langle \frac{dV}{d\mathbf{q}}\mathbf{q} \right\rangle \tag{2.24}$$

Where P is the pressure, V is the Volume and q is the position.

2.4. Periodic Boundary Conditions

Computational resources are still limited to simulate the length and time scales of real experiments until today. Currently, we can simulate up to 10^8 atoms which is a large number in general but also very small in macro perspective ($> 10^{23}$).[147] In addition, the atom in the edge of the simulation box would experience different forces than the other molecules resulting the edge effect. To try and counteract this edge effect and also obtain the bulk properties of the studied system, a simulation cell with periodic boundary conditions need to be used. This means that a "mirror image atom" will move into the simulation box when a "real atom" moves out of the simulation box as can be seen in Figure 2.3. The cutoff value must less than half of the box size to ensure that the real atom cannot see its mirror image atom, so atoms do not interact with multiple image of their neighbors.

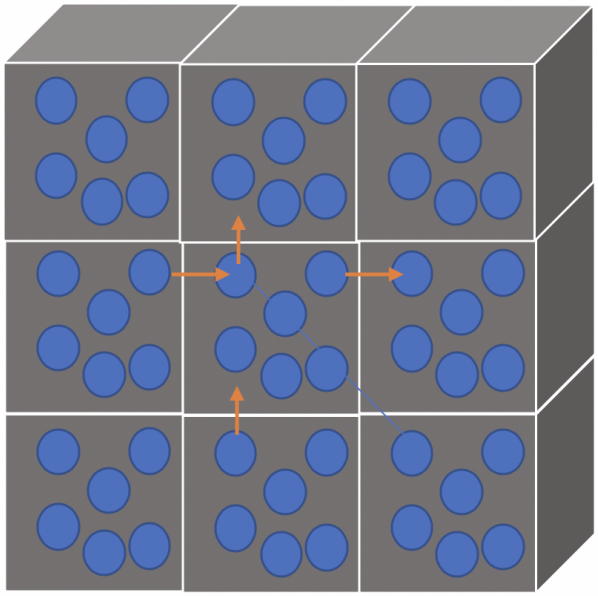

Figure 2.3. Periodic Boundary Conditions

2.5. Non-Bonded Interactions

If we calculated the non-bonded interactions directly, the computational complexity of the direct summation is $O(N^2)$ which is really computational expensive and would be a considerable performance bottleneck for our MD simulations. Therefore, for computer efficiency, non-bonded interactions are usually divided into two parts, one is short range interactions which decrease quicker than r^{-d} (d is the dimension of the system), another is long range interactions. Short range interactions are dealt with by imposing a cutoff to the potential $V(r)$ and $V(r)$ is set to 0 if r is larger than the cutoff value. For long range interaction, specifically long range electrostatic interaction, Ewald Summation, specifically, PPPM (Particle Particle Particle Mesh)[148] is used in this dissertation.

2.6. Enhanced Sampling

Due to the limitation of the hardware and computational resources, the attainable MD time scales is limited to $O(\mu s)$.[147] Thus, the process that requires longer relaxations time ($> \mu s$) is hard to study. Energetically speaking, the system under study can be trapped due to large energy barriers during the simulation process, with the transition an exceedingly uncommon occasion. Enhanced Sampling techniques use artificial biases to speed up sampling of conformational space. There are so many enhanced sampling methods to be used nowadays like umbrella sampling,[149] parallel tempering,[150] metadynamics,[151] etc. Parallel tempering also known as replica exchange MCMC (Markov chain Monte Carlo) sampling is the one mainly used in this dissertation. It uses temperature swaps to accelerate system dynamics at high temperature, so the molecular structures exist in high temperature now can run in low temperature and vice versa. Practically, we run N copies of the system which are randomly initialized at different temperatures and those systems can swap configurations at different temperatures based on the Metropolis criterion. The exchange configurations are accepted with probability p which is shown in E.Q. (2.25).

$$p = \min\left(\begin{array}{c} 1, \\ \end{array} \begin{array}{c} \exp\left(-\frac{E_j}{k_b T_i} - \frac{E_i}{k_b T_j}\right) \\ \exp\left(-\frac{E_i}{k_b T_i} - \frac{E_j}{k_b T_j}\right) \end{array}\right) = \min\left(1, e^{(E_i - E_j)\left(\frac{1}{k_b T_i} - \frac{1}{k_b T_j}\right)}\right) \tag{2.25}$$

2.7. Analysis of Simulation Data

2.7.1. Radial Distribution Function

The radial distribution function (RDF) as shown in E.Q. (2.26) is used to describe how other atoms are located with respect to distance from a reference atom. We usually use the RDF to analyze the solvation structure of our studying system. Moreover, the

coordination number can be obtained form the integration of the RDF as can be seen from E.Q. (2.27).

$$g\left(r_{ij}\right)=\frac{V}{N^{2}}\left\langle \delta\left(r-r_{ij}\right)\right\rangle \tag{2.26}$$

$$n(r)=\int_{0}^{r}4\pi r^{2}\rho g(r)\mathrm{d}r \tag{2.27}$$

Where r_{ij} is the distance between atom i and j, V is the volume, N is the number of atoms and $\delta(r)$ is the Dirac delta function

2.7.2. Diffusion Coefficient

The diffusion coefficient describes the speed of one studying material can diffuse through the system. With higher diffusion coefficient, the diffusion of the studying material will be faster. In MD simulation, there are usually two ways to calculate the diffusion coefficient, one is using velocity-velocity correlation function as can be seen in E.Q. (2.28), another is by implementing mean square displacement.

$$D=\int_{0}^{\infty}\psi\left(t_{d}\right)\quad\psi\left(t_{d}\right)=\frac{1}{3N}\left\langle \sum_{i}^{N}\vec{v}_{i}\left(t_{0}\right)\cdot\vec{v}_{i}\left(t_{0}+t_{d}\right)\right\rangle \tag{2.28}$$

In MD simulations, the mean square displacement (MSD), which can be calculated as E.Q. (2.29), is used to describe the mobility of atoms.

$$\mathrm{MSD}\equiv\left\langle \Delta\overrightarrow{\mathrm{r}}(\mathrm{t})^{2}\right\rangle \equiv\frac{1}{\mathrm{N}}\sum_{\mathrm{i}=1}^{\mathrm{N}}\left(\overrightarrow{\mathrm{r}}_{\mathrm{i}}(\mathrm{t})-\overrightarrow{\mathrm{r}}_{\mathrm{i}}(0)\right)^{2} \tag{2.29}$$

The diffusion coefficient can be obtained from MSD.

$$\mathrm{MSD}=\left\langle \Delta\overrightarrow{\mathrm{r}}(\mathrm{t})^{2}\right\rangle =\mathrm{A}+6\mathrm{Dt}+\text{ fluctuations} \tag{2.30}$$

2.7.3. Orientational Tetrahedral Order Parameter

The orientational tetrahedral order parameter Q, which aims to quantify the tetrahedral solvation structure of water molecules, is a commonly used order parameters.[152–154]

$$q = 1 - \frac{3}{8}\sum_{j=1}^{3}\sum_{k=j+1}^{4}\left(\cos\psi_{jk} + \frac{1}{3}\right)^2 \tag{2.31}$$

Where ψ_{jk} is the angle formed by the lines joining the oxygen atom of a given molecule and those of its 4 nearest neighbors j and k. $q = 1$ for perfectly tetrahedral.

2.7.4. Water Rotational Dynamics

In order to get a holistic picture of what kind of role that water plays in the electrolytes system, an understanding of water, especially its structure and dynamics, is of great importance. With the help of RDF and Tetrahedral Order Parameter, we can have a clear understanding of the structure. The water rotational time-correlation function which is given by $< P_2(\overrightarrow{u(0)} \cdot \overrightarrow{u(t)}) >$ can help us with a better understanding of water rotational dynamics. P_2 is the second Legendre polynomial, and the rotational correlation time is the integral from 0 to ∞ of this time correlation function.[155]

2.7.5. Conductivity

There are usually two ways to calculate ionic conductivity from MD simulation, one is from equilibrium simulation using Nernst-Einstein equation[156] the other is from non-equilibrium simulation via measuring ionic currents.[157] Nernst-Einstein equation is shown in E.Q. (2.32) It states that the ionic conductivity is proportional to the diffusion coefficients and concentration of the ionic species.

$$\sigma_{NE} = \frac{e^2}{VK_BT}\left(N_+ z_+^2 D_+ + N_- z_-^2 D_-\right) \tag{2.32}$$

From non-equilibrium simulation, the conductivity is defined as the magnitude of the current density divided by the magnitude of electric field.

$$\sigma = \frac{I}{A \cdot E} \tag{2.33}$$

Where A is the area perpendicular to the field, I is the current, E is the external electric field. As shown in E.Q. (2.34), the average current flowing across all the system is calculated by linearly fitting the cumulative current that is computed by the integration of the instantaneous current.

$$I(t) = \frac{1}{\Delta t L} \sum_{i=1}^{N} q_i \left[z_i(t + \Delta t) - z_i(t) \right] \tag{2.34}$$

Where z_i is the z coordinate and q_i is the charge of atom i, L is the size of the simulation box and Δt is the time interval used to record data.

Chapter 3. Computational Study of Structure and Dynamics of Glyme Based Electrolytes for Sodium Rechargeable Batteries

3.1. Introduction

Since the first Industrial Revolution, developing and using fossil fuel created unprecedented prosperity for human civilization.[158] On the one hand, people started to use machines instead of hands to produce products, which significantly increased the efficiency of productivity. However, on the other hand, the overuse of fossil fuel not only leads to heavy pollution and global warming but also causes health hazards.[159] In addition, traditional energy resources are non-renewable. The shortage of fossil fuels and the increase in greenhouse gas emissions are one of the main problems that need to be solved with the development of human society.[160] Sustainable energy is not only an effective way to solve environmental problems, but also one of the most important solutions to meet the requirement of energy resources for humans.[161] To make full use of sustainable energy, it is necessary to develop energy storage technology. Among the electrochemical energy storage systems, the lithium-ion battery has received great interest due to its desirable properties and multifunctionality.[162,163] Lithium-ion batteries are dominant in the portable electronic market since the first commercialization, and their triumph is due to their higher energy density in nature compared to the rechargeable system counterparts.[16] Moreover, they are now considered as the most suitable candidates for application in plug-in hybrid electric vehicles or electric vehicles.[164,165] However, they still cannot compete with gasoline-powered engines due to significantly lower energy density,[166] because the capacity of the lithium-ion battery is greatly constrained by

Content in this chapter is published as two articles in The Journal of Physical Chemistry C. [Li, K.; Kankanamge, S. R. G.; Weldeghiorghis, T. K.; Jorn, R.; Kuroda, D. G.; Kumar, R. J. Phys. Chem. C 2018, 122, 9, 4747–4756] and [Kankanamge, S. R. G.; Li, K.; Fulfer, K. D.; Du, P.; Jorn, R.; Kumar, R.; Kuroda, D. G. J. Phys. Chem. C 2018, 122, 44, 25237–25246] reprinted by permission of American Chemical Society.

the materials in the cathode.[167] Furthermore, using existing lithium ion battery technologies for large-scale stationary storage systems is economically not feasible.[54,168] Therefore, it is necessary to develop high energy density batteries and lower the cost. Lithium-air batteries have drawn worldwide attention due to their theoretical ability to store as much energy per volume as gasoline.[169–171] Compared to conventional battery systems that are self-containing, they can capture atmospheric oxygen to use in the cathode reaction instead of storing their own oxidizing agent.[172] However, the formation of lithium peroxide in the cathode will block the porous carbon, and it will lead to large overpotentials.[172] To solve this problem, the use of sodium instead of lithium presents a good solution.[172–175] Although lithium and sodium have similar physical and chemical properties, their respective reactions with oxygen are very different.[176,177] The reaction product between sodium and oxygen is NaO_2 which is very stable, but for lithium the LiO_2 produced is highly unstable.[178] It was found that LiO_2 is only an intermediate species in lithium-air batteries, and after that, it turns into Li_2O_2.[178] Furthermore, NaO_2 is large and will not block the porous carbon cathode.[172,175] Beyond these basic challenges to lithium-air batteries, the biggest advantage of sodium over lithium is its higher global abundance compared to lithium, which makes it is more economic.[17–19] Even though there is an inherently lower energy density for sodium owing to the larger ion size and mass, sodium-air batteries still have a higher energy density than lithium-ion batteries.[19,179] To put it briefly, sodium rechargeable batteries do not merely have a more favorable superoxide formation mechanism compared to lithium-air cells,[172,175,180] they are also plentiful in natural of the essential metal. Hence, it is of considerable importance to further develop sodium rechargeable batteries aiming to reduce fossil fuel use in vehicles as well as build large-scale energy storage systems.

Traditional electrolytes degrade during charge cycling, which makes metal-air batteries hard to recharge.[181] To solve this problem, it is necessary to develop deep insight into the electrolyte charge transport behavior, the nature of the electrolyte/electrode interface, the side reactions during charge cycling, and the factors that influence the electrolyte stability.[182] There are two main electrolytes in use for lithium/sodium-air batteries, one is a carbonate-based electrolyte, and the other is an ether-based electrolyte.[173] In the case of lithium-ion batteries, lithium salts dissolved in mixtures of cyclic and linear carbonates are favored as the electrolytes, owing to their viscosity and electrochemical stability.[183,184] Based on these previous studies on the electrolytes in lithium ion batteries, mixtures of propylene carbonate (PC), ethylene carbonate (EC), diethyl carbonate (DEC), dimethyl carbonate (DMC) and ethyl methyl carbonate (EMC) with a dissolved sodium salts have been studied to optimize the sodium ion battery performance.[34–36,185]Although the investigations have revealed that mixtures of cyclic and linear carbonates produced high bulk conductivity and low viscosity, the reactions between carbonate electrolytes and the electrodes could produce a problematic sodium carbonate which is insoluble. Additionally, these electrolytes easily react with O^{2-} during charge/discharge in sodium-air batteries, resulting in a product like sodium carbonate.[186] Those side reactions will lead to high overpotentials and low energy efficiencies.[172] In an ether-based electrolyte, it has been found that sodium superoxide is favored to be formed reversibly as a crystalline product at very low overpotentials, which minimize the formation of sodium carbonate, moreover, there are fewer side reactions in the ether-based electrolytes.[172,173,187–189]

Given the advantages that ether-based electrolytes have over carbonate-based electrolytes, ether-based solvents provide a bright avenue for designing improved sodium battery

electrolytes. The ether solvents which are focused on today are the glyme family which consists of a varying number of ethylene glycol [$-OCH_2CH_2O-$] in the molecule, starting from monoglyme ($CH_3OCH_2CH_2OCH_3$).[182] From previous studies, in the first solvation shell of sodium salts in the ethers, the coordination numbers for sodium cation with glyme oxygen is around 6 and between 5 and 6 in concentrated crystal solvate structures,[2,188,190] while oxygen coordination around a sodium ion in the case of carbonate solvent is usually below 5.[191] Coordination numbers in the ether-based electrolytes tends to be higher than those for corresponding carbonate-based electrolytes,[34,192] which means there is a stronger binding to the ether. Also, there is a chelating effect between the sodium cation and glyme molecules, which is caused by the stronger coordination. Furthermore, this chelating effect is especially for longer glyme molecules which can wrap around the sodium ion, because the lone pairs electron on the oxygens can donate electron density to the sodium cation.[193] The increasing oxidative stability of the ether-based electrolyte at high salt concentration is the evidence for the electron donation.[194] Moreover, the binding between the sodium ion and ether-based solvent has a significant impact on the performance of sodium-air batteries by forming the ternary graphite intercalation complexes which can be functioned as sodium ion storage in cells.[195–197]

The optimal salt concentration used in metal-ion batteries has long focused on 1M electrolytes. However, some recent studies have shown that salt concentration has a significant impact on the battery's performance.[95,198,199] Lee et al. have shown the use of an ultra-concentrated electrolyte which consists of 5 M sodium bis(fluorosulfonyl)imide in diglyme.[95] This high concentration electrolyte showed excellent electrochemical stability and good cycling performance compared to the low concentration electrolyte. Another research done

recently also showed that even "poor" electrolytes like propylene carbonate show superior performance at high salt concentration (2M) for lithium-ion batteries.[200] Thus, understanding the solvation structures change as a function of salt concentration is highly important. The sodium salt used in this work is sodium triflate, which dissolved in glyme has shown remarkable thermal and cycling stability in sodium rechargeable batteries.[201] The chemical stability of the electrolytes may enhance the battery safety.[201–203] Due to the importance of the chelating effect and the impact caused by salt concentration, one goal of this work is to further explore the role of chelation and concentration on ion association in glyme-based electrolytes. The polymer–consistent force-field (PCFF) was selected to describe the glyme solvent since it has been developed specifically for organic molecules including various glymes and carbonates.[137,204] For pure glyme molecule, both inter- and intramolecular interactions have been parameterized with experimental data which means PCFF is adequate to describe the solvent. However, the original model was obviously not parameterized for the solution of sodium triflate in the glyme molecule. In previous work from my group,[2] the van der Waals parameters for the sodium triflate interactions with other salt moieties as well as with diglyme were determined using a variational force-matching algorithm. Although this force-field was developed specifically for sodium triflate in diglyme, the glyme family all have similar chemical structures, so another goal of this work is to verify the transferability of this model to glymes of varying length. Finally, experiments have also shown that the conductivity of some of these electrolytes increase as a function of concentration.[22] The mechanisms behind this abnormal conduction behavior are investigated in this work. Two different charge transport mechanisms were found through our simulations, namely a traditional vehicular mechanism based on the free ion diffusion and a hopping mechanism

involving the triflate anion.

3.2. Computational Methodologies

3.2.1. Electronic Structure Calculation

The partial charge on each type of glyme molecule was obtained by performing electronic structure calculations on a single glyme molecule. In particular, charges from electrostatic potentials using a grid (CHELPG) method[205] were used to determine atomic charges by fitting to the ab initio electrostatic potential on a grid around the glyme molecule. The reason for using the CHELPG scheme is that the same scheme used to obtain charges for the PCFF force-field and hence was adopted here for consistency. All electronic structure calculations were performed at the MP2 level of theory with D95+(2df, p) basis set using the GAUSSIAN 09 software.[206]

3.2.2. Classical Molecular Dynamics Simulations

The first step in a molecular dynamics simulation is to build the starting structures of the system under study. The initial structures of monoglyme, diglyme, triglyme, tetraglyme, and sodium triflate were built using the Avogadro software.[207] Four cubic simulation boxes were constructed with side length 40 Å for monoglyme, 38 Å for diglyme, 41 Å for triglyme, 45 Å for tetraglyme, and populated using a random packing algorithm in Packmol.[130] For monoglyme, each simulation box contained 360 monoglyme molecules with a varying number of sodium triflate pairs to account for the correct concentration: 19 for 0.5 M, 38 for 1.0 M, 57 for 1.5 M, 76 for 2.0 M. For diglyme, each simulation box contained 230 diglyme molecules with the following number of sodium triflate pairs: 17 for 0.5 M, 34 for 1.0 M, 51 for 1.5 M, 68 for 2.0 M. For triglyme, the simulation box contained 213 triglyme molecules with:

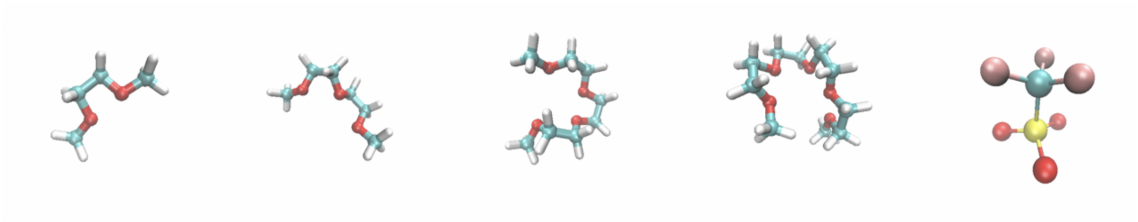

Figure 3.1. The glymes with increasing chain length from monoglyme to tetraglyme are shown followed by the triflate anion. Red corresponds to O atoms, blue to C atoms, yellow to S, pink to F atoms, and white to H atoms.

19 sodium triflate pairs for 0.5 M, 39 for 1.0 M, 58 for 1.5 M, 78 for 2.0 M. For tetraglyme, the simulation box contained 213 tetraglyme molecules with: 29 sodium triflates for 0.5 M, 58 for 1.0 M, 87 for 1.5 M, 116 for 2.0 M. After random packing, each box was equilibrated in the NVT ensemble for 1 ns at a temperature of 300 K, followed by 3 ns simulation in the NPT (temperature of 300 K and pressure of 1 atm) ensemble. The Nose-Hoover thermostat[143–145] and barostat[146] were used. Finally, 30 ns production runs were carried out in the NVE ensemble. All of the above simulations were carried out within the LAMMPS software package[208] under periodic boundary conditions with a 1 fs time step using Ewald, specifically PPPM,[148] to account for long-range electrostatics.

3.3. Results and Discussion

3.3.1. Force-field validation

The transferability of the force-field was validated by comparing two different properties of the system. One property compared is the fraction of ion-pairing, while the other is the diffusion coefficient of the glyme in the salt solutions. The reason for comparing these properties is that the short-range interactions can be validated by ion-pairing while the diffusion constant can take into account the long-range interactions. For ion-pairing, the fraction of free ions was calculated by FTIR experiments carried out in the group of our experimental

Table 3.1. Comparison between experiments and simulations for the solvent dependence of the free ion probability and diffusion constant of the glyme molecules.

Solvent	Fraction of free ions				Diffusion Coefficient $(10^{-10} \cdot m^2 \cdot s^{-1})$	
	1.0 M		1.5 M		1.0 M	
	Exp.	Theory	Exp.	Theory	Exp.	Theory
Monoglyme	0.020±0.005	0	0.010±0.002	0	24.0	33.1
Diglyme	0.29±0.02	0.15	0.25±0.02	0.11	7.6	4.0
Triglyme	0.52±0.02	0.69	0.49±0.02	0.52	2.9	1.0
Tetraglyme	0.46±0.01	0.56	0.44±0.01	0.36	1.6	0.31

collaborator, Dr. Daniel Kuroda,[21] and compared to the results from molecular dynamics simulations in Table 3.1. The probability for the presence of free ions increase from monoglyme to triglyme, and decrease from triglyme to tetraglyme. Both the experimental and simulation results show this trend, and there is very good agreement between them. The average diffusion coefficients of glyme molecules at 1.0 M sodium triflate concentration were obtained from pulse field NMR experiments and compared with results from the simulations. As can be seen from Table 3.1, the diffusion coefficient values from experiment and theory show strong agreement like the ion-pairing, which means not only the local structure but also longer range dynamics are precisely described by this force-field.

3.3.2. Solvation structure

The radial distribution function (RDF) is used to describe how other particles are distributed radially from a reference particle. In this work, we use RDFs to get the local structure surrounding the sodium ions in the different electrolytes. Figure 3.2 shows the RDFs of the local structure around the Na^+ for 1 M solution together with the coordination number. The coordination number is calculated integrating from zero to the first minimum. The first minimum in the RDF defines the first solvation shell. From Figure 3.2, it is easy

to see that the first peak for the $Na-S$ (around 3.6 angstroms) is at a shorter distance than the feature for $Na-C$ (around 4.6 angstroms). This result shows that it is the $-SO_3$ group that coordinates with the sodium ion not the $-CF_3$ group. From the sodium-glyme oxygen RDF, a shift to a smaller value can be seen with the increase of glyme chain length, which means tetraglyme has the strongest binding, while monoglyme has the weakest one. Increasing chain length leads to stronger binding, which means a greater chelation effect and agrees with previous studies.[193] Not only does the change of RDF show the impact of chelation on ion association, but the reported average coordination number also provides further evidence. As seen in sodium-sulfur RDF from Figure 3.2, the coordination number is around 2 in the monoglyme solution which means that there are aggregate structures of multiple ions, however, for diglyme, it drops to around 1 indicating the contact ion pair structures. Finally, it decreases to 0.5 for triglyme and tetraglyme which indicates solvent-separated ions present.

As can be seen from Figure A1 to A4 (Appendix A), the radial distribution functions for sodium ion in different glyme solutions with different salt concentrations show the same general behaviors which have been reported.[2] Table 3.2 contains the average coordination numbers for the first solvation shell around the sodium ion at different concentrations. As shown in Table 3.2, the average coordination number of oxygen atoms (from either the solvent or the anion) is approximately 6 or 7, and it is not affected by the salt concentration or the glyme chain length. This result agrees with previous crystal structures of $glyme-Na^+$ solvates.[190] However, the composition of the sodium's first solvation is greatly influenced by the salt concentration and the glyme chain length. With the increase of salt concentration, the number of triflate anions increase in the average solvation structure resulting a decrease in

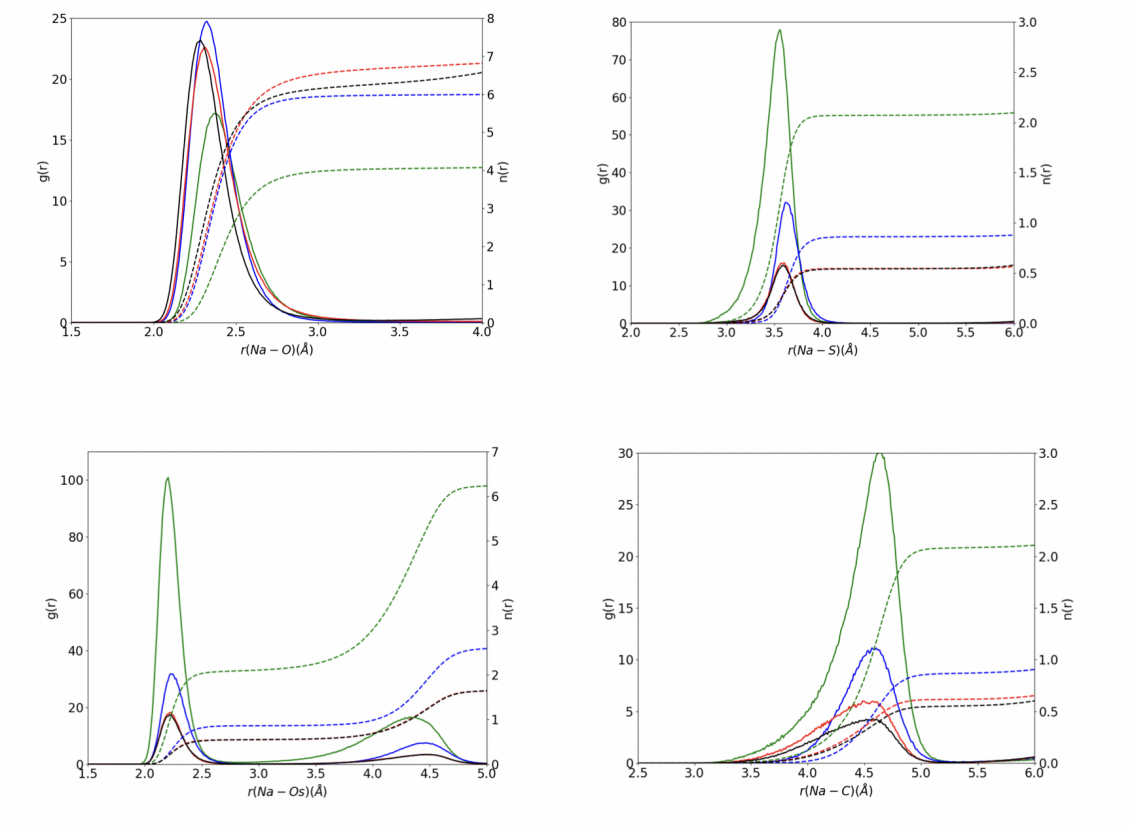

Figure 3.2. Radial distribution functions (solid lines) and coordination numbers (dashed lines) for (a) Na-O (all oxygens from glymes), (b) Na-S (sulfur from triflate), (c) Na-Os (sulfonate oxygen) and (d) Na-C (carbon from triflate) from classical MD simulation at 1.0 M. Green, blue, red, and black lines represent monoglyme, diglyme, triglyme, and tetraglyme, respectively.

the participation of glyme oxygens. This tendency can also be seen in Table 3.3 which shows the relative populations of solvation structure. The change of glyme participation in sodium cation solvation shell is nonlinear, with increasing glyme chain length. From monoglyme to triglyme, the participation of glyme molecules in sodium cation solvation shell increases, but decrease from triglyme to tetraglyme. In the case of triglyme, as shown in Table 3.3 and Figure 3.3, there are two main different structures, one is the solvent separated ion pair (no coordinating anions) the other is aggregate structures ($\geq$ 2 coordinating anions). These solvation structures lead to a large fraction of non-contact ion-pair configurations resulting

from the high participation of triglyme in the first solvation shell. This phenomenon indicates that the solvation structure of sodium ion not only determined by the chelation capacity of the glyme on the sodium ion but steric effect and entropy effect are also essential. More importantly, the solvation structure difference for sodium in triglyme results in the changing of the intercalation properties of sodium-ion batteries.[195] The significant connection between ion solvation structures and battery performance further validates the importance of our method.

Table 3.2. Coordination Number for sodium (Na) ion at different salt concentrations as a function of glyme chain length. O stands for glyme oxygen atoms and Os for triflate oxygen atoms.

Solvent	Conc. (M)	Na^+ coordination number		
		$Na-Og$	$Na-Os$	$Na-S$
Monoglyme	0.5	4.37	1.88	1.86
	1.0	4.06	2.10	2.07
	1.5	3.99	2.14	2.11
	2.0	3.51	2.46	2.43
Diglyme	0.5	6.02	0.80	0.80
	1.0	6.00	0.86	0.86
	1.5	5.85	0.99	0.99
	2.0	5.33	1.38	1.37
Triglyme	0.5	7.39	0.31	0.31
	1.0	6.77	0.62	0.62
	1.5	6.55	0.73	0.74
	2.0	6.05	1.05	1.04
Tetraglyme	0.5	6.41	0.48	0.47
	1.0	6.27	0.55	0.54
	1.5	5.66	0.83	0.81
	2.0	5.49	1.08	1.05

Examining the sodium ion coordination, one can see that only in monoglyme, even at low concentrations (0.5 M), sodium coordinates with one or more triflates. The other glymes always have free ions in solution, which decreases as the concentration of the salt rises. In addition, diglyme shows the largest fraction of one triflate in the first solvation

Table 3.3. Distribution of the number of triflate ions (anion) in the first solvation shell around sodium as a function of glyme chain length and salt concentration.

	Populations (%)			
Anion participation	0	1	2	≥ 3
	0.5 M			
Monoglyme	0	48	41	11
Diglyme	20	80	0	0
Triglyme	85	0	15	0
Tetraglyme	67	23	7	3
	1.0 M			
Monoglyme	0	36	49	15
Diglyme	15	85	0	0
Triglyme	69	0	31	0
Tetraglyme	56	33	10	1
	1.5M			
Monoglyme	0	42	39	19
Diglyme	11	84	1	4
Triglyme	52	0	45	3
Tetraglyme	36	54	6	4
	2.0M			
Monoglyme	0	17	55	28
Diglyme	12	66	2	20
Triglyme	52	0	40	8
Tetraglyme	32	44	18	6

shell at all concentrations as compared to other glyme. When it comes to triglyme, there is a high fraction of free ions in solution, even at high salt concentrations. These results agree with the previous discussion of why the oxygen coordination number for triglyme is higher than that for tetraglyme.

The main solvation structures for sodium triflate in different glymes obtained from MD simulations are listed in Figure 3.3. In the case of monoglyme, there are two main structures at low concentrations: one has sodium coordinated with three monoglyme molecules and two triflate anion, while the other has sodium coordinated to two monoglyme molecules and two triflate anions. As the concentration increases, the proportion of aggregation also

increases, and the solvation structures which contain multiple triflate anion become more obvious. For diglyme, two structures are observed at all concentrations, the main structure is one in which the sodium cation is coordinated by two diglyme molecules and one triflate anion, and the second, in which sodium is just coordinated by two diglyme molecules. With the increase of salt concentration, the fraction of the second structure decreases, and the percentage of the aggregation structure goes up. For triglyme, there are two structures at low concentration, the dominant structure is the one in which sodium ion coordinates with two triglyme molecules, and another where the sodium ion coordinated one triglyme molecule and two triflate anions. With increasing concentration, the percentage of structures in which the sodium ion coordinates with one triglyme molecule and two triflate anions increases. The interesting thing is that there is no structure in which sodium ions coordinate with only one triflate anion. In the case of diglyme; the proportion of sodium cations coordinated by two triflate anions are negligible, while the fraction of sodium cations coordinated with three triflate anions are not. These phenomena match the discussion, in which sodium ions in glymes present a coordination number between 6 and 7 oxygens. Therefore, the configurations either are not seen or can be negligible if they do not meet this requirement. Finally, for the case of tetraglyme, the solvation strctures for sodium triflate in tetraglyme shows that sodium coordinates with one, two, and three triflates even at 0.5 M. The dominant solvation structure is the one where sodium coordinates with two tetraglyme molecules, but as the salt concentration increases, sodium ions coordinated by one tetraglyme and one triflate anion become more significant.

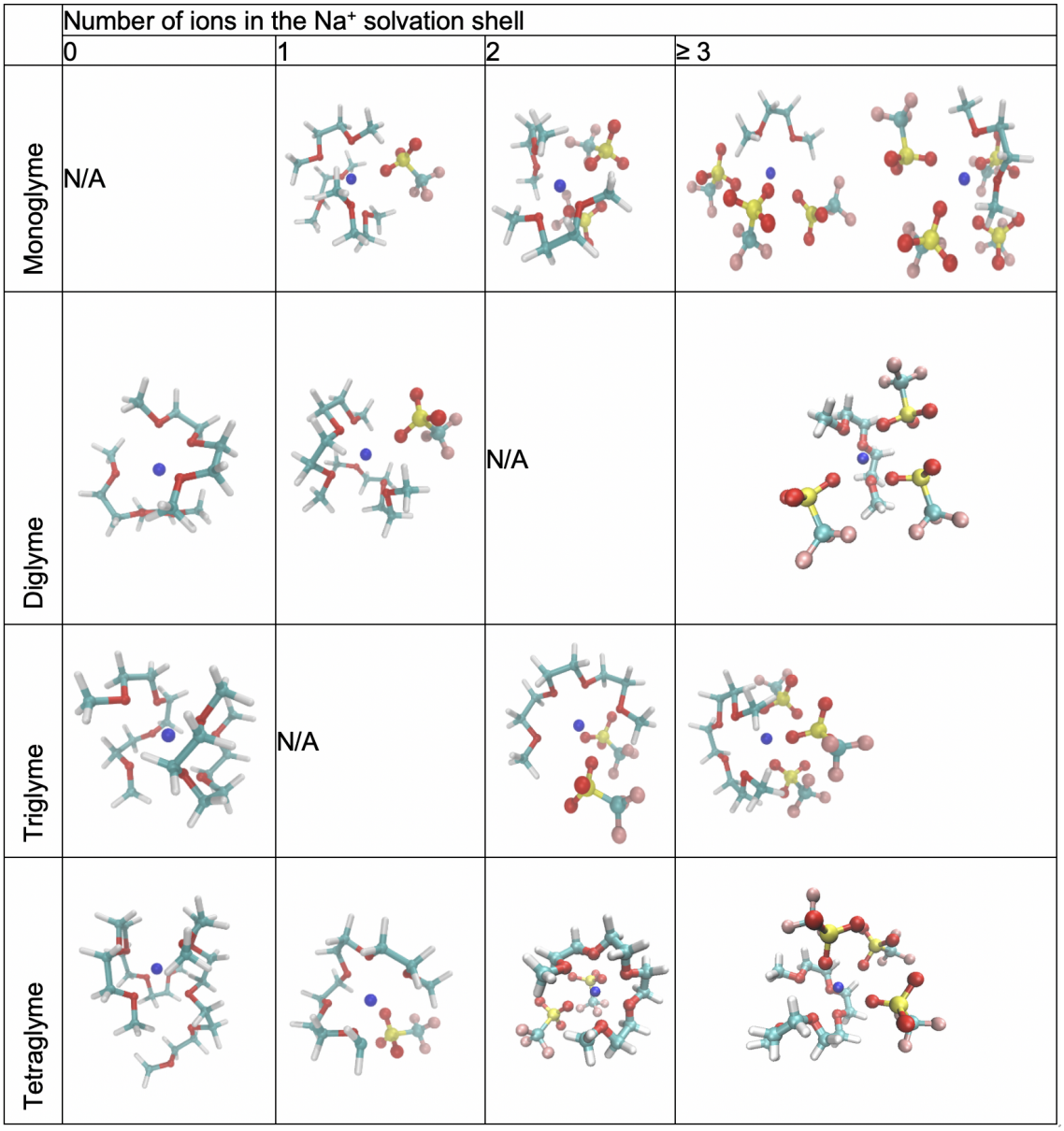

Figure 3.3. Sample solvation for sodium ion in the different glymes. Sodium ion (purple) coordinated by glymes (carbon in black, hydrongen in white, and oxygen in red) and the triflate anion (fluorine in blue, sulfur in yellow, carbon in balck, and oxygen in red).

3.3.3. Diffusion of molecular components

The diffusion coefficients were obtained from the slope of the mean square displacement (MSD) of the center of mass of the glyme molecules, sodium cations, and triflate anions at different salt concentrations. The MSD for those components are shown in A5-A7 (Ap-

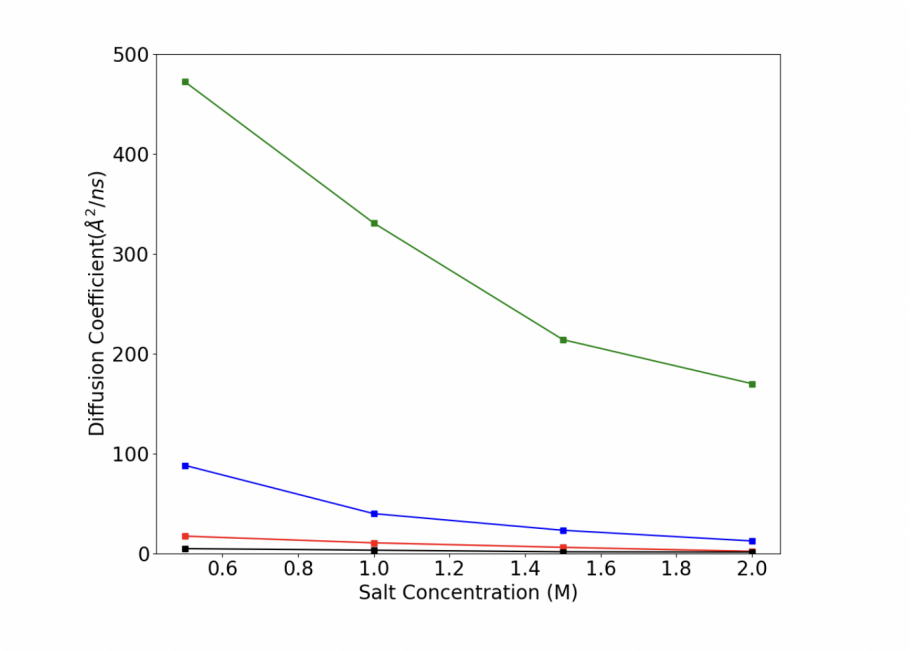

Figure 3.4. Self-diffusion as a function of salt concentration for glyme molecules, monoglyme (green), diglyme (blue), triglyme (red), tetraglyme (black).

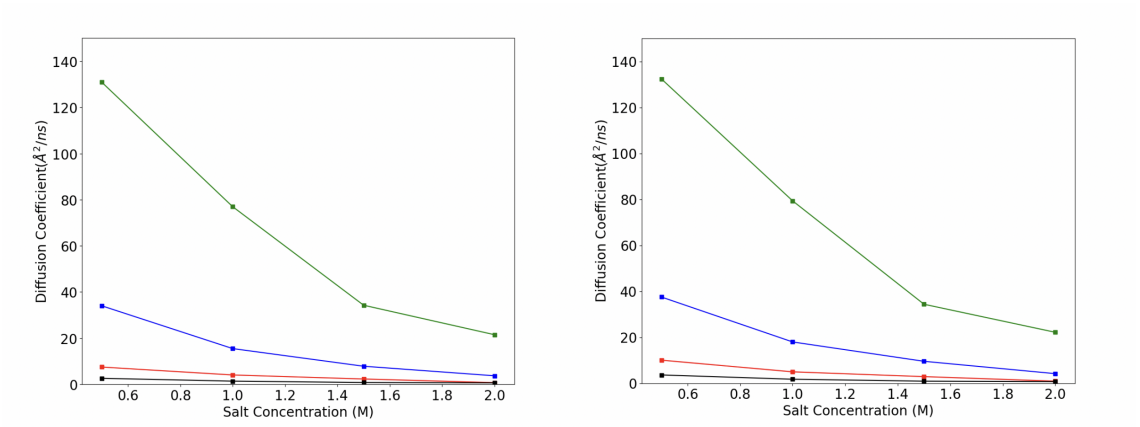

Figure 3.5. (a) Self-diffusion as a function of salt concentration for sodium, monoglyme (green), diglyme (blue), triglyme (red), tetraglyme (black), (b) Self-diffusion as a function of salt concentration for triflate, monoglyme (green), diglyme (blue), triglyme (red), tetraglyme (black).

pendix A), and the diffusion coefficients are shown in Figure 3.4 and Figure 3.5. Owing to the strong interaction between sodium ions and glyme molecules, the self-diffusion coefficient for the glyme molecules decreases with the increasing salt concentrations. This trend also indicates that aggregation will increase the viscosity of the electrolyte. In addition, as the

glyme chain length increased, the diffusion coefficient decreases, which agrees with the size of the molecules. The self-diffusion coefficients of the sodium ion and triflate anions show the same trend as the glyme molecules. However, the diffusion coefficient of glyme molecules is about three times larger than these ionic components. This result indicates that the glyme molecules determine the motion of the electrolyte. Furthermore, the diffusion coefficients of sodium ions and triflate anions are similar, which is in agreement with the large fraction of ion pairing. Finally, the triflate anions diffuse slightly faster than the sodium cations on average. It can be explained by the stronger coordination of the cation, but also indicates that there might be extra movement of the triflate anion.

Table 3.4. Self diffusion constant of the two ions as well as the glyme solvent as a function of salt concentration. Units in $\mathring{A}^2 \cdot ns^{-1}$.

Solvent	Species	0.5 M	1.0 M	1.5 M	2.0 M
Monoglyme	Na	130.89	76.93	34.24	21.46
	Triflate	132.44	79.38	34.44	22.24
	Glyme	472.15	330.56	213.87	169.78
Diglyme	Na	33.98	15.44	7.80	3.66
	Triflate	37.59	18.04	9.63	4.27
	Glyme	88.07	39.67	23.03	12.33
Triglyme	Na	7.44	4.01	2.26	0.68
	Triflate	10.13	5.05	2.97	0.99
	Glyme	17.15	10.45	5.94	1.96
Tetraglyme	Na	2.56	1.33	0.75	0.59
	Triflate	3.71	1.84	0.99	0.79
	Glyme	4.66	3.09	1.46	1.23

3.3.4. Triflate Hopping

Normally as the salt concentration is increased, the viscosity of the solution increases leading to a decrease in conductivity. However, Galle Kankanamge et al.[22] showed that in monoglyme and diglyme conductivity increased with salt concentration (up to 2.0 M) and diglyme exhibits an extraordinary conductivity behavior. Our simulation results show that

the diffusion coefficient of the sodium and triflate ions decreased with the increase of salt concentration for all the glymes under consideration. All of these data suggest that there might be another ion transport mechanism in which ion pairs/aggregates are mostly participated in an exchange behavior. Moreover, this ion exchange phenomenon can contribute to the spatial ion transport resulting in high conductivity. This hypothesis is also revealed by other research group. For example, Okoshi et al.[209] found that the exchange reaction in superconcentrated electrolyte solutions (sodium bis(fluorosulfonyl)amide in monoglyme) for sodium ion battery, and this dissociation/association reactions could play a role in the conduction mechanism.

Examining the simulation data, interestingly but not surprisingly, we found that the sodium ions remain chelated by the same glyme molecules, but the triflate can hop between different sodium solvation shells. A possible explanation for the anomalous increase in conductivity could be the triflate hopping phenomenon which gives rise to non-vehicular contributions to the conductivity. An exchange is considered to take place if the identity of the sodium ion they are coordinated to changes during the time step delta t. The exchange rate is the average number of such changes every nanosecond divided by the simulation box volume. The rate of exchange and fraction show exchange were also calculated for all the four glymes at different concentrations. As can be seen Table 3.5, diglyme shows the highest exchange rate and almost all triflate show the exchange behavior, while triglyme shows the lowest and has the lowest faction of exchange. In addition, the exchange rate increases with increasing concentration except for triglyme, where it starts to plateau at 1.5 M.

A question that can arise is whether the exchange is just back and forth shuttling of the triflate between two sodium ions which in turn will not contribute to the conductivity

Table 3.5. Triflate exchange rate as a function of glyme chain length and salt concentration.

	Glymes Concentration $(mol \cdot L^{-1})$	Fraction show Exchange	Rate $(10^{-6} \cdot ns^{-1} \cdot \mathring{A}^{-3})$
Monoglyme	0.5	0.50	8.2
	1.0	0.47	9.3
	1.5	0.67	29.5
	2.0	0.61	31.1
Diglyme	0.50	1.00	43.3
	1.0	1.00	91.1
	1.5	0.98	101.0
	2.0	0.97	107.3
Triglyme	0.5	0.00	0.0
	1.0	0.26	2.8
	1.5	0.26	8.5
	2.0	0.22	8.2
Tetraglyme	0.5	0.31	3.9
	1.0	0.57	16.5
	1.5	0.62	29.6
	2.0	0.61	38.3

data behavior. Another possibility is that the triflate anion can just shuttle between several coordinating sodium which in turn will also not contribute to conductivity. In order to differentiate simple exchange and shuttling within an aggregate from productive forward hopping, a new definition of hopping is used. Hopping is considered to take place only if the triflate hops to a new solvation shell, with a completely different set of coordinating sodium ions as compared to the previous solvation shell. Moreover, the triflate has to satisfy the condition that it does not go back in the next step to any of the previously coordinating sodium ions in the previous step. These three different kinds of exchange/hopping mechanisms are shown in Figure 3.6. Based on this definition the hopping rate for the different glymes as a function of concentration is shown in Table 3.6.

Monoglyme shows negligible forward hopping despite a non-negligible exchange rate.

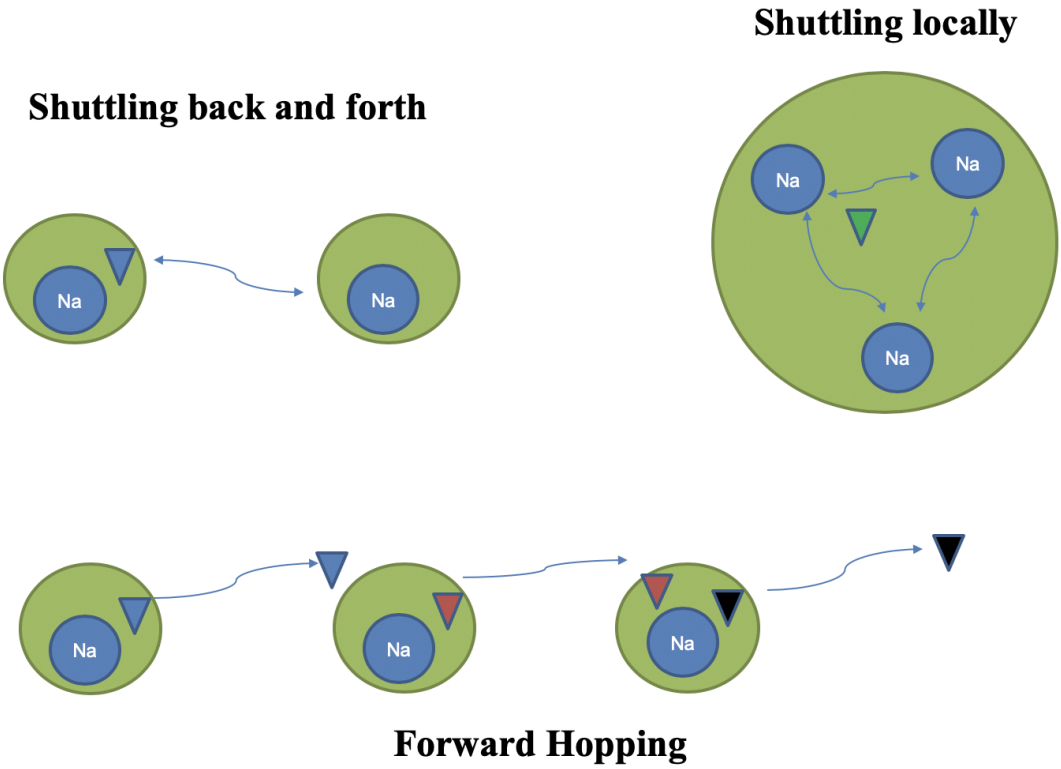

Figure 3.6. Cartoons for different triflate behaviors

Table 3.6. Hopping rate as a function of glyme chain length and salt concentration

Glymes	Monoglyme				Diglyme			
Conc $(mol \cdot L^{-1})$	0.5	1.0	1.5	2.0	0.5	1.0	1.5	2.0
Hopping Rate$(10^{-6} \cdot ns^{-1} \cdot \mathring{A}^{-3})$	0	0	0	0	21.1	32.4	37.0	30.4
Fraction that show hopping	0	0	0	0	0.9	0.8	0.7	0.6
Glymes	Triglyme				Tetraglyme			
Conc$(mol \cdot L^{-1})$	0.5	1.0	1.5	2.0	0.5	1.0	1.5	2.0
Hopping Rate$(10^{-6} \cdot ns^{-1} \cdot \mathring{A}^{-3})$	0	0	0	0	0	0	1.5	1.8
Fraction that show hopping	0	0	0	0	0	0	0.04	0.03

The solvation structure of monoglyme shows significant amount of aggregation with one triflate coordinated to multiple sodium ions and virtually no free triflate. In fact, on closer examination of the simulation trajectories one observes that essentially the triflate anion shuttles between its various coordinating sodium ions which is shown in Figure 3.7. It is quite possible that at longer time scales the triflate anion can hop between different aggregate domains which will explain the why the conductivity increases with the increase of salt concentration in monoglyme, but this is outside the scope of these simulations both in terms of length and time scales.

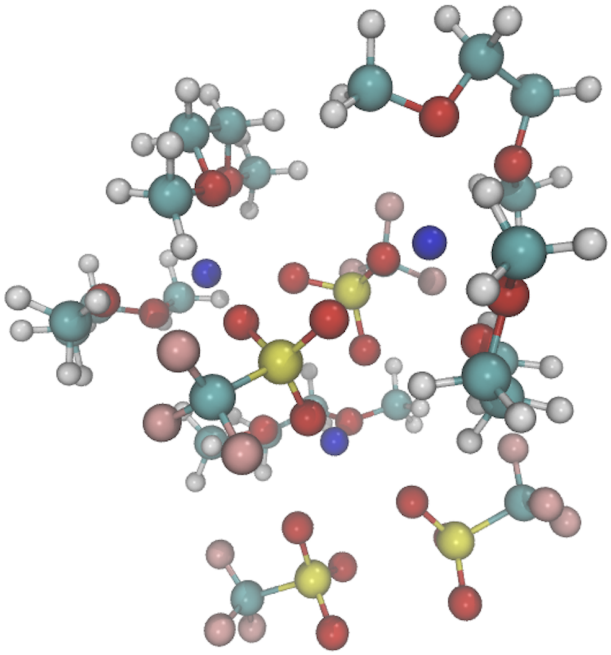

Figure 3.7. Snapshot for aggregate structure wherein the triflate shuttles between different monoglymes, red corresponds to O atoms, blue to C atoms, yellow to S, pink to F atoms, dark blue to Na and white to H atoms

For diglyme, there is significant productive hopping and the mechanism is quite dif-

ferent from monoglyme. It was already seen previously that on average around 20% of the ions are free, namely not coordinated to a counterion and the remaining form contact ion pairs. Analysis of the trajectories indicated that a typical hop involves three distinctive steps (see Figure 3.8). At first, an uncoordinated triflate ion moves into the coordination region of a sodium ion with the simultaneous exit of the triflate that is currently coordinated to the same sodium ion. Following this, the outgoing triflate moves into the coordination shell of the next nearest sodium ion which in turn pushes its triflate ion into the solvent.

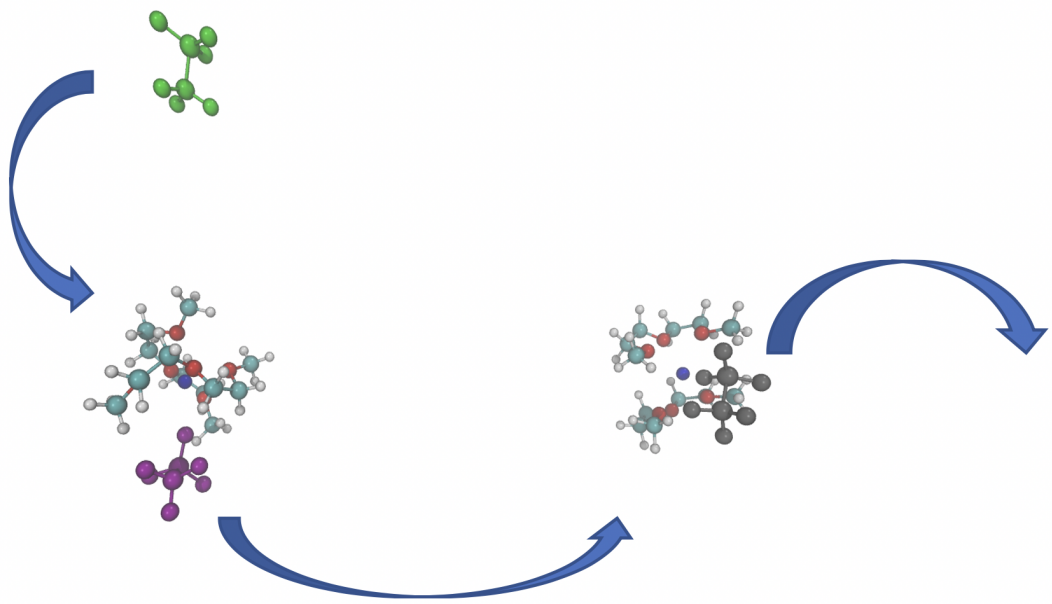

Figure 3.8. Representative triflate hopping in diglyme. Green, purple, black atoms represent three different triflate anions. Red corresponds to O atoms, blue to C atoms, white to H atoms, and dark blue to Na atoms.

For triglyme, most triflate anions did not show hopping and around 20% of triflate anions showed shuttling between sodium ions similar to the case of monoglyme (see Figure 3.9 for a representative structure). In the case of tetraglyme, there is some productive hopping taking place, but the hopping triflate percentage and the hopping rate is much

lower than diglyme.In the case of tetraglyme, there is some productive hopping taking place, but the hopping triflate percentage and the hopping rate is much lower than diglyme. In addition, one does not see multiple sodium ions coordinated to a single triflate.

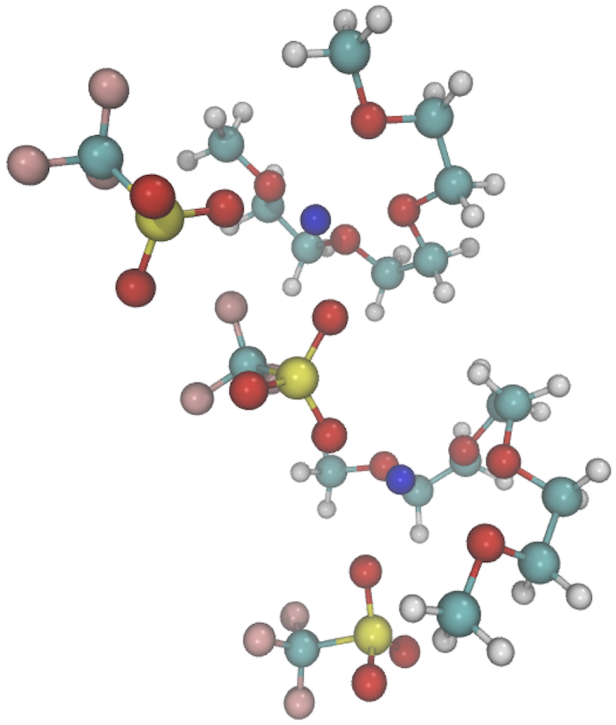

Figure 3.9. Snapshot of an aggregate structure in triglyme that allows triflate shuttling. Red corresponds to O atoms, blue to C atoms, yellow to S, pink to F atoms, dark blue to Na and white to H atoms.

These results provide a molecular explanation for the experimental conductivity data. The non-vehicular diffusion is strongly related to the solvation environment around the charge transport species. Productive hopping requires both contact ion pairs as well as "free" triflate ions that are not coordinated to a counterion. This does indeed suggest that changes in chemical composition of the electrolytes (mixed glymes, different anion, etc.) that result in solvation environments with the above motifs can directly impact charge transport,

thereby leading to design principles for the tailoring of optimal electrolytes.

3.4. Conclusion

The comparison of experiment results and simulation results show that the new model gave a reasonable description of the various glyme-based electrolytes. Therefore, the force-field built specifically for sodium triflate in diglyme is transferable over the glyme family. The solvation structures for sodium ions in different glyme molecules change with the increase in glyme chain length, but not in a linear way. For example, triglyme is an outlier in this respect with a large fraction of free ions in solution even at high salt concentrations. The poor performance of tetraglyme can be explained by its excessive binding tendency to sodium ion. Monoglyme and diglyme show a good potential by allowing for ion association that could prevent glyme molecules being attacked by the superoxide ion produced in the cathode. Finally, monoglyme and triglyme have aggregate structures with multiple sodium coordinated to a single triflate with shuttling of the triflate taking place. Diglyme shows very high productive hopping leading to high conductivity in the concentration range of 0.5-2 M when compared to other glymes.

Chapter 4. Computational Study of Block Copolymer Electrolytes

4.1. Introduction

Polymeric ion-exchange membranes (IEMs), which usually consist of hydrophobic functional parts, immobilized hydrophilic charged functional groups, and movable counterions, have great potential in varieties of applications such as desalination of salty water,[210–212] energy storage and conversion system,[213–215] electrodialysis,[213,216,217] etc. IEMs play significant roles in solving environment and energy related problems.[218] Molecular architectures of polymer electrolytes have a significant impact on the ionic conductivity and mechanical properties of IEMs.[89] Different designs of polymer electrolytes will affect ion selectivity and ionic conductivity and those properties will eventually influence the efficiency of their applications in electrochemical processes.[217] For example, high ionic conductivity will lead to the drop of ohmic overpotential in electrochemical cells and hence improve the thermodynamic efficiency of the batteries.[219] In addition, in electrochemical ion separation processes like desalination, the efficiency of permselectivity for counterions and co-ion exclusion have a significant influence on the current industry application.[217,220,221]

Polymer electrolytes can either be: block copolymer electrolytes (BCEs) or random copolymer electrolytes (RCEs). BCEs have gained significant attention as a subset of the polymeric materials as their ionic domains contribute to the high ionic conductivity and the non-ionic domains provide robust mechanical properties.[55–59,222] Although several studies[72,89,90,223] have shown that BCEs continually demonstrate higher ionic conductivity over their random copolymer counterparts there still a lack of understanding of essential physicals

Content in this chapter is published as one article in Journal of Materials Chemistry A, [Q. Lei, K. Li, D. Bhattacharya, J. Xiao, S. Kole, Q. Zhang, J. Strzalka, J. Lawrence, R. Kumar and C. G. Arges, J. Mater. Chem. A, 2020, 8, 15962] reproduced by permission of The Royal Society of Chemistry.

behind this phenomenon. Counterion condensation and ion transport phenomena in BCEs have aroused the interest of research for many years.[69,71,73,74,224–226] For example, Freeman et al.[73–76,227] have examined how counterion condensation influences ionic conductivity and selectivity in BCEs. They also studied the relationship between the counterion condensation and counterion and co-ion diffusion within BCEs. A lot of progress has been achieved via these studies, however, there are still many questions that remain to be solved such as how does polymer electrolyte morphology affect the ion association and dissociation? How does the water structure within the polymer electrolytes impact counterion condensation and hence influence the material bulk properties like ionic conductivity and selectivity?

Experimentally, poly(styrene-block-2-vinyl pyridine-co-n-methyl pyridinium iodide) and poly(styrene-random-2-vinyl pyridine-co-n-methyl pyridinium iodide) were selected as the BCE and RCE respectively because it was based on the previous works done by Arges and coworkers.[55,223,228] In addition, BCE and RCE has been systematically investigated using multiple experimental techniques including solution uptake using quartz crystal microbalance (QCM), environmental grazing-incidence small-angle X-ray scattering (GI-SAXS) that monitors changes in periodic domain size when the thin film is immersed in salt solutions, and thin film ionic conductivity measurements on interdigitated electrodes (IDEs). QCM and GI-SAXS (only for BCE samples) were used to quantify the extent of counterion condensation in the BCE and RCE thin films.

In this work, to complement the experimental studies, classical molecular dynamics simulations for BCE were performed in this research to obtain counterion condensation and ionic conductivity values. BCEs with different salt concentration ranging from the experimental salt concentrations to the dilute case were investigated to gain the underlying

molecular insight for this charge transport behavior and solvation structures. The simulation results at conditions that are dilute compared to experiments showed a lower fraction of condensed counterions. However, at the same concentrations as the experiment, these simulations showed large extents of counterion condensation, which is similar to what was observed in GI-SAXS and QCM experiments. In addition, to compare the solvation and transport properties between the BCE and the random/non-block case (referred to as RCE), MD simulations for RCE at the same concentrations as the experiment were also deployed. Results from our simulation on counterion condensation, ion migration as well as the water motion revealed that the BCEs display good ion migration due to ion hopping along the chain that is possibly mediated by the percolated water pathway.

4.2. Computational Methodologies

4.2.1. Molecular dynamics simulations

In our work, we used a conventional non-reactive force-filed based on OPLS-AA.[111] The simulations were carried out using the LAMMPS software package[208] under periodic boundary. The cutoff radius for the Lennard-Jones and the real space part of the electrostatic interactions was set to 10 Angstroms. The long-range electrostatic interactions was handled by the Ewald, specifically, particle-particle particle-mesh (PPPM) method.[148] A time step of 1 fs was adopted, and the SHAKE algorithm[229] was used to constrain the bond lengths and bond angles in the water molecules. The model BCE chain, which has three different kinds of monomeric units, were shown in Figure 4.1. The model BCE chain was chosen with a hydrophobic (styrene) segment followed by a hydrophilic segment of equal length. The hydrophilic segment is composed of alternating positively charged n-methyl pyridinium,

hereafter referred to as pyridinium and neutral/unchanged pyridine segments. In the case of RCE, it has 40 monomeric units which are the same as BCE, but it does not have a continuous hydrophobic block part followed by a hydrophilic unlike the BCE case (see Figure 4.1 for a sketch of the two cases). For each tethered positively charged pyridinium moiety, an iodide counterion was introduced. The initial structure of the BCE and RCE was generated consisting of the monomeric units arranged in a trans isomer form using the Avogadro software.[207] For BCE and RCE chains, a short 100 ps simulation of one single chain was performed in vacuum at a temperature of 300 K in the isothermal (NVT) ensemble in a cubic box of length 100 Angstroms at the beginning. Then 30 chains were solvated with water in a cubic box with a box length around 100 Angstroms. The amount of water, which is about 6 waters per pyridinium, was determined based on the solution uptake experiments. In order to study how the salt concentration and water content affect the counterion condensation of BCE, we performed additional simulations. In the extreme case of no added salt and a fully solvated BCE with excess water, one BCE chain was solvated with 6500 water molecules in a cubic box with a box length 60 Angstroms for the dilute case. Finally, we preformed three separate sets of simulations for BCE, with varying amounts of KI salt added and with a ratio of water to KI being 1: 300, 1: 45, 1:20, respectively. The amount of added KI salt were informed from co-ion adsorption experimental data.[67] The water model applied in this study is TIP3P.[230] For all the simulations, after random packing with the help of the Packmol program,[130] each simulation box was energy minimized and subsequently equilibrated for 5 ns in the canonical ensemble (NVT) at a temperature of 300 K followed by 30 ns simulation in the isothermal-isobaric ensemble (NPT) (with a temperature of 300 K and a pressure of 1 atm) via the Nose-Hoover thermostat and barostat.[143–145] To get better sampling, we

carried out replica exchange[231] MD simulations. For each case, the replica exchange/parallel tempering simulations were carried out with 16 replica systems equally distributed between 290 K to 365 K for 20 ns. The structural information were obtained via the trajectories for the 300 K replica. In order to determine dynamical data, the final structures from the parallel tempering simulations at 300K were used to carry out production runs of length 20 ns in the NVT ensemble. Additionally, to obtain the conductivity of the copolymer electrolyte, non-equilibrium MD simulations were performed by adding an electric field of 0.1 V/$\AA$ in the z-direction for 20ns.

Table 4.1. Details of simulated systems

No. of chains	No. Water molecules	No. KI	Temperature (K)
30 BCE	1800	0	300
30 BCE	1800	6	300
30 BCE	1800	40	300
30 BCE	1800	90	300
1 BCE	6500	0	300
30 RCE	1800	0	300

4.2.2. Electronic structure calculations

In order to determine the partial charge on the atomic sites of the polymer for use in the MD simulations, electronic structure calculations on a single repeating unit of the polymer electrolyte were carried out in each case. In particular, charges from electrostatic potentials using a grid (CHELPG) method[205] were used to determine atomic charges by fitting to the ab-initio electrostatic potential on a grid around the polymer electrolyte unit molecule. The CHELPG scheme was chosen to maintain consistency with the OPLS-AA force-field. All electronic structure calculations were performed at the HF/6-31G* level

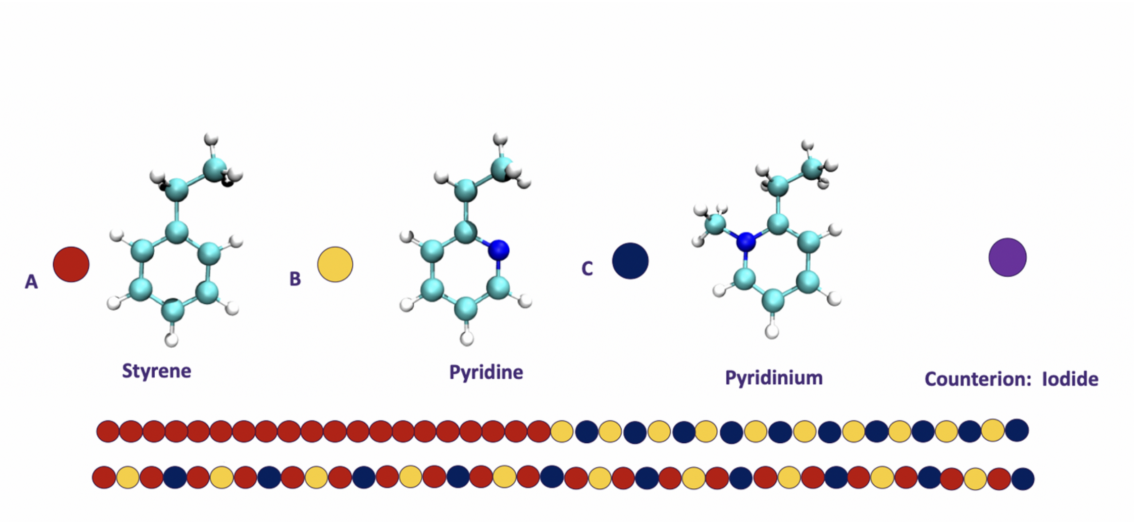

Figure 4.1. The model BCE (first chain) and RCE (second chain) with the different chemical groups.

using the Gaussian 09 software.[206]

4.3. Results and Discussions

The MD simulations determined the extent of counterion condensation by ion-pairing. The ion-pairing of the mobile iodide counterion with the tethered charge on the polymer chain was examined using the iodide ion and the carbon atom (C in the $-CH_3$ group attached to N) radial distribution function. The first minimum in this radial distribution function defines the first solvation shell of pyridinium ions around an iodide ion. If the distance is less than this cutoff the iodide ion is considered to be condensed. The fraction of condensed ion is shown in Table 4.2. MD simulations revealed that about 90 % of the iodide ion are condensed. GI-SAXS experiments and solution uptake experiments done by Dr. Christopher Arges's group who is our collaborator showed that the fraction of condensed counterion is about 97 %. Moreover, this large fraction of condensed counterions is further evidenced by the low activity of coefficients of ions in the BCEs observed from experiments. In addition, the added salt has an effect on the ratio of iodide ions that are coordinated to

the tethered positive charge to the total number of pyridinium moieties. The ratio increases with the increase in salt concentration. This indicates that there are iodide ions from KI salt condensed to the BCE chain. This is an important observation from MD simulations, because Manning's model,[69] which is the theory that experiments based on, assumes that all counterions from adsorbed salt are not condensed. Finally, as shown in Figure 4.3, there is no significant impact on the number of waters coordinated with I^- and K^+ with increase in salt concentration and, as expected, increasing the salt concentration decrease the number of waters coordinated with pyridinium.

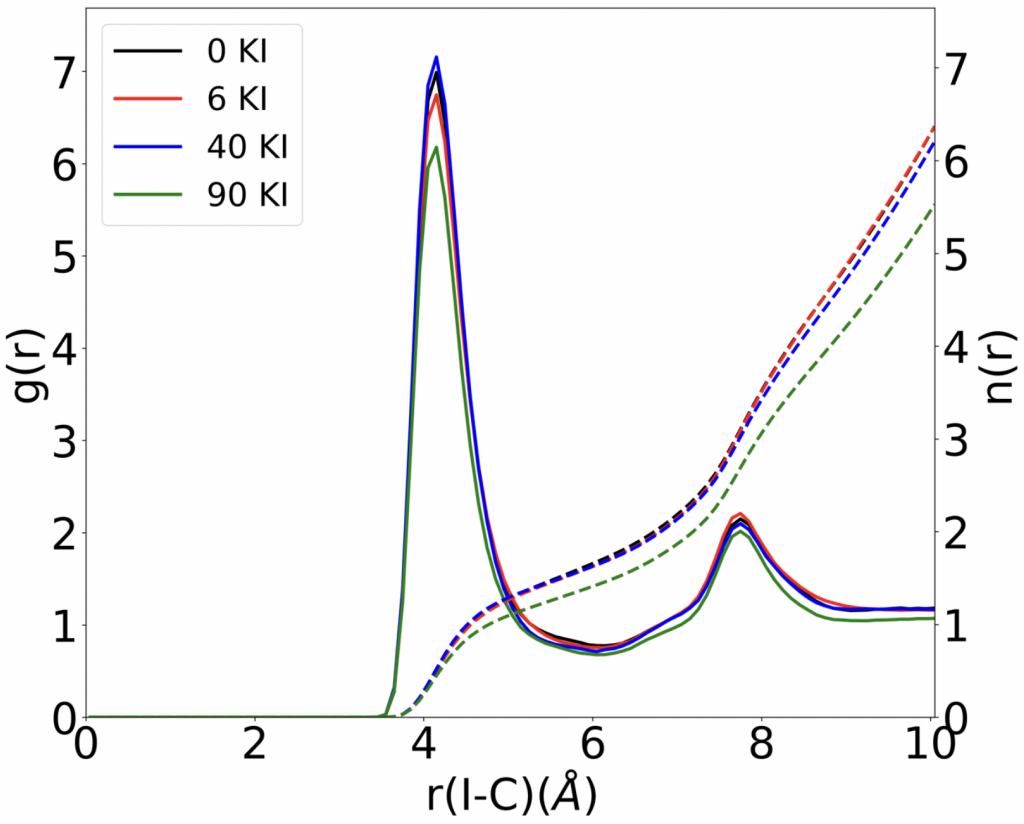

Figure 4.2. The Radial distribution function, g(r), (solid lines) and coordination number, n(r), (dashed lines) for I-C (C from -CH_3 group attached to N) for the BCE in different salt concentrations.

Table 4.2. The ratio (N_{I^-}/N_C) of the total number of iodide ions that are coordinated to a pyridinium to the total number of pyridinium units, coordination number for water around I^- , coordination number for water around K^+ and coordination number for water around pyridinium for five cases: concentrated aqueous solution of BCE without added salt, concentrated aqueous solution of BCE with added salt (from 6 to 90 KI) and dilute BCE solution with no added salt.

	BCE	BCE (6 KI)	BCE (40 KI)	BCE (90 KI)	BCE (dilute)
N_{I^-}/N_C	0.88±0.01	0.89±0.01	0.99±0.01	1.09±0.01	0.40±0.12
Coordination number for water around I^-	4.19	4.18	4.11	4.13	NA
Coordination number for water around K^+	NA	4.96	5.10	4.93	NA
Coordination number for water around pyridinium	4.66	4.60	4.24	3.84	NA

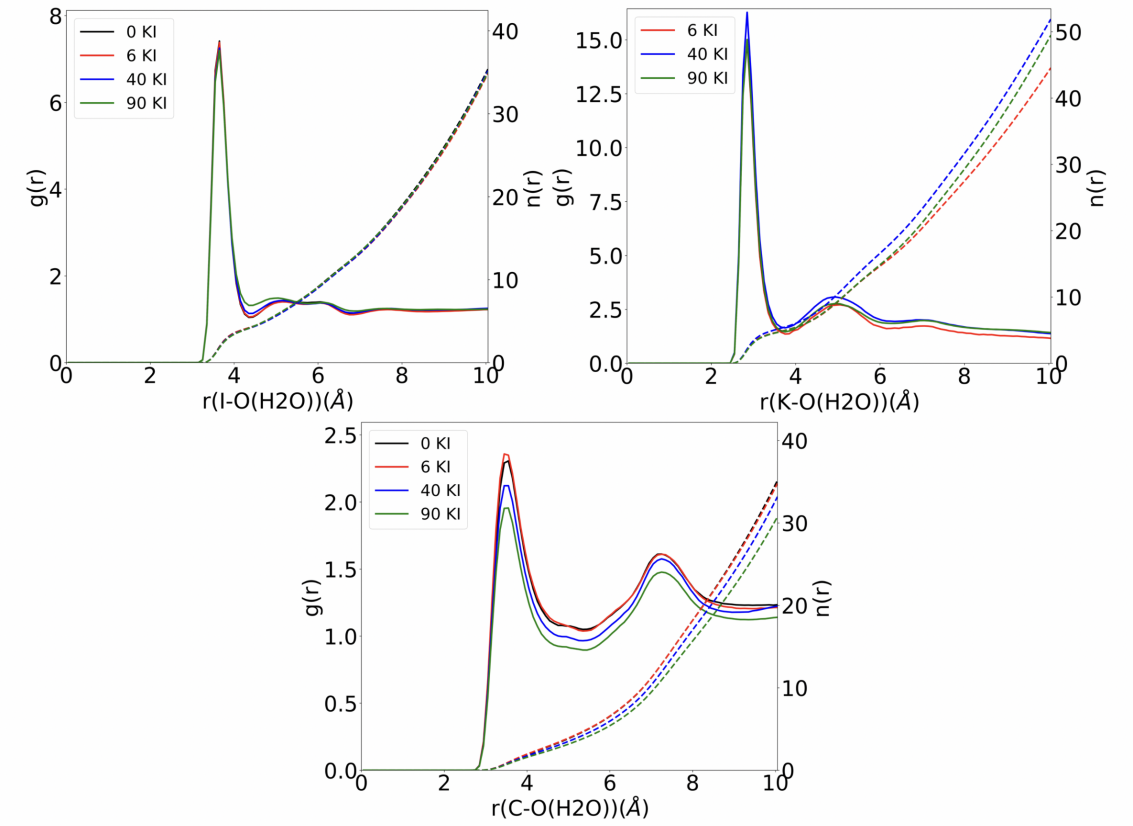

Figure 4.3. The Radial distribution function, g(r), (solid lines) and coordination number, n(r), (dashed lines) for I-O (H_2O), K-O (H_2O) and C (C from -CH_3 group attached to N) -O (H_2O) for the BCE in different salt concentrations.

From the MD simulations, we also noticed that the extent of counterion condensation is significantly governed by the water amount. The fraction of condensed counterion for the dilute case is around 40 % which is substantially lower than that of non-dilute cases. This result revealed that water can help dissociate the ion pairs in polymer electrolytes via solvation and hence lower the fraction of condensed ions.

From Table 4.3, it is clear that the diffusion coefficient of the iodide ion is largely reduced in the low hydration regime of the experimental conditions when compared to the iodide ion in the dilute condition. In addition, the ionic conductivity values derived from the Nernst-Einstein equation which is based on the diffusion coefficient of the ions are an order of magnitude smaller than the experimental conductivities. Hence, the conductivity was also directly calculated from non-equilibrium simulations with an added external electric field in the z-direction. In this case, the conductivity is defined as the magnitude of the current density divided by the magnitude of the electric field. For the concentrated BCE solution case with no added salt, the conductivity obtained from the simulation is 25.9 mS/cm which is of the same order as the experiment. The dramatic increase in the conductivity over what one would obtain from equilibrium self-diffusion data strongly indicates Grotthuss like hopping behavior of the condensed counterion. Hopping is considered to take place if the iodide hops during the timestep delta t to a new solvation shell as compared to the previous solvation shell. Moreover, the iodide ion has to satisfy the condition that it does not go back to the previous solvation shell in the next step. The number of such hops over all the simulation divided by the product of the simulation time and number of iodides gives the hopping rate. Additionally, the hopping rate with the application of an electric field is about 2 times when compared with the regular one (see Table 4.3). These simulation results clearly

Table 4.3. Conductivity for three cases: concentrated aqueous solution of BCE without added salt, concentrated aqueous solution of BCE with added salt (from 6 KI to 90 KI) and dilute BCE solution with no added salt.

	BCE	BCE (6 KI)	BCE (40 KI)	BCE (90 KI)	BCE (dilute)
I^- diffusion coefficient (Å^2/ns)	1.68±0.02	1.92±0.03	2.08±0.03	3.24±0.04	295.12±3.59
K^+ diffusion coefficient (Å^2/ns)	NA	3.16±0.05	4.98±0.03	9.12±0.09	NA
I^- conductivity (mS/cm) from Nernst-Einstein equation	1.12	1.29	1.54	2.71	8.7
K^+ Conductivity (mS/cm) from Nernst-Einstein equation	0	0.04	0.44	1.76	NA
Total Conductivity (mS/cm) from Nernst-Einstein equation	1.12	1.33	1.98	4.47	8.7
I^- conductivity from non-equilibrium simulations (mS/cm)	25.9	29.4	36.5	36.8	22.4
K^+ conductivity from non-equilibrium simulations (mS/cm)	NA	0.4	3.5	9.6	NA
Total conductivity from non-equilibrium simulations (mS/cm)	25.9	29.8	40.0	46.4	22.4
I^- hopping rate in equilibrium simulations	51.3	50.6	46.0	43.8	23.7
I^- hopping rate in non-equilibrium simulations	85.9	88.8	93.2	90.2	21.58

indicate that the non-vehicular hopping behavior plays a significant role in the ion transport along the polymer backbone. Finally, experiments results showed that BCE films with liquid droplets exhibited an ionic conductivity ranging from 58 to 68 mS/cm which increases with

the increase of salt concentration. The ionic conductivity values obtained from MD non-equilibrium simulations showed the same trend as a function of salt concentration (25.9–46.4 mS/cm).

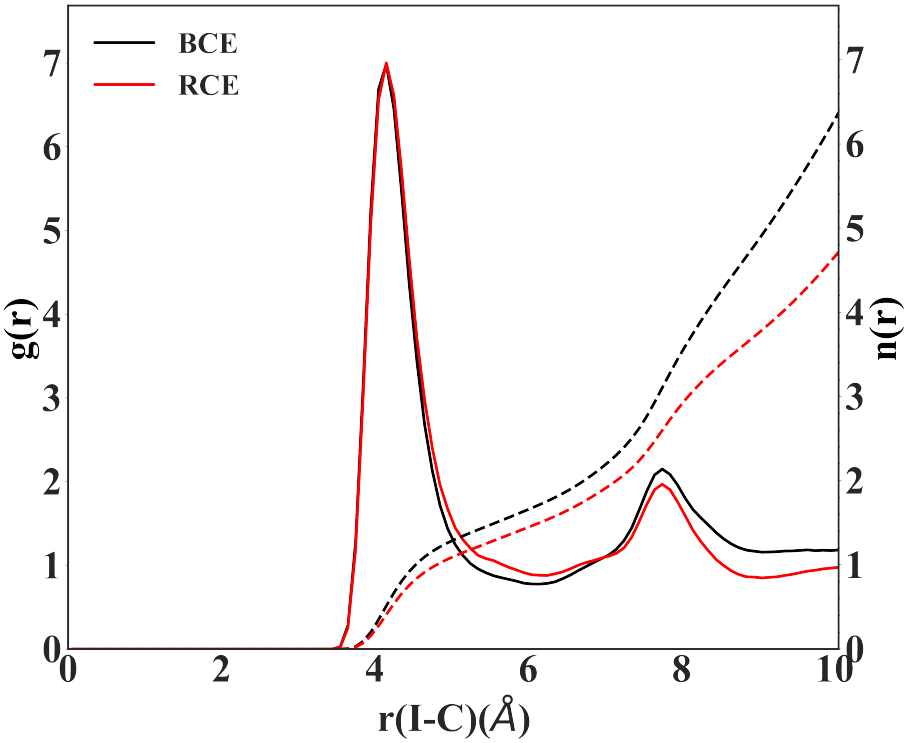

Figure 4.4. The Radial distribution function, g(r), (solid lines) and coordination number, n(r), (dashed lines) for I-C (C from -CH3 group attached to N) for the BCE and RCE.

To get a microscopic point of view of how polymer electrolytes architectures affects their bulk properties, we performed MD simulations for BCE and RCE cases. The fraction of condensed counterions is obtained via RDF and the extent of counterion condensation in BCE is higher than that of RCE (see Table 4.4). I^- ions in BCE are more likely to be attached to the polymer charged group, which is also evidenced by the high coordination number for I^- with C from pyridinium. Additionally, as can be seen in Figure 4.4 , there are more water molecules in I^- and C first solvation shell in BCE.

To further understand how the motion of water molecules affect the ion transport

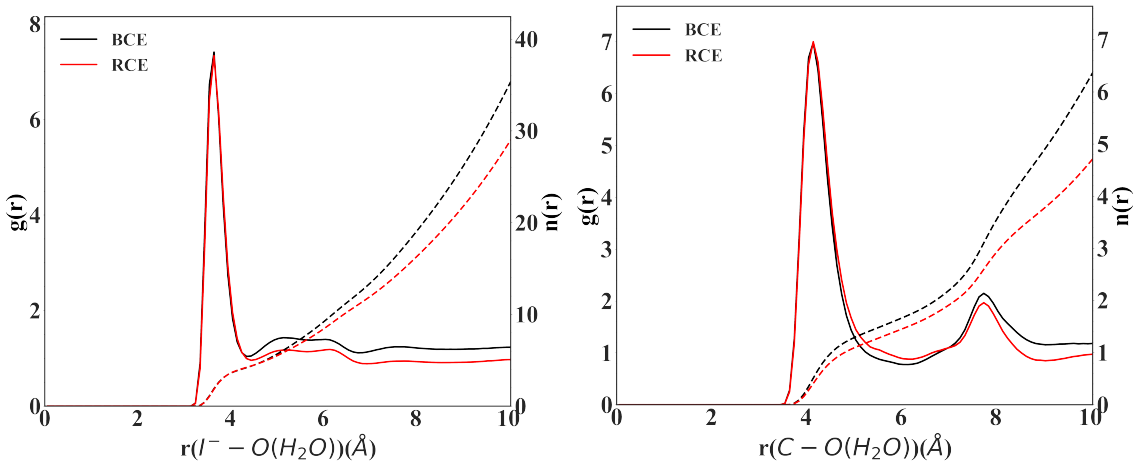

Figure 4.5. The Radial distribution function, g(r), (solid lines) and coordination number, n(r), (dashed lines) for I-O (H2O) and C (C from -CH3 group attached to N) -O (H2O) for the BCE and RCE.

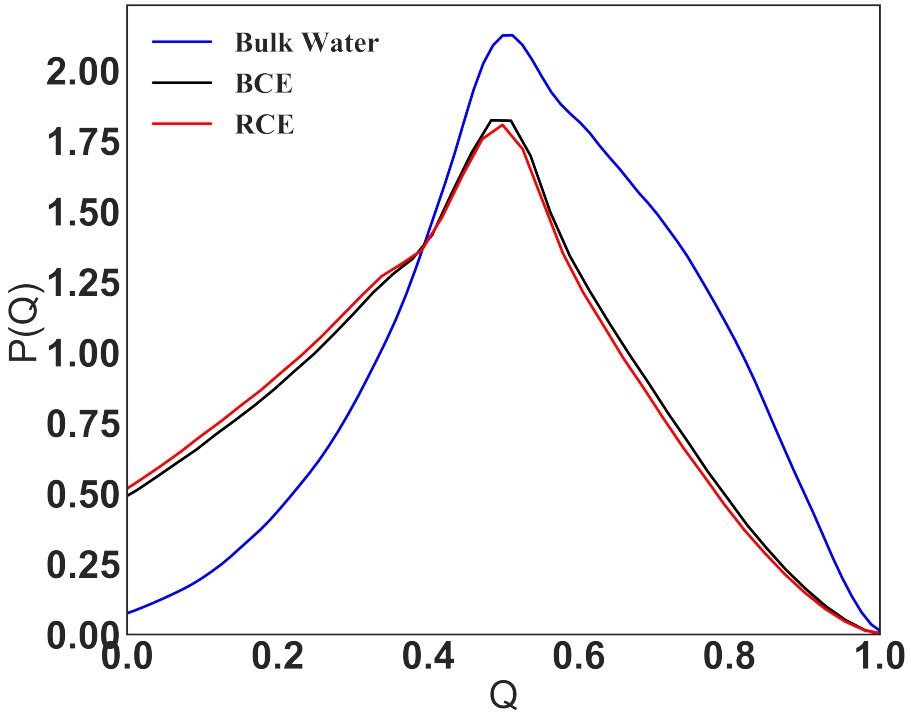

Figure 4.6. Tetrahedral water order parameter for water in BCE, RCE and bulk water.

dynamics, translational and rotational dynamics of water molecular has been measured in both BCE and RCE. As shown in Table 4.4, water rotational dynamics and translational diffusion is faster in the BCE over RCE but slower than bulk water (diffusion coefficient:

Table 4.4. Comparison of solvation and transport observables between BCE and RCE

	BCE	RCE
N_{I^-}/N_C	0.88±0.01	0.85±0.01
Largest water cluster size	1372±135	842±237
Water diffusion coefficient (Å^2/ns)	25.1±0.9	22.9±0.3
Water rotational dynamics(ps)	87	103
Iodide diffusion coefficient (Å^2/ns)	1.6±0.1	1.1±0.1
Iodide Conductivity (mS/cm)	25.9	21.6
Iodide hopping rate (ns^{-1})	51	51
Iodide hopping rate with electric field (ns^{-1})	86	74
Coordination number for water around pyridinium	3.52	3.05
Coordination number for water around I^-	4.36	4.22

519 $\mathring{A}^2$/ns,[232] rotational correlation time: 2.36 ps.[155]) Moreover, examining the distribution of the tetrahedral order parameter of water molecules, we found that the solvation structure of the water molecules themselves in both the BCE and RCE systems deviates significantly from the bulk. There is a clear shift to lower values of q indicating the non-bulk like solvation environment of the water in the channels.

The simulation trajectory of the BCE showed distinct water-rich hydrophilic domains and water-poor hydrophobic regions, while water in RCE is less aggregated and disconnected as is clearly shown from the representative simulation snapshot in Figure 4.7. This percolated water (water percolation here describes the behavior of a water network where water are connected by hydrogen bonds, water percolate through the polymer electrolytes, ions can transport through the water network.) behavior is quantified using the largest water cluster

size and water cluster size distribution. Two water molecules are considered as belonging to the same water cluster if they are connected by hydrogen bonds. The size of a water cluster is characterized by the number of water molecules belonging to it. Two water molecules are considered to be hydrogen-bonded if the distance between the hydrogen atom from one water molecule and the oxygen atom from another water molecule is less than 2.5 Å.

The water cluster size distribution is shown in Figure 4.8. Both BCE and RCE showed a big peak around 100 which indicates that some small water clusters exist. There

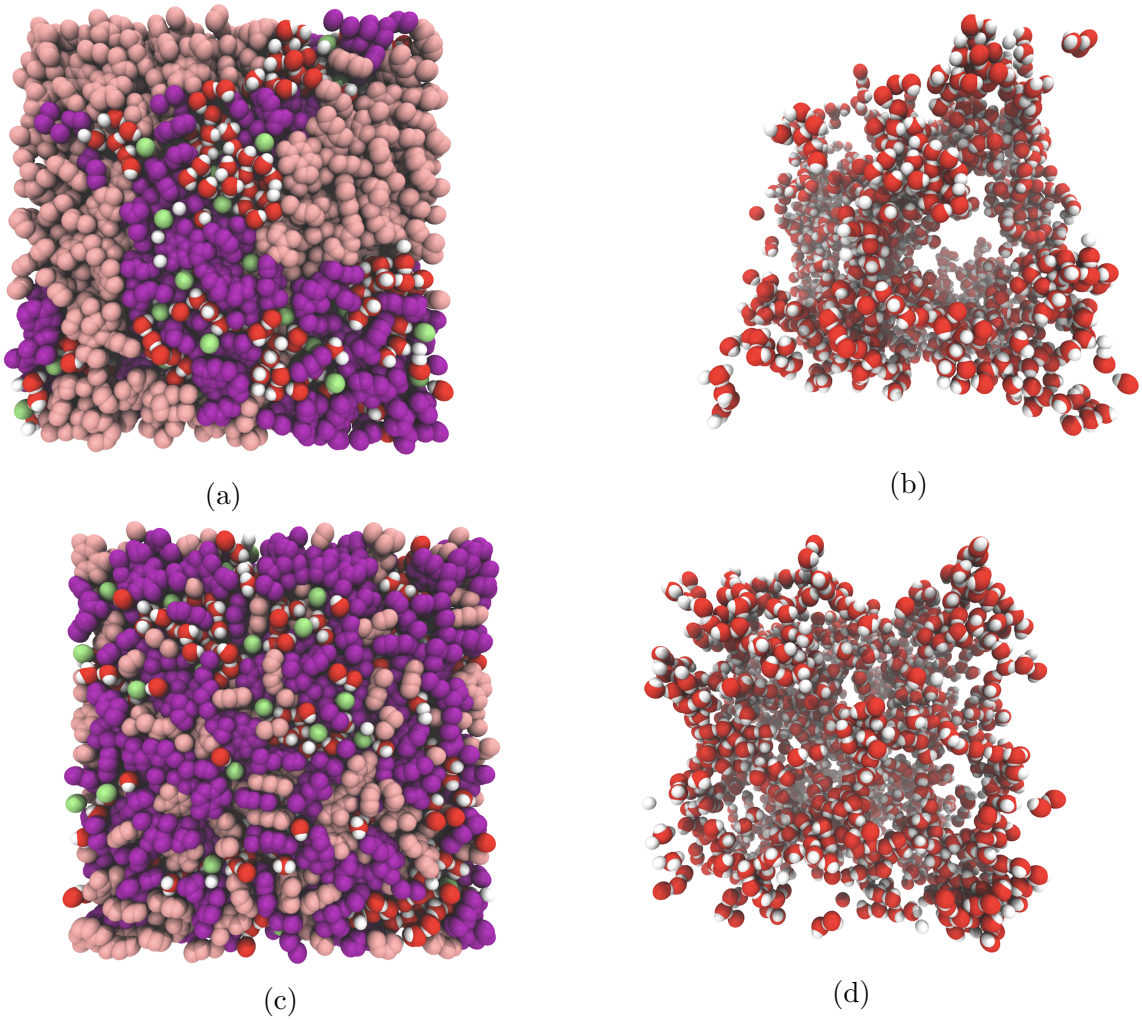

Figure 4.7. Simulation snapshots, purple represents pyridine and pyridinium, pink is styrene, white and red correspond to water, and green is the iodide counterion (a) BCE (b) water inside BCE (c) RCE (d) water inside RCE

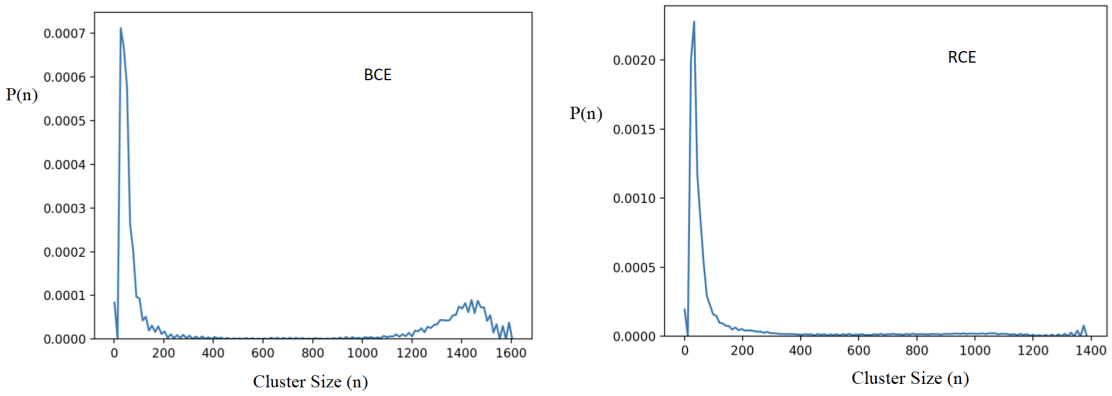

Figure 4.8. Water cluster size distribution in BCE and RCE

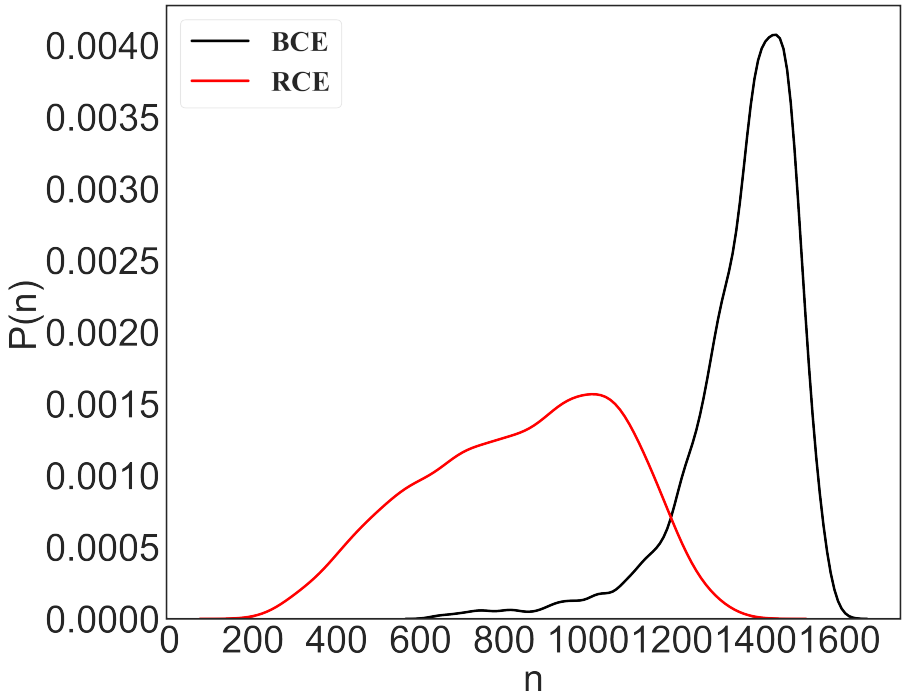

Figure 4.9. Probability, P(n), distribution of the largest water clusters as a function of the number of water molecules (n) in the clusters for BCE and RCE.

is also a broad peak around cluster size 1400 for BCE while there is no obvious peak for RCE in that part. The largest water cluster size and distribution for BCE and RCE were also measured to quantitatively show the difference (see Table 4.4 and Figure 4.9). Not surprisingly, the largest water cluster in BCE is much bigger when compared to RCE. For

largest water cluster distribution, BCE showed a narrow distribution while RCE showed a wide one. In addition, although the iodide diffusion constant and iodide hopping rate in BCE are similar to that of iodide in RCE, the iodide hopping with the electric field shows a significant difference between BCE and RCE. All the data suggests that the ion migration due to ion hopping along the chain that is possibly mediated by more percolated water in the BCE case. The faster ion hopping contributes to a higher conductivity for BCE when compared to RCE. BCE with percolated pathways of ionic charge domains provides water channels and ions have faster transport dynamics when applied with an extra electric field in the water network.

4.4. Conclusion

The implications of multiple simulations for BCE highlighted that water plays an important role in ion dissociation and ion activity. The presence of additional water lowers the fraction of condensed ions. In addition, the ionic conductivity calculated from non-equilibrium simulation revealed that the importance of iodide ion hopping along the backbone which contributes to the high conductivity of BCEs. In the case of RCE, although RCE displays lower counterion condensation, the lower ionic conductivity, when compared to BCE, was attributed to small water aggregates with lower percolation . The faster transitional and rotational dynamic of water molecules inside BCE result from the connected water network and can partially account for the higher ionic conductivity.

Chapter 5. Ionic Conductivity of Nanoconfined Polycation and Polyanion Brushes – A Computational Study

5.1. Introduction

High ion-conducting polymer electrolytes have been extensively investigated by researchers due to their potential application in electrochemical devices such as sensors, batteries, fuel cells, ionic separations, and electrolyzers, and water purification units.[217,219,233–236] These polymer electrolytes can not only be used to transit ions but can also serve as a mechanical separator between the two electrodes. An important priority for electrochemical systems is to maximize the ionic conductivity of polymer electrolytes because it can lower the ohmic overpotential in devices, which can lead to higher thermodynamic efficiency. Increasing the ionic loading of the polymer electrolyte is a common way to improve conductivity, but the problem with this strategy is that a continued increase in ionic loading will lead to poor mechanical properties and excessive swelling.[237,238] The desired properties of polymer electrolytes are to have high ionic conductivity while maintaining the mechanical resilience at the same time. However, these two properties often have a negative correlation.[89,90,222] Microphase separated block copolymer electrolytes (BCEs)[55–59] provide a promising solution to this, because the ionic groups contribute to high ionic conductivity and the non-ionic group endows the material with better mechanical properties.[239] Block copolymers have been manipulated into different microstructures such as lamellae, spheres, cylinders, etc.[59,240] Arges et al. points out that the current studies for the relation between BCE microstructure and ionic conductivity have some drawbacks.[66,90] Furthermore, they were inspired by the

Content in this chapter is published as one article in Molecular Systems Design & Engineering, [C. G. Arges, K. Li, L. Zhang, Y. Kambe, G. Wu, B. Lwoya, J. N. L. Albert, P. F. Nealey and R. Kumar, Mol. Syst. Des. Eng., 2019, 4, 365] reproduced by permission of The Royal Society of Chemistry.

literature review to make ordered BCE structures that can bridge the gap between the microstructure and ionic conductivity.[66]

Experimentally, to mimic lamellae structures found in bulk BCE membrane materials, nano-confined sulfonated poly(styrene) with H as the counterion and nano-confined poly(2-vinyl-1-methylpyridinium iodide) polymer electrolyte brushes were prepared. These brushes were prepared using block copolymer template-assisted lithography.[241,242]The nano-confined polymer electrolyte brushes showed excellent ionic conductivities (10^{-2} S$\cdot cm^{-1}$ to 10^{-1} S$\cdot cm^{-1}$) for both the anion and the cation case. To further understand why nano-confined polymer electrolyte brushes have better ionic conductivities than non-confined polymer electrolyte brushes, a computational study is needed. It can provide the molecular-level understanding of the reasons behind the conductivity difference between nano-confined polymer electrolyte brushes and non-confined polymer electrolyte brushes which are not accessible through experiments. Atomistic molecular dynamic simulation is a computer simulation method for studying the physical movements of atoms and molecules which can model rather large systems with nano-timescale. The transport mechanism of ions, solvation structure and the couterion condensation can be obtained through these simulations.

5.2. Computational Methods

5.2.1. Classical Molecular Dynamics Simulations

We performed a series of MD simulations for idealized systems using a conventional non-reactive force-field based on the OPLS-AA[111] for the polymer brushes along with the TIP3P[230] model for water. The non-bonded parameters for silicon substrate is based on the work of Cruz-Chu et al,[243] and the parameters used to simulate the hydronium were taken

from a refined MS-EVB model developed by Wu and coworkers.[244] The partial charges on the polymers were determined by fitting to the ab-initio electrostatic potential on a grid around the polymer electrolyte unit molecule (a single repeating unit of the polymer), using the CHELPG[205] scheme at the the HF/6-31G* level with the Gaussian 09 software,[206] and the partial charge is shown in Table B.1 (Appendix B). The reason for choosing this scheme is to maintain consistency with the OPLS-AA force field. For the polycation case, the iodide and pyridinium charges were scaled by 0.8 to take into account polarization effects based on the work by Vazder et al. and Leontyev et al.[245,246] The initial structures of the polystyrene, poly(styrene sulfonate), and the poly(2-vinyl-1-methylpyridinium) brushes were generated consisting of the monomeric units arranged in a trans isomerism using the Avogadro software.[207] Each brush consisted of ten monomeric units. The silicon substrate structure, as shown in Figure 5.1, was generated based on a cubic diamond lattice, in which the lattice constant is 0.5431 nm.[247] The thickness of the silicon substrate is 0.5431 nm as well. For each simulation box, there are 8 polymer brushes, which are attached to the SiO_x

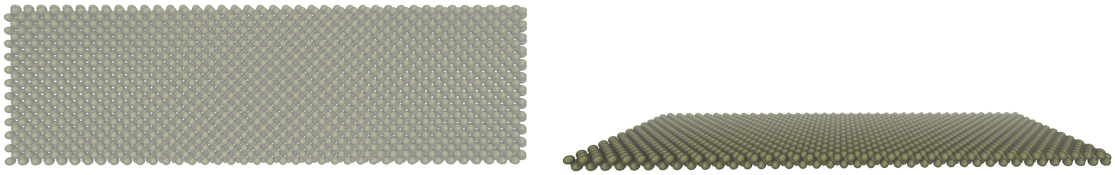

(a) (b)

Figure 5.1. (a): Model silicon substrate front (b): Model silicon substrate side

substrate through an oxygen atom. In the case of the nano-confined polyanion/polycation brushes, to mimic experimental condition, 4 charged (all of the monomeric units were ionized) poly(styrene sulfonate)/poly(2-vinyl-1-methylpyridinium) were placed along the one axis of

the silicon substrate with the distance between each charged polymer brushes equal to 17 Å. The counterions for the poly(styrene sulfonate) are hydronium ions and iodide anions are the counterion for poly(2-vinyl-1-methylpyridinium). Moreover, 4 uncharged polystyrenes, which function as a nano-confinement, were placed parallel to the charged polymers with the same interval as the charged case. The distance between the charged polymer brushes and the uncharged one is 140 Å which is the maximum possible distance between a non-charged polymer domain and a charged polymer electrolyte in the experimental system. The structure of nano-confined case is shown in Figure 5.2.

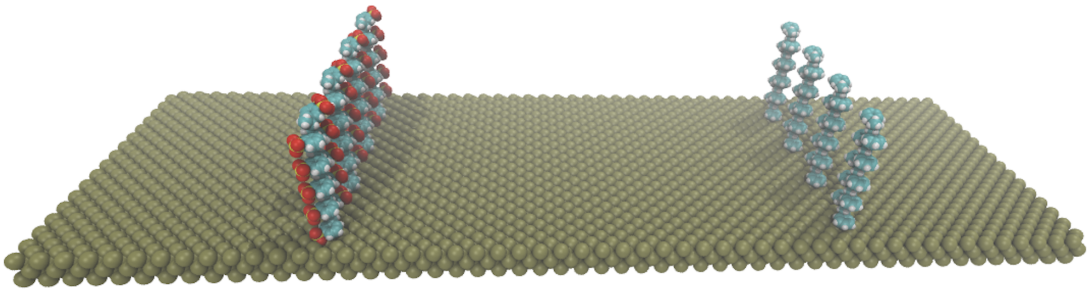

(a) Nano-confined polymer brushes, 4 uncharged polystyrenes on the right side, and 4 charged poly(styrene sulfonates) on the left side

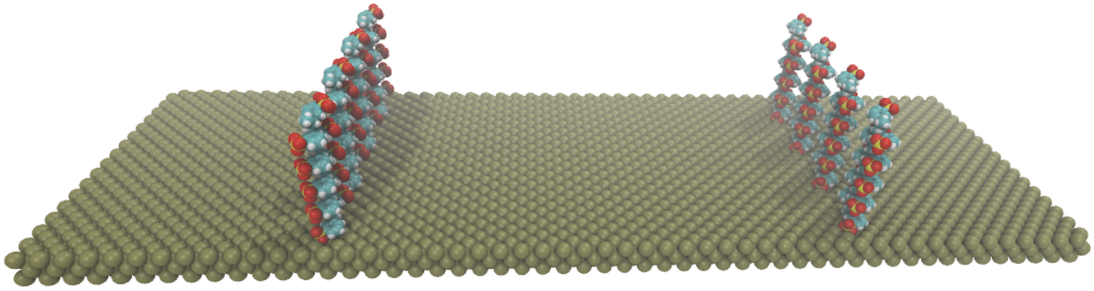

(b) Non-confined polymer brushes, 8 charged poly(styrene sulfonates)

Figure 5.2. Nano-confined polymer brushes and Non-confined polymer brushes in their initial structures for MD simulation.

To represent the non-confined case, two systems of only charged polymer brushes with either 8 poly(styrene sulfonates) or 8 poly(2-vinyl-1-methylpyridinium) were built and the

brushes were put in the same position as the nano-confined ones (with 4 of them replacing the polystyrene nano-confinement). Four cuboid simulation boxes were constructed, and all the simulation boxes have the dimensions of (284 $\mathring{A}$ × 94 $\mathring{A}$ × 100 $\mathring{A}$). For all the four simulations, two were for the nano-confined polyanion/polycation brushes and the other two for the non-confined cases. The side of the silicon substrate with the polymer brushes was solvated with 25000 water molecules using a random packing algorithm in the Packmol package[130] for all 4 simulation boxes with a boxlength of 45 Å in the z-direction which is perpendicular to the substrate. After random packing, the boxlength in the z-direction was extended to 100 Å and the box was then equilibrated in the canonical ensemble (NVT) for 5 ns at a temperature of 300 K, followed by 20 ns production runs in the NVT ensemble at the same temperature. A second set of simulations was carried out by taking the initial box and running it at 350 K for 5 ns and then gradually cooling down at a constant rate of 10 K/ns to 300 K over another 5 ns and then running an NVT simulation for 20 ns. In all these simulations, the silicon substrate position was kept fixed. The Nose-Hoover thermostat[143–145] was employed to keep the temperature constant, and the integration time step was 1 fs. The SHAKE algorithm[229] was used to constrain the bond lengths and bond angles in the water molecules. All the simulations were performed using the LAMMPS software package[208] under periodic boundary conditions. Particle-particle particle-mesh scheme[148] were used to compute long-range electrostatics interactions.

5.3. Atomistic Molecular Dynamics Simulation Results

In this work, we use various radial distribution functions (RDF) to get the local structure surrounding the ionic group in the four-different cases. Based on the solvation

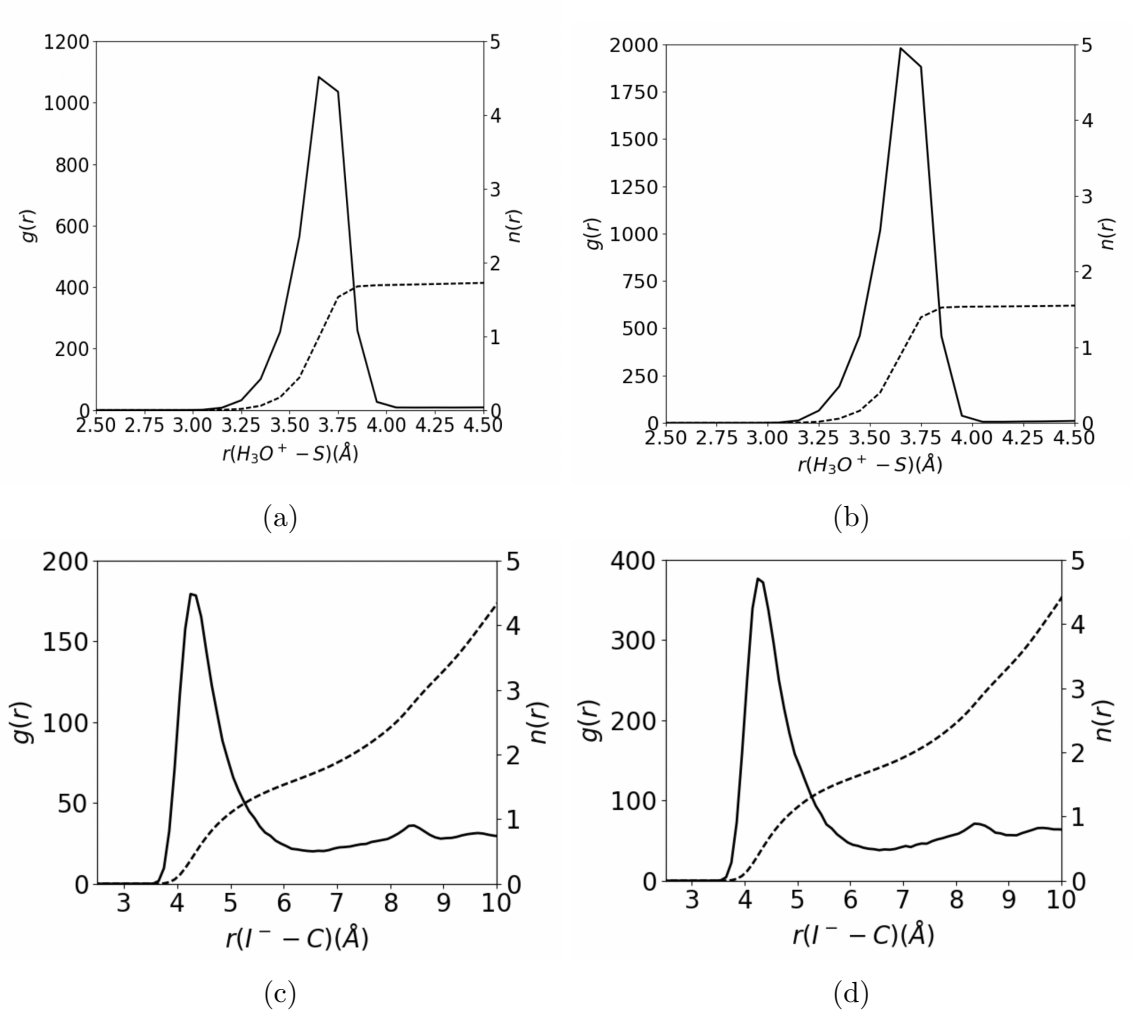

Figure 5.3. Radial Distribution Functions, (a) O-S (oxygens from hydronium) for non-confined polyanion, (b) O-S (oxygens from hydronium) for nano-confined polyanion, (c) I-C (carbon form $-CH_3$ group) non-confined polycation, (d) I-C (carbon form $-CH_3$ group attached to N) for nano-confined polycation.

structures, the fraction of condensed ion as well as free ion can be obtained. The faction of condensed hydronium ions is calculated using a definition based on the O (from H_3O^+) and S (from the sulfonate groups) radial distribution functions. The minimum of this radial distribution function, which can be seen in Figure 5.3, at 4.35 Å is taken as the cutoff to define hydronium ions coordinated to the sulfonate groups. Similarly, for the polycation, the first minimum of I^- (the iodide) and C (the carbon belonging the methyl group attached

to the N atom) radial distribution function at 6.35 Å is taken as the cutoff to define iodide ions coordinated to the cationic group of the polymer.

Table 5.1. Fraction of counterions condensed along with the overall diffusion constant of the counterions and the diffusion constant of the non-condensed counterions for the nano-confined and non-confined polycation and polyanion

poly(styrene sulfonate) / H_3O^+ nano-confined case		poly(styrene sulfonate) / H_3O^+ non-confined case	
$H_3O^+ - S$	Fraction	$H_3O^+ - S$	Fraction
Fraction of counterions condensed	0.77	Fraction of counterions condensed	0.84
Diffusion Coefficient($\AA^2/ns$)	109	Diffusion Coefficient($\AA^2/ns$)	73
Non-condensed H_3O^+ Diffusion Coefficient($\AA^2/ns$)	520	Non-condensed H_3O^+ Diffusion Coefficient($\AA^2/ns$)	522
poly(2-vinyl-1-methylpyridinium) / I^- nano-confined case		poly(2-vinyl-1-methylpyridinium) / I^- non-confined case	
$I^- - C$	Fraction	$I^- - C$	Fraction
Fraction of counterions condensed	0.70	Fraction of counterions condensed	0.75
Diffusion Coefficient($\AA^2/ns$)	216	Diffusion Coefficient($\AA^2/ns$)	182
Non-condensed I^- Diffusion Coefficient($\AA^2/ns$)	519	Non-condensed I^- Diffusion Coefficient($\AA^2/ns$)	525

As can be seen from Table 5.1, the nano-confined polymer electrolyte brushes have less condensed counterions when compared to non-confined polymer electrolyte brushes. Moreover, counterions in nano-confined polymer electrolyte brushes have higher average vehicular diffusion coefficients than those in non-confined polymer electrolyte brushes. Therefore, a large fraction of non-condensed counterions results in higher average vehicular diffusion coefficients. Table 5.1 also shows that H_3O^+ had almost the same diffusion coefficient as I^-, however, in reality, the ionic mobility for H_3O^+ counterions is about 5 times higher than

for I^- counterions. The reason is that the force-field used in this study is a non-reactive force-field which means it does not consider the Grotthuss shuttling mechanism or proton transfer events, and this proton shuttling mechanism can increase the H_3O^+ ionic mobility by 4 times.[248] Interestingly, the non-condensed counterions average diffusion constant are the same for all the systems in the MD simulation, however, the average diffusion coefficient values for counterions in the nano-confined polymer brushes were larger than the non-confined cases. The reason is that nano-confined systems have a smaller fraction of condensed counterions compared to non-confined polymer electrolyte systems and the non-condensed counterions have significantly larger diffusion constant.

5.4. Conclusion

Experimentally, nano-confined polymer electrolyte brushes exhibit excellent ionic conductivity when compared to non-confined case. Using atomistic molecular dynamic simulations, this study provides a molecular level of understanding of this phenomenon. It revealed that counterions in nano-confined samples are more likely to be solvated by the gathering water resulting in a large fraction of non-condensed conterions. In addition, the non-condensed counterions have a larger average diffusion constant versus condensed counterions, hence, counterions in nano-confined samples diffuse faster on average when compared to non-confined cases. Finally, the results motivate future studies to investigate counterion condensation effects on ionic transport and water solvation impact in polymer electrolytes system using experimental tools combined with molecular simulations.

Chapter 6. Outlook and Future Directions

6.1. Future Work

In Chapter 3, we investigated the transferability of a new model, which was developed by Wahlers et al.,[2] applying to glyme of varying lengths and different salt concentrations. This new model optimized the intermolecular interactions between sodium triflate (OTf) and diglyme molecules. The trifluoromethanesulfonimide (TFSI) anion is also a popular anion to be used in the electrolytes system and it presents a similar chemical structure compared to triflate (see Figure 6.1). The next set of studies will concentrate on sodium TFSI in the diglyme system.

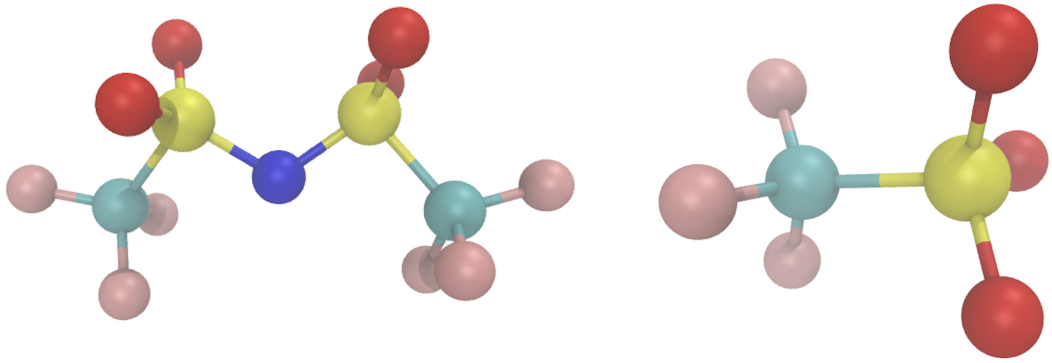

(a) $(CF_3SO_2)_2N^-$ (b) $(CF_3SO_3)^-$

Figure 6.1. Model TFSI anion (a) and model triflate anion (b)

The only parameter we miss here is the pair coefficient (Lennard-Jones interaction) for N atom in TFSI anion. The non-bonded interactions parameter for the nitrogen will be taken from the PCFF[137] force-field. Ab-initio MD simulation will also be performed to compare the results get from the classical MD simulations and, if the need arises, further optimized them. Radial Distribution Functions will be used to validate the accuracy of the non-bonded interactions. In addition, we will compare the solvation structures and dynamics

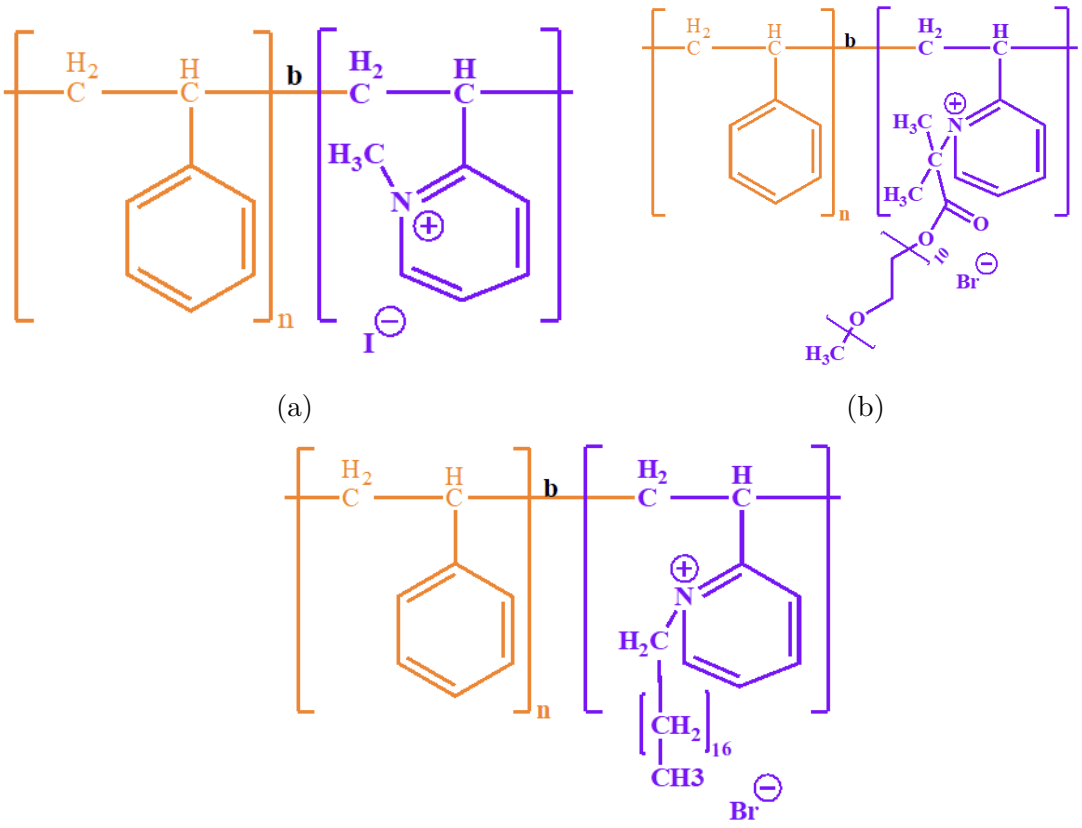

Figure 6.2. (a) BCE (b) BCE with ether side chain (c) BCE with carbon side chain.

of sodium TFSI in diglyme and sodium triflate in diglyme with different salt concentrations to provide a complete picture of the dynamic of these systems and provide direction for enhancing these electrolytes. In Chapter 4 and Chapter 5, block copolymer electrolytes (BCEs) have been studied. The water inside BCEs plays a significant role. Water not only can promote ion dissociation but also can form percolated pathways for ions to transport and hence increase the conductivity. The next step of studies is inspired by Miller and co-workers[249] who showed that the ether groups promote anion dissociation. Based on the BCE we used in Chapter 4, we will add ether groups to the BCE (see Figure 6.2). The free pair of electrons in the oxygen in the ether groups can coordinate with the cation (e.g. K^+) and

slow down the movement of the cation. Additionally, we will add an alkyl chain of similar length as the ether chain to the BCE to represent the non-coordinating case for comparison. The question that arises here is whether the ether groups will effectively promote anion dissociation in this circumstance. The solvation structures of ions, the dynamics of ion transport, the water dynamics, and connectivity will be examined. Both the ether-based and alkyl-based BCEs will be studied to understand the properties of these systems and therefore enhance the engineering of tailored BCEs.

Appendix A. Supplementary Material for Chapter 3

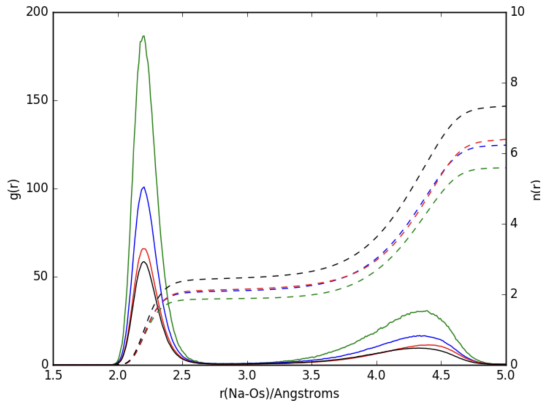

(a) Na-Os (sulfonate oxygen)

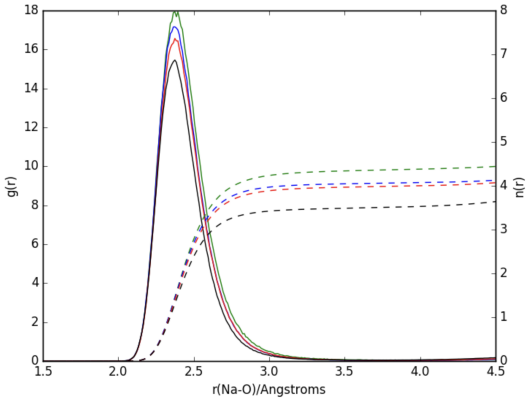

(b) Na-O (all oxygens from glyme)

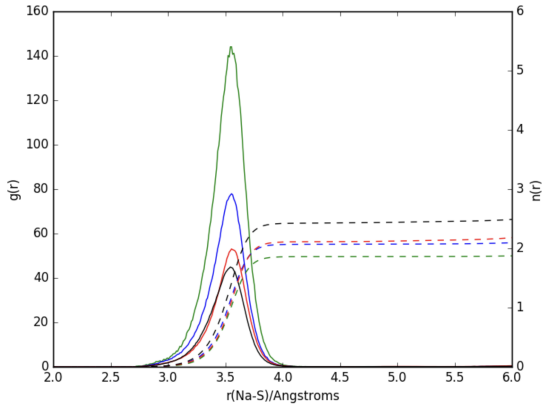

(c) Na-S (sulfur from triflate)

Figure A.1. Radial distribution functions (solid) of monoglyme from classical MD simulations at 0.5 M (green), 1.0 M (blue), 1.5M (red), and 2.0 (black). Dashed lines show the coordination number for the corresponding concentration.

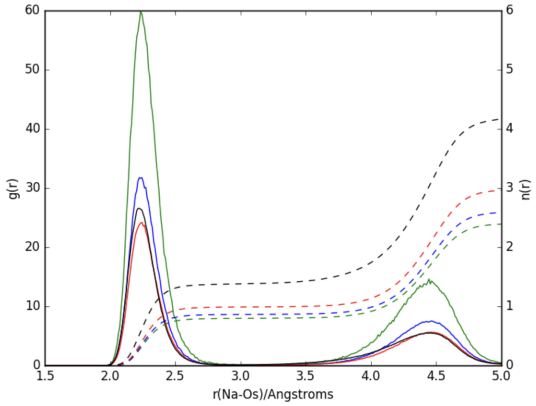

(a) Na-Os (sulfonate oxygen)

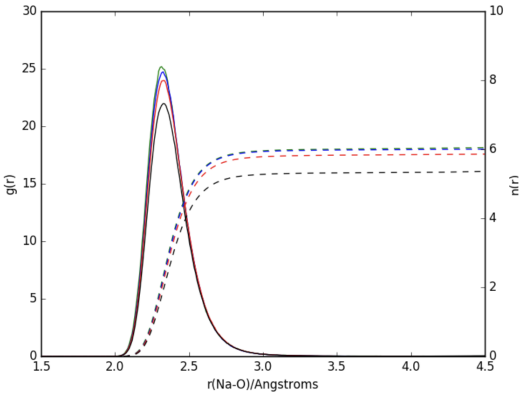

(b) Na-O (all oxygens from glyme)

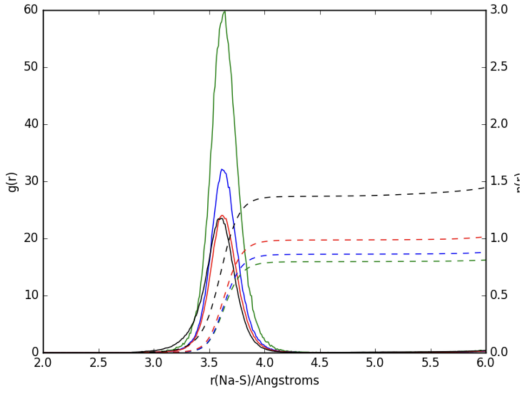

(c) Na-S (sulfur from triflate)

Figure A.2. Radial distribution functions (solid) of diglyme from classical MD simulations at 0.5 M (green), 1.0 M (blue), 1.5M (red), and 2.0 (black). Dashed lines show the coordination number for the corresponding concentration.

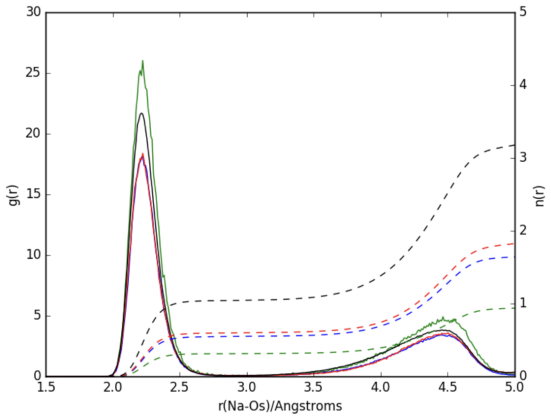

(a) Na-Os (sulfonate oxygen)

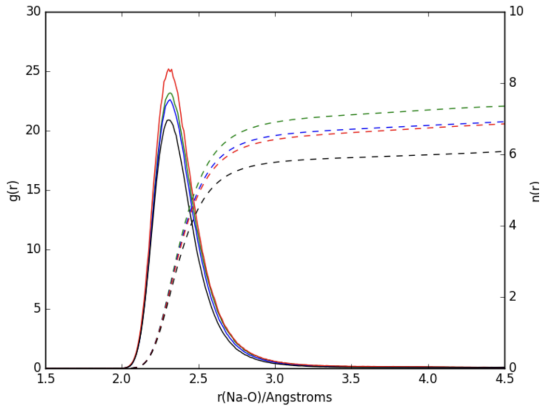

(b) Na-O (all oxygens from glyme)

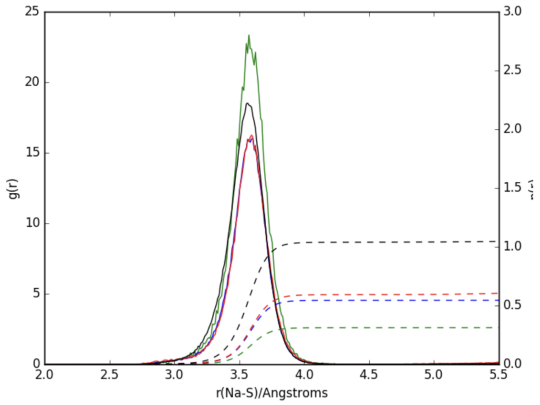

(c) Na-S (sulfur from triflate)

Figure A.3. Radial distribution functions (solid) of triglyme from classical MD simulations at 0.5 M (green), 1.0 M (blue), 1.5M (red), and 2.0 (black). Dashed lines show the coordination number for the corresponding concentration.

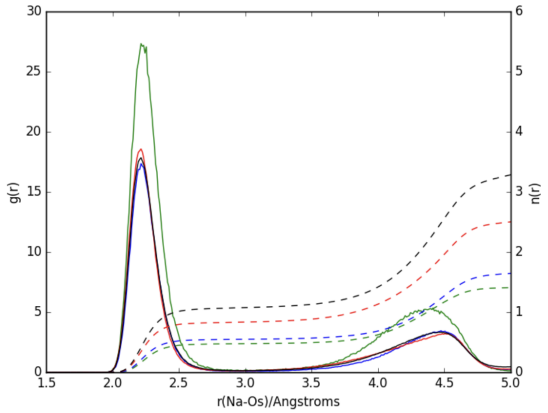

(a) Na-Os (sulfonate oxygen)

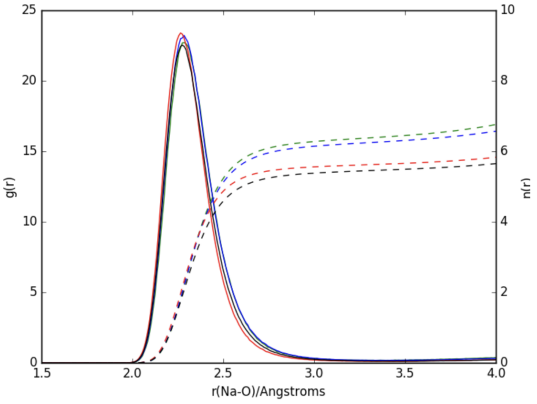

(b) Na-O (all oxygens from glyme)

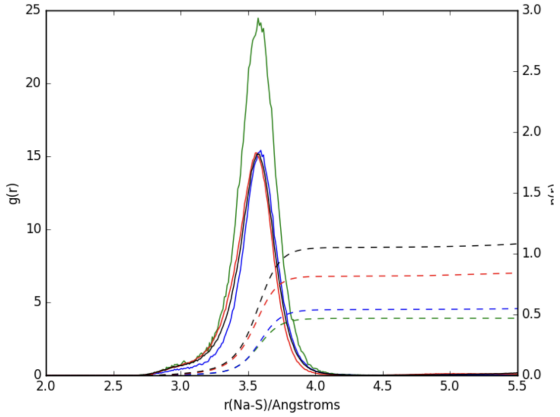

(c) Na-S (sulfur from triflate)

Figure A.4. Radial distribution functions (solid) of tetraglyme from classical MD simulations at 0.5 M (green), 1.0 M (blue), 1.5M (red), and 2.0 (black). Dashed lines show the coordination number for the corresponding concentration.

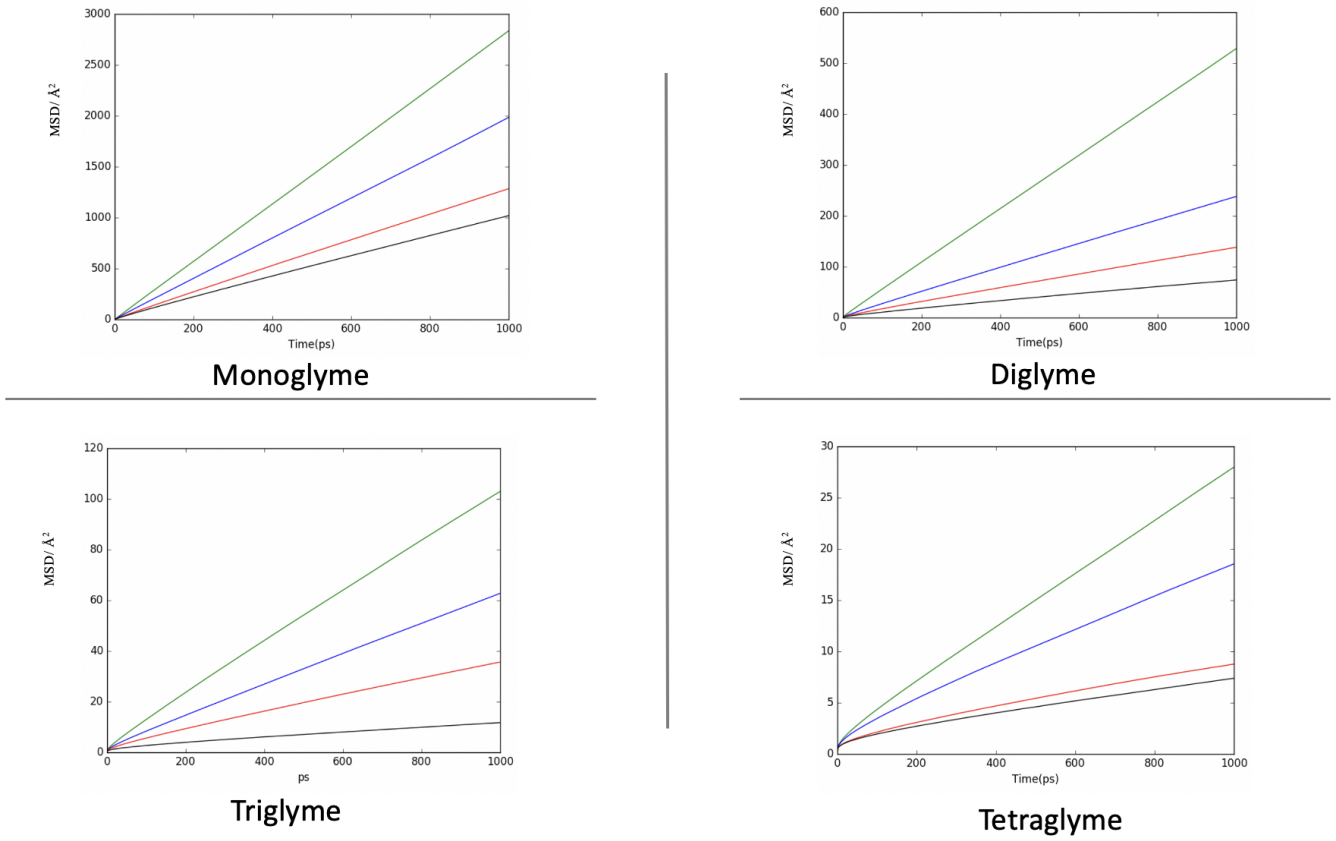

Figure A.5. Mean squared deviation (MSD) versus time (ps) as a function of salt concentration from 0.5 M (green), to 1.0 M (blue), 1.5 M (red), and 2.0 M (black) for the different glymes.

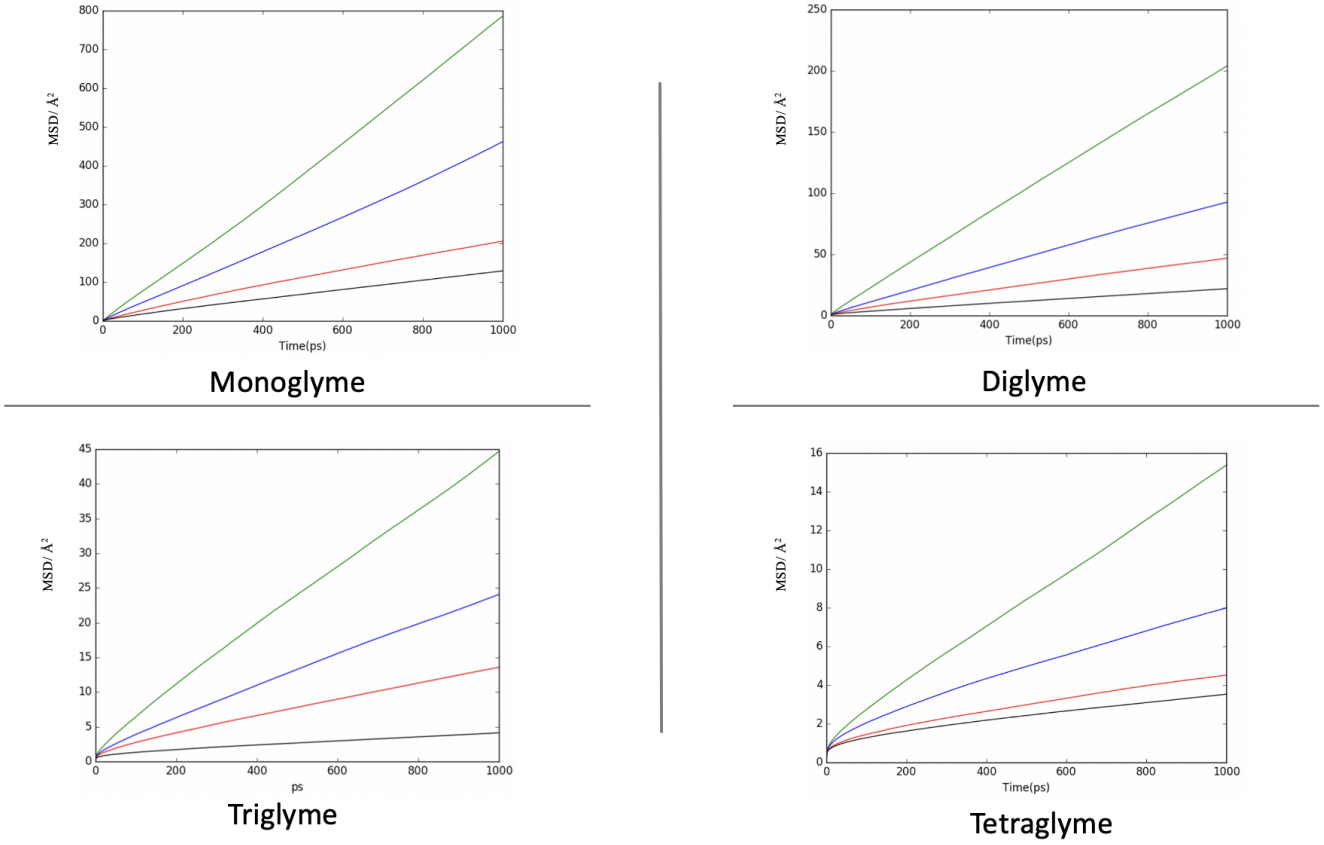

Figure A.6. Mean squared deviation (MSD) versus time (ps) as a function of salt concentration from 0.5 M (green), to 1.0 M (blue), 1.5 M (red), and 2.0 M (black) for the different Na.

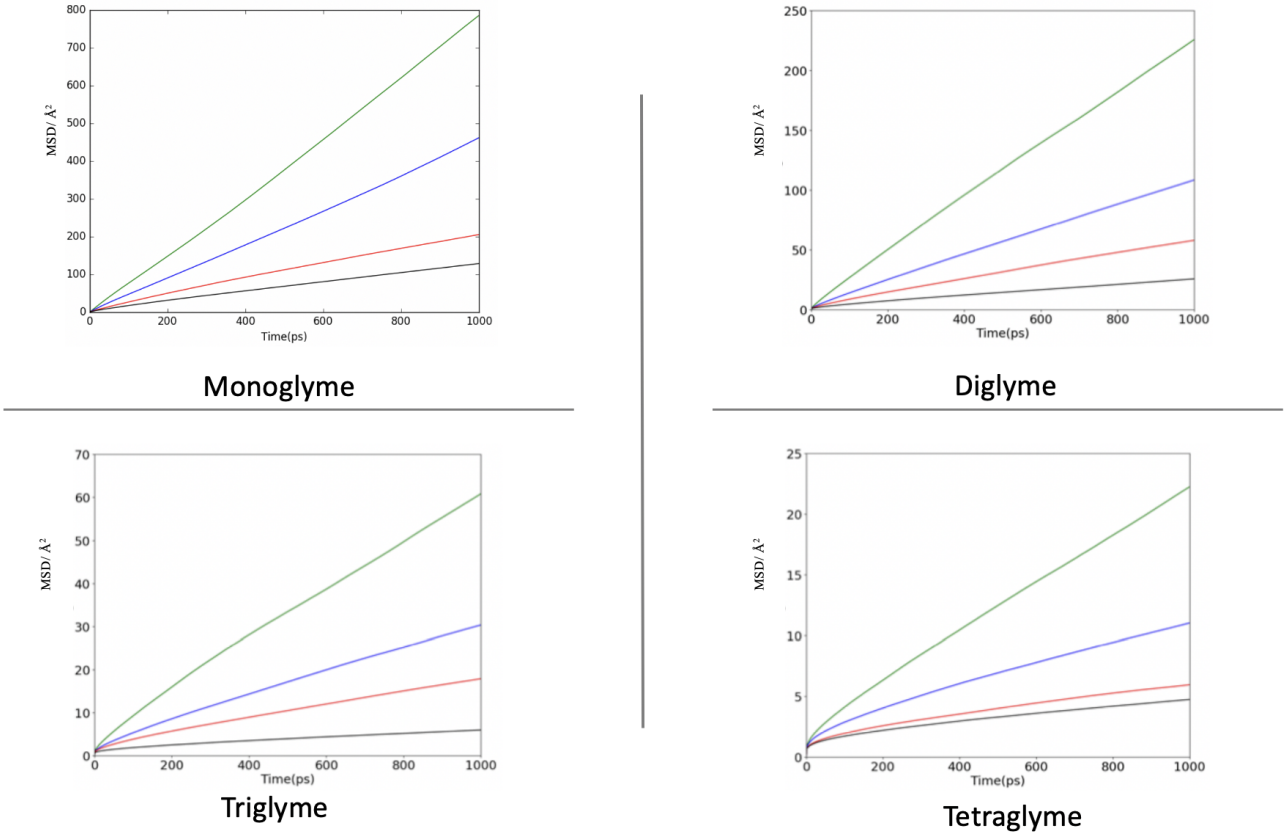

Figure A.7. Mean squared deviation (MSD) versus time (ps) as a function of salt concentration from 0.5 M (green), to 1.0 M (blue), 1.5 M (red), and 2.0 M (black) for the different triflate.

Appendix B. Supplementary Material for Chapter 5

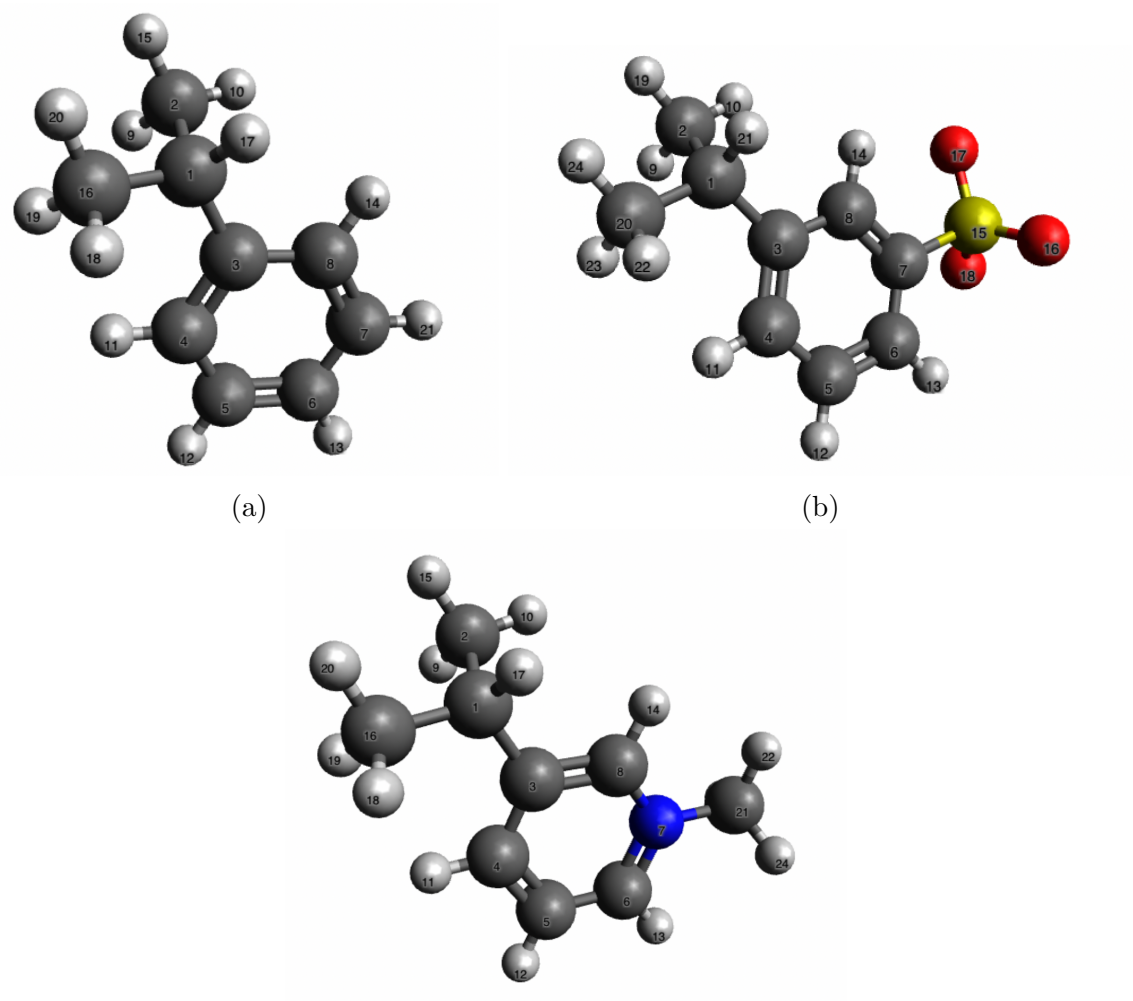

(a) (b)

(c)

Figure B.1. A single unit of the polymer brushes. (a): uncharged polystyrene (b): charged polystyrene sulfonate (c): charged polypyridinium iodide

Table B.1. Partial charge for charged polystyrene sulfonate, uncharged polystyrene and Charged polypyridinium (atom types from Figure 5.3)

Atom Index	Charged polystyrene sulfonate	Atom Index	Uncharged polystyrene	Atom Index	Charged polypyridinium
1	-0.073043	1	0.169626	1	0.186564
2	-0.140419	2	-0.156608	2	-0.208704
3	0.538206	3	0.153179	3	0.030350
4	-0.511280	4	-0.239629	4	0.025434
5	-0.295644	5	-0.053180	5	-0.188413
6	0.340807	6	-0.160523	6	0.049885
7	-0.225069	7	-0.049788	7	0.104182
8	-0.326223	8	-0.233158	8	-0.045072
9	0.028804	9	0.033315	9	0.055629
10	0.014826	10	0.009578	10	0.034752
11	0.178155	11	0.135922	11	0.159281
12	0.102863	12	0.096870	12	0.177779
13	0.051834	13	0.111887	13	0.167775
14	0.122910	14	0.112614	14	0.162849
15	1.298896	15	0.043289	15	-0.248225
16	-0.728059	16	-0.157287	16	0.146144
17	-0.718181	17	-0.001632	17	0.160755
18	-0.735885	18	0.009971	18	0.145264
19	0.052334	19	0.033185	19	0.092294
20	-0.137664	20	0.043506	20	-0.208082
21	0.066262	21	0.098862	21	0.017351
22	0.019232			22	0.034802
23	0.027069			23	0.055424
24	0.049270			24	0.091980

Appendix C. Publication Agreements and Permissions

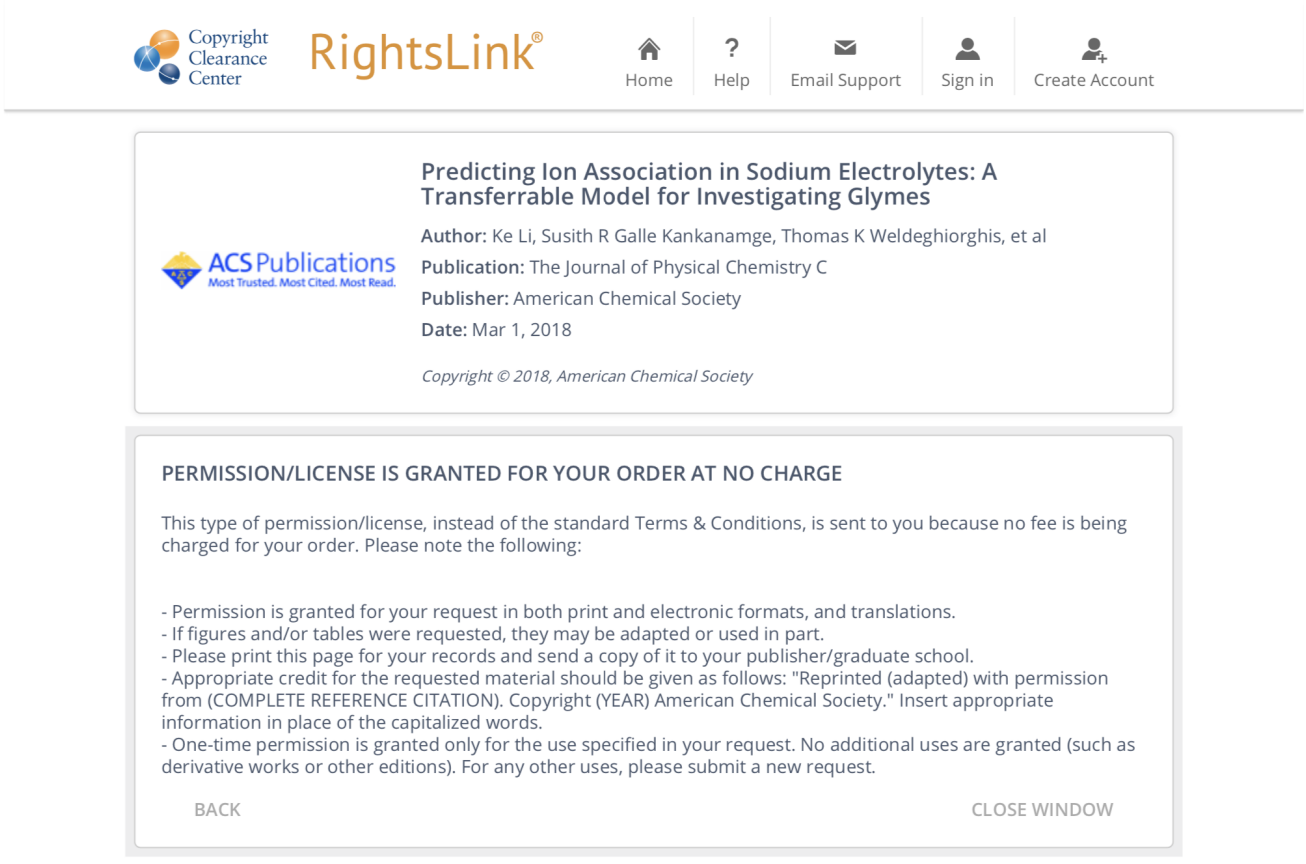

Copyright Clearance Center RightsLink®

Home | Help | Email Support | Sign in | Create Account

ACS Publications
Most Trusted. Most Cited. Most Read.

Predicting Ion Association in Sodium Electrolytes: A Transferrable Model for Investigating Glymes

Author: Ke Li, Susith R Galle Kankanamge, Thomas K Weldeghiorghis, et al

Publication: The Journal of Physical Chemistry C

Publisher: American Chemical Society

Date: Mar 1, 2018

Copyright © 2018, American Chemical Society

PERMISSION/LICENSE IS GRANTED FOR YOUR ORDER AT NO CHARGE

This type of permission/license, instead of the standard Terms & Conditions, is sent to you because no fee is being charged for your order. Please note the following:

- Permission is granted for your request in both print and electronic formats, and translations.
- If figures and/or tables were requested, they may be adapted or used in part.
- Please print this page for your records and send a copy of it to your publisher/graduate school.
- Appropriate credit for the requested material should be given as follows: "Reprinted (adapted) with permission from (COMPLETE REFERENCE CITATION). Copyright (YEAR) American Chemical Society." Insert appropriate information in place of the capitalized words.
- One-time permission is granted only for the use specified in your request. No additional uses are granted (such as derivative works or other editions). For any other uses, please submit a new request.

BACK CLOSE WINDOW

Counterion condensation or lack of solvation? Understanding the activity of ions in thin film block copolymer electrolytes

Q. Lei, K. Li, D. Bhattacharya, J. Xiao, S. Kole, Q. Zhang, J. Strzalka, J. Lawrence, R. Kumar and C. G. Arges, *J. Mater. Chem. A*, 2020, **8**, 15962
DOI: 10.1039/D0TA04266H

Ionic conductivity and counterion condensation in nanoconfined polycation and polyanion brushes prepared from block copolymer templates

C. G. Arges, K. Li, L. Zhang, Y. Kambe, G. Wu, B. Lwoya, J. N. L. Albert, P. F. Nealey and R. Kumar, *Mol. Syst. Des. Eng.*, 2019, **4**, 365
DOI: 10.1039/C8ME00081F

References

(1) Huang, Y.; Zhao, L.; Li, L.; Xie, M.; Wu, F.; Chen, R. Electrolytes and Electrolyte/Electrode Interfaces in Sodium-Ion Batteries: From Scientific Research to Practical Application. *Advanced Materials* **2019**, *31*, 1808393.

(2) Wahlers, J.; Fulfer, K. D.; Harding, D. P.; Kuroda, D. G.; Kumar, R.; Jorn, R. Solvation Structure and Concentration in Glyme-Based Sodium Electrolytes: A Combined Spectroscopic and Computational Study. *The Journal of Physical Chemistry C* **2016**, *120*, 17949–17959.

(3) Yabuuchi, N.; Kajiyama, M.; Iwatate, J.; Nishikawa, H.; Hitomi, S.; Okuyama, R.; Usui, R.; Yamada, Y.; Komaba, S. P2-type Nax[Fe1/2Mn1/2]O2 made from earth-abundant elements for rechargeable Na batteries. *Nature Materials* **2012**, *11*, 512–517.

(4) Kuboki, T.; Okuyama, T.; Ohsaki, T.; Takami, N. Lithium-air batteries using hydrophobic room temperature ionic liquid electrolyte. *Journal of Power Sources* **2005**, *146*, 766–769.

(5) Beck, F.; Rüetschi, P. Rechargeable batteries with aqueous electrolytes. *Electrochimica Acta* **2000**, *45*, 2467–2482.

(6) Kühnel, R.-S.; Reber, D.; Battaglia, C. A High-Voltage Aqueous Electrolyte for Sodium-Ion Batteries. *ACS Energy Letters* **2017**, *2*, 2005–2006.

(7) Wang, J.; Yamada, Y.; Sodeyama, K.; Watanabe, E.; Takada, K.; Tateyama, Y.; Yamada, A. Fire-extinguishing organic electrolytes for safe batteries. *Nature Energy* **2017**, *3*, 22–29.

(8) Read, J.; Mutolo, K.; Ervin, M.; Behl, W.; Wolfenstine, J.; Driedger, A.; Foster, D. Oxygen Transport Properties of Organic Electrolytes and Performance of Lithium/Oxygen Battery. *Journal of The Electrochemical Society* **2003**, *150*, A1351.

(9) Zhang, H.; Li, C.; Piszcz, M.; Coya, E.; Rojo, T.; Rodriguez-Martinez, L. M.; Armand, M.; Zhou, Z. Single lithium-ion conducting solid polymer electrolytes: advances and perspectives. *Chemical Society Reviews* **2017**, *46*, 797–815.

(10) Michael, M.; Jacob, M.; Prabaharan, S.; Radhakrishna, S. Enhanced lithium ion transport in PEO-based solid polymer electrolytes employing a novel class of plasticizers. *Solid State Ionics* **1997**, *98*, 167–174.

(11) Zhang, J.; Wen, H.; Yue, L.; Chai, J.; Ma, J.; Hu, P.; Ding, G.; Wang, Q.; Liu, Z.; Cui, G.; Chen, L. In Situ Formation of Polysulfonamide Supported Poly(ethylene glycol) Divinyl Ether Based Polymer Electrolyte toward Monolithic Sodium Ion Batteries. *Small* **2016**, *13*, 1601530.

(12) Jung, Y.-C.; Kim, S.-K.; Kim, M.-S.; Lee, J.-H.; Han, M.-S.; Kim, D.-H.; Shin, W.-C.; Ue, M.; Kim, D.-W. Ceramic separators based on Li-conducting inorganic electrolyte for high-performance lithium-ion batteries with enhanced safety. *Journal of Power Sources* **2015**, *293*, 675–683.

(13) Quartarone, E.; Mustarelli, P. Review—Emerging Trends in the Design of Electrolytes for Lithium and Post-Lithium Batteries. *Journal of The Electrochemical Society* **2020**, *167*, 050508.

(14) Yazami, R. Surface chemistry and lithium storage capability of the graphite–lithium electrode. *Electrochimica Acta* **1999**, *45*, 87–97.

(15) Zhang, Y.; Zhao, G.; Lv, X.; Tian, Y.; Yang, L.; Zou, G.; Hou, H.; Zhao, H.; Ji, X. Exploration and Size Engineering from Natural Chalcopyrite to High-Performance Electrode Materials for Lithium-Ion Batteries. *ACS Applied Materials & Interfaces* **2019**, *11*, 6154–6165.

(16) Manthiram, A. An Outlook on Lithium Ion Battery Technology. *ACS Central Science* **2017**, *3*, 1063–1069.

(17) Yabuuchi, N.; Kubota, K.; Dahbi, M.; Komaba, S. Research Development on Sodium-Ion Batteries. *Chemical Reviews* **2014**, *114*, 11636–11682.

(18) Sawicki, M.; Shaw, L. L. Advances and challenges of sodium ion batteries as post lithium ion batteries. *RSC Advances* **2015**, *5*, 53129–53154.

(19) Adelhelm, P.; Hartmann, P.; Bender, C. L.; Busche, M.; Eufinger, C.; Janek, J. From lithium to sodium: cell chemistry of room temperature sodium–air and sodium–sulfur batteries. *Beilstein Journal of Nanotechnology* **2015**, *6*, 1016–1055.

(20) Ishikawa, M.; Sugimoto, T.; Kikuta, M.; Ishiko, E.; Kono, M. Pure ionic liquid electrolytes compatible with a graphitized carbon negative electrode in rechargeable lithium-ion batteries. *Journal of Power Sources* **2006**, *162*, 658–662.

(21) Li, K.; Kankanamge, S. R. G.; Weldeghiorghis, T. K.; Jorn, R.; Kuroda, D. G.; Kumar, R. Predicting Ion Association in Sodium Electrolytes: A Transferrable Model for Investigating Glymes. *The Journal of Physical Chemistry C* **2017**, *122*, 4747–4756.

(22) Kankanamge, S. R. G.; Li, K.; Fulfer, K. D.; Du, P.; Jorn, R.; Kumar, R.; Kuroda, D. G. Mechanism behind the Unusually High Conductivities of High Concentrated Sodium Ion Glyme-Based Electrolytes. *The Journal of Physical Chemistry C* **2018**, *122*, 25237–25246.

(23) Cao, C.; Li, Z.-B.; Wang, X.-L.; Zhao, X.-B.; Han, W.-Q. Recent Advances in Inorganic Solid Electrolytes for Lithium Batteries.*Frontiers in Energy Research* **2014**, *2*.

(24) Yu, X.; Manthiram, A. Electrode–Electrolyte Interfaces in Lithium–Sulfur Batteries with Liquid or Inorganic Solid Electrolytes.*Accounts of Chemical Research* **2017**, *50*, 2653–2660.

(25) Kim, J.-J.; Yoon, K.; Park, I.; Kang, K. Progress in the Development of Sodium-Ion Solid Electrolytes.*Small Methods* **2017**, *1*, 1700219.

(26) Roth, E. P.; Orendorff, C. J. How Electrolytes Influence Battery Safety.*Interface magazine* **2012**, *21*, 45–49.

(27) Xu, K. Nonaqueous Liquid Electrolytes for Lithium-Based Rechargeable Batteries.*Chemical Reviews* **2004**, *104*, 4303–4418.

(28) Chang, Z.; Li, C.; Wang, Y.; Chen, B.; Fu, L.; Zhu, Y.; Zhang, L.; Wu, Y.; Huang, W. A lithium ion battery using an aqueous electrolyte solution.*Scientific Reports* **2016**, *6*, DOI: 10.1038/srep28421.

(29) Chang, Z.; Yang, Y.; Li, M.; Wang, X.; Wu, Y. Green energy storage chemistries based on neutral aqueous electrolytes.*J. Mater. Chem. A* **2014**, *2*, 10739–10755.

(30) Wang, X.; Hou, Y.; Zhu, Y.; Wu, Y.; Holze, R. An Aqueous Rechargeable Lithium Battery Using Coated Li Metal as Anode.*Scientific Reports* **2013**, *3*.

(31) Li, W.; Dahn, J. R.; Wainwright, D. S. Rechargeable Lithium Batteries with Aqueous Electrolytes.*Science* **1994**, *264*, 1115–1118.

(32) Liu, J.; Hu, J.; Deng, Q.; Mo, J.; Xie, H.; Liu, Z.; Xiong, Y.; Wu, X.; Wu, Y. Aqueous Rechargeable Batteries for Large-scale Energy Storage.*Israel Journal of Chemistry* **2015**, *55*, 521–536.

(33) Read, J. Ether-Based Electrolytes for the Lithium/Oxygen Organic Electrolyte Battery.*Journal of The Electrochemical Society* **2006**, *153*, A96.

(34) Cresce, A. V.; Russell, S. M.; Borodin, O.; Allen, J. A.; Schroeder, M. A.; Dai, M.; Peng, J.; Gobet, M. P.; Greenbaum, S. G.; Rogers, R. E.; Xu, K. Solvation behavior of carbonate-based electrolytes in sodium ion batteries.*Physical Chemistry Chemical Physics* **2017**, *19*, 574–586.

(35) Shakourian-Fard, M.; Kamath, G.; Smith, K.; Xiong, H.; Sankaranarayanan, S. K. R. S. Trends in Na-Ion Solvation with Alkyl-Carbonate Electrolytes for

Sodium-Ion Batteries: Insights from First-Principles Calculations. *The Journal of Physical Chemistry C* **2015**, *119*, 22747–22759.

(36) Bhide, A.; Hofmann, J.; Dürr, A. K.; Janek, J.; Adelhelm, P. Electrochemical stability of non-aqueous electrolytes for sodium-ion batteries and their compatibility with Na0.7CoO2. *Phys. Chem. Chem. Phys.* **2014**, *16*, 1987–1998.

(37) Logan, E. R.; Tonita, E. M.; Gering, K. L.; Ma, L.; Bauer, M. K. G.; Li, J.; Beaulieu, L. Y.; Dahn, J. R. A Study of the Transport Properties of Ethylene Carbonate-Free Li Electrolytes. *Journal of The Electrochemical Society* **2018**, *165*, A705–A716.

(38) Zhang, C.; Ueno, K.; Yamazaki, A.; Yoshida, K.; Moon, H.; Mandai, T.; Umebayashi, Y.; Dokko, K.; Watanabe, M. Chelate Effects in Glyme/Lithium Bis (trifluoromethanesulfonyl) amide Solvate Ionic Liquids. I. Stability of Solvate Cations and Correlation with Electrolyte Properties. *The Journal of Physical Chemistry B* **2014**, *118*, 5144–5153.

(39) Ando, H.; Kojima, T.; Takeichi, N.; Watanabe, H.; Umebayashi, Y.; Senoh, H. Mixture of monoglyme-based solvent and lithium Bis(trifluoromethanesulfonyl)amide as electrolyte for lithium ion battery using silicon electrode. *Materials Chemistry and Physics* **2019**, *225*, 105–110.

(40) Henderson, W. A. Glyme-Lithium Salt Phase Behavior. *The Journal of Physical Chemistry B* **2006**, *110*, 13177–13183.

(41) Tamura, T.; Yoshida, K.; Hachida, T.; Tsuchiya, M.; Nakamura, M.; Kazue, Y.; Tachikawa, N.; Dokko, K.; Watanabe, M. Physicochemical Properties of Glyme–Li Salt Complexes as a New Family of Room-temperature Ionic Liquids. *Chemistry Letters* **2010**, *39*, 753–755.

(42) Tamura, T.; Hachida, T.; Yoshida, K.; Tachikawa, N.; Dokko, K.; Watanabe, M. New glyme–cyclic imide lithium salt complexes as thermally stable electrolytes for lithium batteries. *Journal of Power Sources* **2010**, *195*, 6095–6100.

(43) Erickson, E. M.; Markevich, E.; Salitra, G.; Sharon, D.; Hirshberg, D.; de la Llave, E.; Shterenberg, I.; Rosenman, A.; Frimer, A.; Aurbach, D. Review—Development of Advanced Rechargeable Batteries: A Continuous Challenge in the Choice of Suitable Electrolyte Solutions. *Journal of The Electrochemical Society* **2015**, *162*, A2424–A2438.

(44) Rodrıguez-Garcıa, J.; Cameán, I.; Ramos, A.; Rodrıguez, E.; Garcıa, A. B. Graphitic carbon foams as anodes for sodium-ion batteries in glyme-based electrolytes. *Electrochimica Acta* **2018**, *270*, 236–244.

(45) Kajita, T.; Itoh, T. Ether-based solvents significantly improved electrochemical performance for Na-ion batteries with amorphous GeOxanodes.*Physical Chemistry Chemical Physics* **2017**, *19*, 1003–1009.

(46) Wu, F.; Zhu, N.; Bai, Y.; Liu, L.; Zhou, H.; Wu, C. Highly Safe Ionic Liquid Electrolytes for Sodium-Ion Battery: Wide Electrochemical Window and Good Thermal Stability.*ACS Applied Materials & Interfaces* **2016**, *8*, 21381–21386.

(47) Wongittharom, N.; Lee, T.-C.; Wang, C.-H.; Wang, Y.-C.; Chang, J.-K. Electrochemical performance of Na/NaFePO4 sodium-ion batteries with ionic liquid electrolytes.*Journal of Materials Chemistry A* **2014**, *2*, 5655.

(48) Wilken, S.; Xiong, S.; Scheers, J.; Jacobsson, P.; Johansson, P. Ionic liquids in lithium battery electrolytes: Composition versus safety and physical properties.*Journal of Power Sources* **2015**, *275*, 935–942.

(49) Kazemiabnavi, S.; Zhang, Z.; Thornton, K.; Banerjee, S. Electrochemical Stability Window of Imidazolium-Based Ionic Liquids as Electrolytes for Lithium Batteries.*The Journal of Physical Chemistry B* **2016**, *120*, 5691–5702.

(50) Lewandowski, A.; Świderska-Mocek, A. Ionic liquids as electrolytes for Li-ion batteries—An overview of electrochemical studies.*Journal of Power Sources* **2009**, *194*, 601–609.

(51) Li, W.; McKinnon, W. R.; Dahn, J. R. Lithium Intercalation from Aqueous Solutions.*Journal of The Electrochemical Society* **2019**, *141*, 2310–2316.

(52) Liu, T.; Tang, L.; Luo, H.; Cheng, S.; Liu, M. A promising water-in-salt electrolyte for aqueous based electrochemical energy storage cells with a wide potential window: highly concentrated HCOOK.*Chemical Communications* **2019**, *55*, 12817–12820.

(53) Bruce, P. G.; Freunberger, S. A.; Hardwick, L. J.; Tarascon, J.-M. Li–O2 and Li–S batteries with high energy storage.*Nature Materials* **2011**, *11*, 19–29.

(54) Goodenough, J. B.; Park, K.-S. The Li-Ion Rechargeable Battery: A Perspective.*Journal of the American Chemical Society* **2013**, *135*, 1167–1176.

(55) Arges, C. G.; Kambe, Y.; Suh, H. S.; Ocola, L. E.; Nealey, P. F. Perpendicularly Aligned, Anion Conducting Nanochannels in Block Copolymer Electrolyte Films.*Chemistry of Materials* **2016**, *28*, 1377–1389.

(56) Young, W.-S.; Kuan, W.-F.; Epps, T. H. Block copolymer electrolytes for rechargeable lithium batteries.*Journal of Polymer Science Part B: Polymer Physics* **2013**, *52*, 1–16.

(57) Hoarfrost, M. L.; Segalman, R. A. Ionic Conductivity of Nanostructured Block Copolymer/Ionic Liquid Membranes. *Macromolecules* **2011**, *44*, 5281–5288.

(58) Hoarfrost, M. L.; Tyagi, M. S.; Segalman, R. A.; Reimer, J. A. Effect of Confinement on Proton Transport Mechanisms in Block Copolymer/Ionic Liquid Membranes. *Macromolecules* **2012**, *45*, 3112–3120.

(59) Park, M. J.; Balsara, N. P. Phase Behavior of Symmetric Sulfonated Block Copolymers. *Macromolecules* **2008**, *41*, 3678–3687.

(60) Devaux, D.; Glé, D.; Phan, T. N. T.; Gigmes, D.; Giroud, E.; Deschamps, M.; Denoyel, R.; Bouchet, R. Optimization of Block Copolymer Electrolytes for Lithium Metal Batteries. *Chemistry of Materials* **2015**, *27*, 4682–4692.

(61) Tarascon, J.-M.; Armand, M. Issues and challenges facing rechargeable lithium batteries. *Nature* **2001**, *414*, 359–367.

(62) Ohta, N.; Takada, K.; Zhang, L.; Ma, R.; Osada, M.; Sasaki, T. Enhancement of the High-Rate Capability of Solid-State Lithium Batteries by Nanoscale Interfacial Modification. *Advanced Materials* **2006**, *18*, 2226–2229.

(63) Aso, K.; Sakuda, A.; Hayashi, A.; Tatsumisago, M. All-Solid-State Lithium Secondary Batteries Using NiS-Carbon Fiber Composite Electrodes Coated with Li2S–P2S5 Solid Electrolytes by Pulsed Laser Deposition. *ACS Applied Materials & Interfaces* **2013**, *5*, 686–690.

(64) Popov, I.; Sacci, R. L.; Sanders, N. C.; Matsumoto, R. A.; Thompson, M. W.; Osti, N. C.; Kobayashi, T.; Tyagi, M.; Mamontov, E.; Pruski, M.; Cummings, P. T.; Sokolov, A. P. Critical Role of Anion–Solvent Interactions for Dynamics of Solvent-in-Salt Solutions. *The Journal of Physical Chemistry C* **2020**, *124*, 8457–8466.

(65) He, M.; Lau, K. C.; Ren, X.; Xiao, N.; McCulloch, W. D.; Curtiss, L. A.; Wu, Y. Concentrated Electrolyte for the Sodium-Oxygen Battery: Solvation Structure and Improved Cycle Life. *Angewandte Chemie International Edition* **2016**, *55*, 15310–15314.

(66) Arges, C. G.; Li, K.; Zhang, L.; Kambe, Y.; Wu, G.-P.; Lwoya, B.; Albert, J. N. L.; Nealey, P. F.; Kumar, R. Ionic conductivity and counterion condensation in nanoconfined polycation and polyanion brushes prepared from block copolymer templates. *Molecular Systems Design & Engineering* **2019**, *4*, 365–378.

(67) Lei, Q.; Li, K.; Bhattacharya, D.; Xiao, J.; Kole, S.; Zhang, Q.; Strzalka, J.; Lawrence, J.; Kumar, R.; Arges, C. G. Counterion condensation or lack of solvation? Understanding the activity of ions in thin film block copolymer electrolytes. *Journal of Materials Chemistry A* **2020**, DOI: 10.1039/d0ta04266h.

(68) Manning, G. S. Molecular Theory of Counterion Conductivity and Self-Diffusion in Polyelectrolyte Solutions. *The Journal of Chemical Physics* **1967**, *47*, 2010–2013.

(69) Kamcev, J.; Paul, D. R.; Freeman, B. D. Ion Activity Coefficients in Ion Exchange Polymers: Applicability of Manning's Counterion Condensation Theory. *Macromolecules* **2015**, *48*, 8011–8024.

(70) Rivas, B. L.; Moreno-Villoslada, I. Binding of Cd2and NaIons by Poly(sodium 4-styrenesulfonate) Analyzed by Ultrafiltration and Its Relation with the Counterion Condensation Theory. *The Journal of Physical Chemistry B* **1998**, *102*, 6994–6999.

(71) Beers, K. M.; Hallinan, D. T.; Wang, X.; Pople, J. A.; Balsara, N. P. Counterion Condensation in Nafion. *Macromolecules* **2011**, *44*, 8866–8870.

(72) Beers, K. M.; Balsara, N. P. Design of Cluster-free Polymer Electrolyte Membranes and Implications on Proton Conductivity. *ACS Macro Letters* **2012**, *1*, 1155–1160.

(73) Kamcev, J.; Paul, D. R.; Manning, G. S.; Freeman, B. D. Accounting for frame of reference and thermodynamic non-idealities when calculating salt diffusion coefficients in ion exchange membranes. *Journal of Membrane Science* **2017**, *537*, 396–406.

(74) Kamcev, J.; Galizia, M.; Benedetti, F. M.; Jang, E.-S.; Paul, D. R.; Freeman, B. D.; Manning, G. S. Partitioning of mobile ions between ion exchange polymers and aqueous salt solutions: importance of counter-ion condensation. *Physical Chemistry Chemical Physics* **2016**, *18*, 6021–6031.

(75) Kamcev, J.; Paul, D. R.; Manning, G. S.; Freeman, B. D. Predicting Salt Permeability Coefficients in Highly Swollen, Highly Charged Ion Exchange Membranes. *ACS Applied Materials & Interfaces* **2017**, *9*, 4044–4056.

(76) Kamcev, J.; Paul, D. R.; Manning, G. S.; Freeman, B. D. Ion Diffusion Coefficients in Ion Exchange Membranes: Significance of Counterion Condensation. *Macromolecules* **2018**, *51*, 5519–5529.

(77) Xu, K. Electrolytes and Interphases in Li-Ion Batteries and Beyond. *Chemical Reviews* **2014**, *114*, 11503–11618.

(78) Ravikumar, B.; Mynam, M.; Rai, B. Effect of Salt Concentration on Properties of Lithium Ion Battery Electrolytes: A Molecular Dynamics Study. *The Journal of Physical Chemistry C* **2018**, *122*, 8173–8181.

(79) Gachot, G.; Grugeon, S.; Armand, M.; Pilard, S.; Guenot, P.; Tarascon, J.-M.; Laruelle, S. Deciphering the multi-step degradation mechanisms of carbonate-based electrolyte in Li batteries. *Journal of Power Sources* **2008**, *178*, 409–421.

(80) Yamada, Y.; Yaegashi, M.; Abe, T.; Yamada, A. A superconcentrated ether electrolyte for fast-charging Li-ion batteries. *Chemical Communications* **2013**, *49*, 11194.

(81) Yamada, Y.; Furukawa, K.; Sodeyama, K.; Kikuchi, K.; Yaegashi, M.; Tateyama, Y.; Yamada, A. Unusual Stability of Acetonitrile-Based Superconcentrated Electrolytes for Fast-Charging Lithium-Ion Batteries. *Journal of the American Chemical Society* **2014**, *136*, 5039–5046.

(82) Ren, X.; Zou, L.; Jiao, S.; Mei, D.; Engelhard, M. H.; Li, Q.; Lee, H.; Niu, C.; Adams, B. D.; Wang, C.; Liu, J.; Zhang, J.-G.; Xu, W. High-Concentration Ether Electrolytes for Stable High-Voltage Lithium Metal Batteries. *ACS Energy Letters* **2019**, *4*, 896–902.

(83) Lutz, L.; Yin, W.; Grimaud, A.; Corte, D. A. D.; Tang, M.; Johnson, L.; Azaceta, E.; Sarou-Kanian, V.; Naylor, A. J.; Hamad, S.; Anta, J. A.; Salager, E.; Tena-Zaera, R.; Bruce, P. G.; Tarascon, J.-M. High Capacity Na–O2 Batteries: Key Parameters for Solution-Mediated Discharge. *The Journal of Physical Chemistry C* **2016**, *120*, 20068–20076.

(84) Kaulgud, T. V.; Dhumal, N. R.; Gejji, S. P. Electronic Structure and Normal Vibrations of CH3(OCH2CH2)nOCH3-M-CF3SO3-(n= 2-4, M = Li, Na, and K). *The Journal of Physical Chemistry A* **2006**, *110*, 9231–9239.

(85) Dhumal, N. R.; Gejji, S. P. Theoretical studies in local coordination and vibrational spectra of MCH3O(CH2CH2O)nCH3 (n=2–7) complexes (M=Na, K, Mg and Ca). *Chemical Physics* **2006**, *323*, 595–605.

(86) Jorn, R.; Kumar, R.; Abraham, D. P.; Voth, G. A. Atomistic Modeling of the Electrode–Electrolyte Interface in Li-Ion Energy Storage Systems: Electrolyte Structuring. *The Journal of Physical Chemistry C* **2013**, *117*, 3747–3761.

(87) Izvekov, S.; Parrinello, M.; Burnham, C. J.; Voth, G. A. Effective force fields for condensed phase systems from ab initio molecular dynamics simulation: A new method for force-matching. *The Journal of Chemical Physics* **2004**, *120*, 10896–10913.

(88) Ercolessi, F.; Adams, J. B. Interatomic Potentials from First-Principles Calculations: The Force-Matching Method. *Europhysics Letters (EPL)* **1994**, *26*, 583–588.

(89) Li, N.; Guiver, M. D. Ion Transport by Nanochannels in Ion-Containing Aromatic Copolymers. *Macromolecules* **2014**, *47*, 2175–2198.

(90) Kambe, Y.; Arges, C. G.; Patel, S.; Stoykovish, M. P.; Nealey, P. F. Ion Conduction in Microphase-Separated Block Copolymer Electrolytes. *The Electrochemical Society Interface* **2017**, *26*, 61–67.

(91) Kim, S.-K.; Kim, D.-G.; Lee, A.; Sohn, H.-S.; Wie, J. J.; Nguyen, N. A.; Mackay, M. E.; Lee, J.-C. Organic/Inorganic Hybrid Block Copolymer Electrolytes with Nanoscale Ion-Conducting Channels for Lithium Ion Batteries. *Macromolecules* **2012**, *45*, 9347–9356.

(92) Shi, F.; Ross, P. N.; Somorjai, G. A.; Komvopoulos, K. The Chemistry of Electrolyte Reduction on Silicon Electrodes Revealed by in Situ ATR-FTIR Spectroscopy. *The Journal of Physical Chemistry C* **2017**, *121*, 14476–14483.

(93) Bao, L.; Zou, X.; Luo, X.; Pu, Y.; Wang, J.; Lei, J. Real-time tracking the Li-ion transition behavior and dynamics in solid Poly(vinyl alcohol)/LiClO4 electrolytes. *Scientific Reports* **2017**, *7*, DOI: 10.1038/srep45921.

(94) Aziz, S. B.; Hamsan, M. H.; Kadir, M. F. Z.; Karim, W. O.; Abdullah, R. M. Development of Polymer Blend Electrolyte Membranes Based on Chitosan: Dextran with High Ion Transport Properties for EDLC Application. *International Journal of Molecular Sciences* **2019**, *20*, 3369.

(95) Lee, J.; Lee, Y.; Lee, J.; Lee, S.-M.; Choi, J.-H.; Kim, H.; Kwon, M.-S.; Kang, K.; Lee, K. T.; Choi, N.-S. Ultraconcentrated Sodium Bis(fluorosulfonyl)imide-Based Electrolytes for High-Performance Sodium Metal Batteries. *ACS Applied Materials & Interfaces* **2017**, *9*, 3723–3732.

(96) Fulfer, K. D.; Kuroda, D. G. Solvation Structure and Dynamics of the Lithium Ion in Organic Carbonate-Based Electrolytes: A Time-Dependent Infrared Spectroscopy Study. *The Journal of Physical Chemistry C* **2016**, *120*, 24011–24022.

(97) Fulfer, K. D.; Kuroda, D. G. A comparison of the solvation structure and dynamics of the lithium ion in linear organic carbonates with different alkyl chain lengths. *Physical Chemistry Chemical Physics* **2017**, *19*, 25140–25150.

(98) Kankanamge, S. R. G.; Kuroda, D. G. Molecular structure and ultrafast dynamics of sodium thiocyanate ion pairs formed in glymes of different lengths. *Physical Chemistry Chemical Physics* **2019**, *21*, 833–841.

(99) Munoz, S.; Greenbaum, S. Review of Recent Nuclear Magnetic Resonance Studies of Ion Transport in Polymer Electrolytes. *Membranes* **2018**, *8*, 120.

(100) Uitz, M.; Epp, V.; Bottke, P.; Wilkening, M. Ion dynamics in solid electrolytes for lithium batteries. *Journal of Electroceramics* **2017**, *38*, 142–156.

(101) Davidowski, S. K.; Yarger, J. L.; Richert, R.; Angell, C. A. Reorientation Times for Solid-State Electrolyte Solvents and Electrolytes from NMR Spin–Lattice Relaxation Studies. *The Journal of Physical Chemistry Letters* **2020**, *11*, 3301–3304.

(102) Bogle, X.; Vazquez, R.; Greenbaum, S.; von Wald Cresce, A.; Xu, K. Understanding Li–Solvent Interaction in Nonaqueous Carbonate Electrolytes with 17O NMR. *The Journal of Physical Chemistry Letters* **2013**, *4*, 1664–1668.

(103) Van Gunsteren, W. F.; Berendsen, H. J. C. Computer Simulation of Molecular Dynamics: Methodology, Applications, and Perspectives in Chemistry. *Angewandte Chemie International Edition in English* **1990**, *29*, 992–1023.

(104) Singh, U. C.; Kollman, P. A. A combinedab initio quantum mechanical and molecular mechanical method for carrying out simulations on complex molecular systems: Applications to the CH3Cl Cl? exchange reaction and gas phase protonation of polyethers. *Journal of Computational Chemistry* **1986**, *7*, 718–730.

(105) Mackerell, A. D.; Feig, M.; Brooks, C. L. Extending the treatment of backbone energetics in protein force fields: Limitations of gas-phase quantum mechanics in reproducing protein conformational distributions in molecular dynamics simulations. *Journal of Computational Chemistry* **2004**, *25*, 1400–1415.

(106) Pópolo, M. G. D.; Lynden-Bell, R. M.; Kohanoff, J. Ab Initio Molecular Dynamics Simulation of a Room Temperature Ionic Liquid. *The Journal of Physical Chemistry B* **2005**, *109*, 5895–5902.

(107) Abroshan, H.; Dhumal, N. R.; Shim, Y.; Kim, H. J. Theoretical study of interactions of a Li(CF3SO2)2N- ion pair with CR3(OCR2CR2)nOCR3 (R = H or F). *Physical Chemistry Chemical Physics* **2016**, *18*, 6754–6762.

(108) Dhumal, N. R.; Gejji, S. P. Theoretical Studies on Blue versus Red Shifts in Diglyme-M-X-(M = Li, Na, and K and X = CF3SO3, PF6, and (CF3SO2)2N)). *The Journal of Physical Chemistry A* **2006**, *110*, 219–227.

(109) Sun, H.; Ren, P.; Fried, J. The COMPASS force field: parameterization and validation for phosphazenes. *Computational and Theoretical Polymer Science* **1998**, *8*, 229–246.

(110) Halgren, T. A. Merck molecular force field. I. Basis, form, scope, parameterization, and performance of MMFF94. *Journal of Computational Chemistry* **1996**, *17*, 490–519.

(111) Jorgensen, W. L.; Maxwell, D. S.; Tirado-Rives, J. Development and Testing of the OPLS All-Atom Force Field on Conformational Energetics and Properties of Organic Liquids. *Journal of the American Chemical Society* **1996**, *118*, 11225–11236.

(112) Lopes, J. N. C.; Pádua, A. A. H. Molecular Force Field for Ionic Liquids Composed of Triflate or Bistriflylimide Anions. *The Journal of Physical Chemistry B* **2004**, *108*, 16893–16898.

(113) Elber, R.; Karplus, M. Multiple conformational states of proteins: a molecular dynamics analysis of myoglobin. *Science* **1987**, *235*, 318–321.

(114) Caves, L. S. D.; Evanseck, J. D.; Karplus, M. Locally accessible conformations of proteins: Multiple molecular dynamics simulations of crambin. *Protein Science* **1998**, *7*, 649–666.

(115) Schlitter, J.; Engels, M.; Krüger, P. Targeted molecular dynamics: A new approach for searching pathways of conformational transitions. *Journal of Molecular Graphics* **1994**, *12*, 84–89.

(116) Hamal, P.; Nguyenhuu, H.; Don, V. S.; Kumal, R. R.; Kumar, R.; McCarley, R. L.; Haber, L. H. Molecular Adsorption and Transport at Liposome Surfaces Studied by Molecular Dynamics Simulations and Second Harmonic Generation Spectroscopy. *The Journal of Physical Chemistry B* **2019**, *123*, 7722–7730.

(117) Don, V. S.; David, R.; Du, P.; Milet, A.; Kumar, R. Interfacial Water at Graphene Oxide Surface: Ordered or Disordered? *The Journal of Physical Chemistry B* **2019**, *123*, 1636–1649.

(118) Coveney, P. V.; Wan, S. On the calculation of equilibrium thermodynamic properties from molecular dynamics. *Physical Chemistry Chemical Physics* **2016**, *18*, 30236–30240.

(119) Briant, C. L.; Burton, J. J. Molecular dynamics study of the structure and thermodynamic properties of argon microclusters. *The Journal of Chemical Physics* **1975**, *63*, 2045–2058.

(120) Lin, S.-T.; Blanco, M.; Goddard, W. A. The two-phase model for calculating thermodynamic properties of liquids from molecular dynamics: Validation for the phase diagram of Lennard-Jones fluids. *The Journal of Chemical Physics* **2003**, *119*, 11792–11805.

(121) Bisoi, S.; Mandal, A. K.; Padmanabhan, V.; Banerjee, S. Aromatic polyamides containing trityl substituted triphenylamine: Gas transport properties and molecular dynamics simulations. *Journal of Membrane Science* **2017**, *522*, 77–90.

(122) Hardy, J.; de Pazzis, O.; Pomeau, Y. Molecular dynamics of a classical lattice gas: Transport properties and time correlation functions. *Physical Review A* **1976**, *13*, 1949–1961.

(123) Basconi, J. E.; Shirts, M. R. Effects of Temperature Control Algorithms on Transport Properties and Kinetics in Molecular Dynamics Simulations. *Journal of Chemical Theory and Computation* **2013**, *9*, 2887–2899.

(124) Pomès, R.; McCammon, J. Mass and step length optimization for the calculation of equilibrium properties by molecular dynamics simulation. *Chemical Physics Letters* **1990**, *166*, 425–428.

(125) Evans, M. W. Molecular dynamics simulation of induced anisotropy. I. Equilibrium properties. *The Journal of Chemical Physics* **1982**, *76*, 5473–5479.

(126) Dang, L. X. Intermolecular interactions of liquid dichloromethane and equilibrium properties of liquid–vapor and liquid–liquid interfaces: A molecular dynamics study. *The Journal of Chemical Physics* **1999**, *110*, 10113–10122.

(127) Soga, K.; Inoue, H.; Makishima, A. Calculation and simulation of spectroscopic properties for rare earth ions in chloro-fluorozirconate glasses. *Journal of Non-Crystalline Solids* **2000**, *274*, 69–74.

(128) Danten, Y.; Tassaing, T.; Besnard, M. Molecular Dynamics of Monomeric Water Dissolved in Very Hydrophobic Solvents: the Current State of the Art of Vibrational Spectroscopy Analyzed from Analytical Model and MD Simulations. *The Journal of Physical Chemistry A* **2000**, *104*, 9415–9427.

(129) Bursulaya, B. D.; Kim, H. J. Spectroscopic and dielectric properties of liquid water: A molecular dynamics simulation study. *The Journal of Chemical Physics* **1998**, *109*, 4911–4919.

(130) Martínez, L.; Andrade, R.; Birgin, E. G.; Martínez, J. M. PACKMOL: A package for building initial configurations for molecular dynamics simulations. *Journal of Computational Chemistry* **2009**, *30*, 2157–2164.

(131) Soteras Gutiérrez, I.; Lin, F.-Y.; Vanommeslaeghe, K.; Lemkul, J. A.; Armacost, K. A.; Brooks, C. L.; MacKerell, A. D. Parametrization of halogen bonds in the CHARMM general force field: Improved treatment of ligand–protein interactions. *Bioorganic & Medicinal Chemistry* **2016**, *24*, 4812–4825.

(132) Yu, W.; He, X.; Vanommeslaeghe, K.; MacKerell Jr., A. D. Extension of the CHARMM general force field to sulfonyl-containing compounds and its utility in biomolecular simulations. *Journal of Computational Chemistry* **2012**, *33*, 2451–2468.

(133) Vanommeslaeghe, K.; Raman, E. P.; MacKerell, A. D. Automation of the CHARMM General Force Field (CGenFF) II: Assignment of Bonded Parameters and Partial Atomic Charges. *Journal of Chemical Information and Modeling* **2012**, *52*, 3155–3168.

(134) Vanommeslaeghe, K.; MacKerell, A. D. Automation of the CHARMM General Force Field (CGenFF) I: Bond Perception and Atom Typing. *Journal of Chemical Information and Modeling* **2012**, *52*, 3144–3154.

(135) Vanommeslaeghe, K.; Hatcher, E.; Acharya, C.; Kundu, S.; Zhong, S.; Shim, J.; Darian, E.; Guvench, O.; Lopes, P.; Vorobyov, I.; Mackerell Jr., A. D. CHARMM general force field: A force field for drug-like molecules compatible with the CHARMM all-atom additive biological force fields. *Journal of Computational Chemistry* **2010**, *31*, 671–690.

(136) Wang, J.; Wolf, R. M.; Caldwell, J. W.; Kollman, P. A.; Case, D. A. Development and testing of a general amber force field. *Journal of Computational Chemistry* **2004**, *25*, 1157–1174.

(137) Ewig, C. S.; Thacher, T. S.; Hagler, A. T. Derivation of Class II Force Fields. 7. Nonbonded Force Field Parameters for Organic Compounds. *The Journal of Physical Chemistry B* **1999**, *103*, 6998–7014.

(138) Ponder, J. W.; Wu, C.; Ren, P.; Pande, V. S.; Chodera, J. D.; Schnieders, M. J.; Haque, I.; Mobley, D. L.; Lambrecht, D. S.; DiStasio, R. A.; Head-Gordon, M.; Clark, G. N. I.; Johnson, M. E.; Head-Gordon, T. Current Status of the AMOEBA Polarizable Force Field. *The Journal of Physical Chemistry B* **2010**, *114*, 2549–2564.

(139) Verlet, L. Computer "Experiments" on Classical Fluids. I. Thermodynamical Properties of Lennard-Jones Molecules. *Physical Review* **1967**, *159*, 98–103.

(140) Birdsall, C.; Langdon, A., *Plasma Physics via Computer Simulation*; Series in Plasma Physics and Fluid Dynamics; Taylor & Francis: 2004.

(141) Andersen, H. C. Molecular dynamics simulations at constant pressure and/or temperature. *The Journal of Chemical Physics* **1980**, *72*, 2384–2393.

(142) Berendsen, H. J. C.; Postma, J. P. M.; van Gunsteren, W. F.; DiNola, A.; Haak, J. R. Molecular dynamics with coupling to an external bath. *The Journal of Chemical Physics* **1984**, *81*, 3684–3690.

(143) Posch, H. A.; Hoover, W. G.; Vesely, F. J. Canonical dynamics of the Nosé oscillator: Stability, order, and chaos. *Physical Review A* **1986**, *33*, 4253–4265.

(144) Hoover, W. G. Canonical dynamics: Equilibrium phase-space distributions. *Physical Review A* **1985**, *31*, 1695–1697.

(145) Nosé, S. A molecular dynamics method for simulations in the canonical ensemble. *Molecular Physics* **1984**, *52*, 255–268.

(146) Parrinello, M.; Rahman, A. Polymorphic transitions in single crystals: A new molecular dynamics method. *Journal of Applied Physics* **1981**, *52*, 7182–7190.

(147) Dror, R. O.; Jensen, M. Ø.; Borhani, D. W.; Shaw, D. E. Exploring atomic resolution physiology on a femtosecond to millisecond timescale using molecular dynamics simulations. *The Journal of General Physiology* **2010**, *135*, 555–562.

(148) Roger W Hockney, J. W. E., *Computer simulation using particles*; Bristol [England],Philadelphia : A. Hilger, ©1988.: 1988.

(149) Torrie, G. M.; Valleau, J. P. Nonphysical sampling distributions in Monte Carlo free-energy estimation: Umbrella sampling. *Journal of Computational Physics* **1977**, *23*, 187–199.

(150) Swendsen, R. H.; Wang, J.-S. Replica Monte Carlo Simulation of Spin-Glasses. *Physical Review Letters* **1986**, *57*, 2607–2609.

(151) Laio, A.; Parrinello, M. Escaping free-energy minima. *Proceedings of the National Academy of Sciences* **2002**, *99*, 12562–12566.

(152) CHAU, P.-L.; HARDWICK, A. J. A new order parameter for tetrahedral configurations. *Molecular Physics* **1998**, *93*, 511–518.

(153) Errington, J. R.; Debenedetti, P. G. Relationship between structural order and the anomalies of liquid water. *Nature* **2001**, *409*, 318–321.

(154) Duboué-Dijon, E.; Laage, D. Characterization of the Local Structure in Liquid Water by Various Order Parameters. *The Journal of Physical Chemistry B* **2015**, *119*, 8406–8418.

(155) Kumar, R.; Skinner, J. L. Water Simulation Model with Explicit Three-Molecule Interactions. *The Journal of Physical Chemistry B* **2008**, *112*, 8311–8318.

(156) France-Lanord, A.; Grossman, J. C. Correlations from Ion Pairing and the Nernst-Einstein Equation. *Physical Review Letters* **2019**, *122*, DOI: 10.1103/physrevlett.122.136001.

(157) Faraudo, J.; Calero, C.; Aguilella-Arzo, M. Ionic Partition and Transport in Multi-Ionic Channels: A Molecular Dynamics Simulation Study of the OmpF Bacterial Porin. *Biophysical Journal* **2010**, *99*, 2107–2115.

(158) Ridley, M. The Rational Optimist: How Prosperity Evolves. *Brock Education Journal* **2012**, *21*.

(159) Perera, F. Pollution from Fossil-Fuel Combustion is the Leading Environmental Threat to Global Pediatric Health and Equity: Solutions Exist. *International Journal of Environmental Research and Public Health* **2017**, *15*, 16.

(160) Qureshi, M. I.; Rasli, A. M.; Zaman, K. Energy crisis, greenhouse gas emissions and sectoral growth reforms: repairing the fabricated mosaic. *Journal of Cleaner Production* **2016**, *112*, 3657–3666.

(161) Chu, S.; Majumdar, A. Opportunities and challenges for a sustainable energy future. *Nature* **2012**, *488*, 294–303.

(162) Choi, N.-S.; Chen, Z.; Freunberger, S. A.; Ji, X.; Sun, Y.-K.; Amine, K.; Yushin, G.; Nazar, L. F.; Cho, J.; Bruce, P. G. Challenges Facing Lithium Batteries and Electrical Double-Layer Capacitors. *Angewandte Chemie International Edition* **2012**, *51*, 9994–10024.

(163) Evanoff, K.; Benson, J.; Schauer, M.; Kovalenko, I.; Lashmore, D.; Ready, W. J.; Yushin, G. Ultra Strong Silicon-Coated Carbon Nanotube Nonwoven Fabric as a Multifunctional Lithium-Ion Battery Anode. *ACS Nano* **2012**, *6*, 9837–9845.

(164) Yoo, H. D.; Markevich, E.; Salitra, G.; Sharon, D.; Aurbach, D. On the challenge of developing advanced technologies for electrochemical energy storage and conversion. *Materials Today* **2014**, *17*, 110–121.

(165) Pollet, B. G.; Kocha, S. S.; Staffell, I. Current status of automotive fuel cells for sustainable transport. *Current Opinion in Electrochemistry* **2019**, *16*, 90–95.

(166) Lee, J.-S.; Kim, S. T.; Cao, R.; Choi, N.-S.; Liu, M.; Lee, K. T.; Cho, J. Metal-Air Batteries with High Energy Density: Li-Air versus Zn-Air. *Advanced Energy Materials* **2010**, *1*, 34–50.

(167) Rui, K.; Wen, Z.; Lu, Y.; Jin, J.; Shen, C. One-Step Solvothermal Synthesis of Nanostructured Manganese Fluoride as an Anode for Rechargeable Lithium-Ion Batteries and Insights into the Conversion Mechanism. *Advanced Energy Materials* **2015**, *5*, 1401716.

(168) Ellis, B. L.; Nazar, L. F. Sodium and sodium-ion energy storage batteries. *Current Opinion in Solid State and Materials Science* **2012**, *16*, 168–177.

(169) Girishkumar, G.; McCloskey, B.; Luntz, A. C.; Swanson, S.; Wilcke, W. Lithium-Air Battery: Promise and Challenges. *The Journal of Physical Chemistry Letters* **2010**, *1*, 2193–2203.

(170) Ogasawara, T.; Débart, A.; Holzapfel, M.; Novák, P.; Bruce, P. G. Rechargeable Li2O2Electrode for Lithium Batteries. *Journal of the American Chemical Society* **2006**, *128*, 1390–1393.

(171) Rahman, M. A.; Wang, X.; Wen, C. A review of high energy density lithium–air battery technology. *Journal of Applied Electrochemistry* **2013**, *44*, 5–22.

(172) Hartmann, P.; Bender, C. L.; Vračar, M.; Dürr, A. K.; Garsuch, A.; Janek, J.; Adelhelm, P. A rechargeable room-temperature sodium superoxide (NaO2) battery. *Nature Materials* **2013**, *12*, 228–232.

(173) Kim, J.; Lim, H.-D.; Gwon, H.; Kang, K. Sodium–oxygen batteries with alkyl-carbonate and ether based electrolytes. *Phys. Chem. Chem. Phys.* **2013**, *15*, 3623–3629.

(174) Sun, Q.; Yang, Y.; Fu, Z.-W. Electrochemical properties of room temperature sodium–air batteries with non-aqueous electrolyte. *Electrochemistry Communications* **2012**, *16*, 22–25.

(175) Hartmann, P.; Bender, C. L.; Sann, J.; Dürr, A. K.; Jansen, M.; Janek, J.; Adelhelm, P. A comprehensive study on the cell chemistry of the sodium superoxide (NaO2) battery. *Physical Chemistry Chemical Physics* **2013**, *15*, 11661.

(176) Sangster, J.; Pelton, A. D. The Li-O (lithium-oxygen) system. *Journal of Phase Equilibria* **1992**, *13*, 296–299.

(177) Wriedt, H. A. The Na-O (Sodium-Oxygen) System. *Bulletin of Alloy Phase Diagrams* **1987**, *8*, 234–246.

(178) Peng, Z.; Freunberger, S. A.; Hardwick, L. J.; Chen, Y.; Giordani, V.; Bardé, F.; Novák, P.; Graham, D.; Tarascon, J.-M.; Bruce, P. G. Oxygen Reactions in a Non-Aqueous Li+ Electrolyte. *Angewandte Chemie International Edition* **2011**, *50*, 6351–6355.

(179) Das, S. K.; Lau, S.; Archer, L. A. Sodium–oxygen batteries: a new class of metal–air batteries. *Journal of Materials Chemistry A* **2014**, *2*, 12623.

(180) McCloskey, B. D.; Garcia, J. M.; Luntz, A. C. Chemical and Electrochemical Differences in Nonaqueous Li–O2and Na–O2Batteries. *The Journal of Physical Chemistry Letters* **2014**, *5*, 1230–1235.

(181) Luntz, A. C.; McCloskey, B. D. Nonaqueous Li–Air Batteries: A Status Report. *Chemical Reviews* **2014**, *114*, 11721–11750.

(182) Che, H.; Chen, S.; Xie, Y.; Wang, H.; Amine, K.; Liao, X.-Z.; Ma, Z.-F. Electrolyte design strategies and research progress for room-temperature sodium-ion batteries. *Energy Environ. Sci.* **2017**, *10*, 1075–1101.

(183) EM, E.; E, M.; G, S.; D, S.; D, H.; de la Llave E; I, S.; A, R.; A, F.; D, A. Review-Development of Advanced Rechargeable Batteries: A Continuous Challenge in the Choice of Suitable Electrolyte Solutions (vol 162, pg A2424, 2015). *Journal of the Electrochemical Society* **2017**, *164*, X5–X5.

(184) Aurbach, D.; Talyosef, Y.; Markovsky, B.; Markevich, E.; Zinigrad, E.; Asraf, L.; Gnanaraj, J. S.; Kim, H.-J. Design of electrolyte solutions for Li and Li-ion batteries: a review. *Electrochimica Acta* **2004**, *50*, 247–254.

(185) Ponrouch, A.; Dedryvère, R.; Monti, D.; Demet, A. E.; Mba, J. M. A.; Croguennec, L.; Masquelier, C.; Johansson, P.; Palacın, M. R. Towards high energy density sodium ion batteries through electrolyte optimization. *Energy & Environmental Science* **2013**, *6*, 2361.

(186) Kumar, H.; Detsi, E.; Abraham, D. P.; Shenoy, V. B. Fundamental Mechanisms of Solvent Decomposition Involved in Solid-Electrolyte Interphase Formation in Sodium Ion Batteries. *Chemistry of Materials* **2016**, *28*, 8930–8941.

(187) Zhao, N.; Guo, X. Cell Chemistry of Sodium–Oxygen Batteries with Various Non-aqueous Electrolytes. *The Journal of Physical Chemistry C* **2015**, *119*, 25319–25326.

(188) Jian, Z.; Chen, Y.; Li, F.; Zhang, T.; Liu, C.; Zhou, H. High capacity Na–O2 batteries with carbon nanotube paper as binder-free air cathode. *Journal of Power Sources* **2014**, *251*, 466–469.

(189) Elia, G. A.; Hasa, I.; Hassoun, J. Characterization of a reversible, low-polarization sodium-oxygen battery. *Electrochimica Acta* **2016**, *191*, 516–520.

(190) Mandai, T.; Nozawa, R.; Tsuzuki, S.; Yoshida, K.; Ueno, K.; Dokko, K.; Watanabe, M. Phase Diagrams and Solvate Structures of Binary Mixtures of Glymes and Na Salts. *The Journal of Physical Chemistry B* **2013**, *117*, 15072–15085.

(191) Kamath, G.; Cutler, R. W.; Deshmukh, S. A.; Shakourian-Fard, M.; Parrish, R.; Huether, J.; Butt, D. P.; Xiong, H.; Sankaranarayanan, S. K. R. S. In Silico Based Rank-Order Determination and Experiments on Nonaqueous Electrolytes for Sodium Ion Battery Applications. *The Journal of Physical Chemistry C* **2014**, *118*, 13406–13416.

(192) Flores, E.; Åvall, G.; Jeschke, S.; Johansson, P. Solvation structure in dilute to highly concentrated electrolytes for lithium-ion and sodium-ion batteries. *Electrochimica Acta* **2017**, *233*, 134–141.

(193) Tsuzuki, S.; Mandai, T.; Suzuki, S.; Shinoda, W.; Nakamura, T.; Morishita, T.; Ueno, K.; Seki, S.; Umebayashi, Y.; Dokko, K.; Watanabe, M. Effect of the cation on the stability of cation–glyme complexes and their interactions with the [TFSA]-anion. *Phys. Chem. Chem. Phys.* **2017**, *19*, 18262–18272.

(194) Yoshida, K.; Nakamura, M.; Kazue, Y.; Tachikawa, N.; Tsuzuki, S.; Seki, S.; Dokko, K.; Watanabe, M. Oxidative-Stability Enhancement and Charge Transport Mecha-

nism in Glyme–Lithium Salt Equimolar Complexes. *Journal of the American Chemical Society* **2011**, *133*, 13121–13129.

(195) Jache, B.; Binder, J. O.; Abe, T.; Adelhelm, P. A comparative study on the impact of different glymes and their derivatives as electrolyte solvents for graphite co-intercalation electrodes in lithium-ion and sodium-ion batteries. *Physical Chemistry Chemical Physics* **2016**, *18*, 14299–14316.

(196) Maibach, J.; Jeschull, F.; Brandell, D.; Edström, K.; Valvo, M. Surface Layer Evolution on Graphite During Electrochemical Sodium-tetraglyme Co-intercalation. *ACS Applied Materials & Interfaces* **2017**, *9*, 12373–12381.

(197) Cabello, M.; Chyrka, T.; Klee, R.; Aragón, M. J.; Bai, X.; Lavela, P.; Vasylchenko, G. M.; Alcántara, R.; Tirado, J. L.; Ortiz, G. F. Treasure Na-ion anode from trash coke by adept electrolyte selection. *Journal of Power Sources* **2017**, *347*, 127–135.

(198) Nasybulin, E.; Xu, W.; Engelhard, M. H.; Nie, Z.; Burton, S. D.; Cosimbescu, L.; Gross, M. E.; Zhang, J.-G. Effects of Electrolyte Salts on the Performance of Li–O2 Batteries. *The Journal of Physical Chemistry C* **2013**, *117*, 2635–2645.

(199) Yamada, Y.; Yamada, A. Review—Superconcentrated Electrolytes for Lithium Batteries. *Journal of The Electrochemical Society* **2015**, *162*, A2406–A2423.

(200) Ding, Y.; Yun, J.; Liu, H.; Wan, Z.; Shen, M.; Zhang, L.; Qu, Q.; Zheng, H. A safe and superior propylene carbonate-based electrolyte with high-concentration Li salt. *Pure and Applied Chemistry* **2014**, *86*, 585–591.

(201) Lee, D.-J.; Park, J.-W.; Hasa, I.; Sun, Y.-K.; Scrosati, B.; Hassoun, J. Alternative materials for sodium ion–sulphur batteries. *Journal of Materials Chemistry A* **2013**, *1*, 5256.

(202) Carbone, L.; Munoz, S.; Gobet, M.; Devany, M.; Greenbaum, S.; Hassoun, J. Characteristics of glyme electrolytes for sodium battery: nuclear magnetic resonance and electrochemical study. *Electrochimica Acta* **2017**, *231*, 223–229.

(203) Kim, H.; Park, J.-S.; Sahgong, S. H.; Park, S.; Kim, J.-K.; Kim, Y. Metal-free hybrid seawater fuel cell with an ether-based electrolyte. *J. Mater. Chem. A* **2014**, *2*, 19584–19588.

(204) Heinz, H.; Koerner, H.; Anderson, K. L.; Vaia, R. A.; Farmer, B. L. Force Field for Mica-Type Silicates and Dynamics of Octadecylammonium Chains Grafted to Montmorillonite. *Chemistry of Materials* **2005**, *17*, 5658–5669.

(205) Breneman, C. M.; Wiberg, K. B. Determining atom-centered monopoles from molecular electrostatic potentials. The need for high sampling density in formamide conformational analysis. *Journal of Computational Chemistry* **1990**, *11*, 361–373.

(206) Frisch, M. J. et al. Gaussian09 Revision E.01, Gaussian Inc. Wallingford CT 2009.

(207) Hanwell, M. D.; Curtis, D. E.; Lonie, D. C.; Vandermeersch, T.; Zurek, E.; Hutchison, G. R. Avogadro: an advanced semantic chemical editor, visualization, and analysis platform. *Journal of Cheminformatics* **2012**, *4*, 17.

(208) Plimpton, S. *Fast parallel algorithms for short-range molecular dynamics*; tech. rep.; United States, 1993.

(209) Okoshi, M.; Chou, C.-P.; Nakai, H. Theoretical Analysis of Carrier Ion Diffusion in Superconcentrated Electrolyte Solutions for Sodium-Ion Batteries. *The Journal of Physical Chemistry B* **2018**, *122*, 2600–2609.

(210) XU, T. Ion exchange membranes: State of their development and perspective. *Journal of Membrane Science* **2005**, *263*, 1–29.

(211) Krol, J. Concentration polarization with monopolar ion exchange membranes: currentâvoltage curves and water dissociation. *Journal of Membrane Science* **1999**, *162*, 145–154.

(212) LI, H.; GAO, Y.; PAN, L.; ZHANG, Y.; CHEN, Y.; SUN, Z. Electrosorptive desalination by carbon nanotubes and nanofibres electrodes and ion-exchange membranes. *Water Research* **2008**, *42*, 4923–4928.

(213) Kariduraganavar, M.; Nagarale, R.; Kittur, A.; Kulkarni, S. Ion-exchange membranes: preparative methods for electrodialysis and fuel cell applications. *Desalination* **2006**, *197*, 225–246.

(214) Leong, J. X.; Daud, W. R. W.; Ghasemi, M.; Liew, K. B.; Ismail, M. Ion exchange membranes as separators in microbial fuel cells for bioenergy conversion: A comprehensive review. *Renewable and Sustainable Energy Reviews* **2013**, *28*, 575–587.

(215) Flint, S. D.; Slade, R. C. Investigation of radiation-grafted PVDF-g-polystyrenesulfonic-acid ion exchange membranes for use in hydrogen oxygen fuel cells. *Solid State Ionics* **1997**, *97*, 299–307.

(216) Nataraj, S.; Hosamani, K.; Aminabhavi, T. Potential application of an electrodialysis pilot plant containing ion-exchange membranes in chromium removal. *Desalination* **2007**, *217*, 181–190.

(217) Strathmann, H.; Grabowski, A.; Eigenberger, G. Ion-Exchange Membranes in the Chemical Process Industry.*Industrial & Engineering Chemistry Research* **2013**, *52*, 10364–10379.

(218) Ran, J.; Wu, L.; He, Y.; Yang, Z.; Wang, Y.; Jiang, C.; Ge, L.; Bakangura, E.; Xu, T. Ion exchange membranes: New developments and applications.*Journal of Membrane Science* **2017**, *522*, 267–291.

(219) Palakkal, V. M.; Rubio, J. E.; Lin, Y. J.; Arges, C. G. Low-Resistant Ion-Exchange Membranes for Energy Efficient Membrane Capacitive Deionization.*ACS Sustainable Chemistry & Engineering* **2018**, *6*, 13778–13786.

(220) Ramon, G. Z.; Feinberg, B. J.; Hoek, E. M. V. Membrane-based production of salinity-gradient power.*Energy & Environmental Science* **2011**, *4*, 4423.

(221) Biesheuvel, P.; van der Wal, A. Membrane capacitive deionization.*Journal of Membrane Science* **2010**, *346*, 256–262.

(222) Elabd, Y. A.; Hickner, M. A. Block Copolymers for Fuel Cells.*Macromolecules* **2011**, *44*, 1–11.

(223) Arges, C. G.; Kambe, Y.; Dolejsi, M.; Wu, G.-P.; Segal-Pertz, T.; Ren, J.; Cao, C.; Craig, G. S. W.; Nealey, P. F. Interconnected ionic domains enhance conductivity in microphase separated block copolymer electrolytes.*Journal of Materials Chemistry A* **2017**, *5*, 5619–5629.

(224) Geise, G. M. Experimental characterization of polymeric membranes for selective ion transport.*Current Opinion in Chemical Engineering* **2020**, *28*, 36–42.

(225) Guzmán-Garcia, A. G.; Pintauro, P. N.; Verbrugge, M. W.; Hill, R. F. Development of a space-charge transport model for ion-exchange membranes.*AIChE Journal* **1990**, *36*, 1061–1074.

(226) Yang, Y.; Pintauro, P. N. Multicomponent Space-Charge Transport Model for Ion-Exchange Membranes with Variable Pore Properties.*Industrial & Engineering Chemistry Research* **2004**, *43*, 2957–2965.

(227) Kamcev, J.; Sujanani, R.; Jang, E.-S.; Yan, N.; Moe, N.; Paul, D. R.; Freeman, B. D. Salt concentration dependence of ionic conductivity in ion exchange membranes.*Journal of Membrane Science* **2018**, *547*, 123–133.

(228) Kambe, Y.; Arges, C. G.; Czaplewski, D. A.; Dolejsi, M.; Krishnan, S.; Stoykovich, M. P.; de Pablo, J. J.; Nealey, P. F. Role of Defects in Ion Transport in Block Copolymer Electrolytes.*Nano Letters* **2019**, *19*, 4684–4691.

(229) Ryckaert, J.-P.; Ciccotti, G.; Berendsen, H. J. Numerical integration of the cartesian equations of motion of a system with constraints: molecular dynamics of n-alkanes. *Journal of Computational Physics* **1977**, *23*, 327–341.

(230) Jorgensen, W. L.; Chandrasekhar, J.; Madura, J. D.; Impey, R. W.; Klein, M. L. Comparison of simple potential functions for simulating liquid water. *The Journal of Chemical Physics* **1983**, *79*, 926–935.

(231) Sugita, Y.; Okamoto, Y. Replica-exchange molecular dynamics method for protein folding. *Chemical Physics Letters* **1999**, *314*, 141–151.

(232) Mahoney, M. W.; Jorgensen, W. L. A five-site model for liquid water and the reproduction of the density anomaly by rigid, nonpolarizable potential functions. *The Journal of Chemical Physics* **2000**, *112*, 8910–8922.

(233) Opekar, F.; Stulik, K. Electrochemical sensors with solid polymer electrolytes. *Analytica Chimica Acta* **1999**, *385*, 151–162.

(234) *Ion Exchange Membranes*; Royal Society of Chemistry: 2007.

(235) Su, X.; Tan, K.-J.; Elbert, J.; Rüttiger, C.; Gallei, M.; Jamison, T. F.; Hatton, T. A. Asymmetric Faradaic systems for selective electrochemical separations. *Energy & Environmental Science* **2017**, *10*, 1272–1283.

(236) Shukur, M.; Sonsudin, F.; Yahya, R.; Ahmad, Z.; Ithnin, R.; Kadir, M. Electrical Properties of Starch Based Silver Ion Conducting Solid Biopolymer Electrolyte. *Advanced Materials Research* **2013**, *701*, 120–124.

(237) Elabd, Y. A.; Walker, C. W.; Beyer, F. L. Triblock copolymer ionomer membranes. *Journal of Membrane Science* **2004**, *231*, 181–188.

(238) Arges, C. G.; Parrondo, J.; Johnson, G.; Nadhan, A.; Ramani, V. Assessing the influence of different cation chemistries on ionic conductivity and alkaline stability of anion exchange membranes. *Journal of Materials Chemistry* **2012**, *22*, 3733.

(239) Park, M. J.; Balsara, N. P. Anisotropic Proton Conduction in Aligned Block Copolymer Electrolyte Membranes at Equilibrium with Humid Air. *Macromolecules* **2010**, *43*, 292–298.

(240) Park, M. J.; Downing, K. H.; Jackson, A.; Gomez, E. D.; Minor, A. M.; Cookson, D.; Weber, A. Z.; Balsara, N. P. Increased Water Retention in Polymer Electrolyte Membranes at Elevated Temperatures Assisted by Capillary Condensation. *Nano Letters* **2007**, *7*, 3547–3552.

(241) Stoykovich, M. P.; Nealey, P. F. Block copolymers and conventional lithography.*Materials Today* **2006**, *9*, 20–29.

(242) Cummins, C.; Ghoshal, T.; Holmes, J. D.; Morris, M. A. Strategies for Inorganic Incorporation using Neat Block Copolymer Thin Films for Etch Mask Function and Nanotechnological Application.*Advanced Materials* **2016**, *28*, 5586–5618.

(243) Cruz-Chu, E. R.; Aksimentiev, A.; Schulten, K. Water-Silica Force Field for Simulating Nanodevices.*The Journal of Physical Chemistry B* **2006**, *110*, 21497–21508.

(244) Park, K.; Lin, W.; Paesani, F. A Refined MS-EVB Model for Proton Transport in Aqueous Environments.*The Journal of Physical Chemistry B* **2011**, *116*, 343–352.

(245) Vazdar, M.; Pluhařová, E.; Mason, P. E.; Vácha, R.; Jungwirth, P. Ions at Hydrophobic Aqueous Interfaces: Molecular Dynamics with Effective Polarization.*The Journal of Physical Chemistry Letters* **2012**, *3*, 2087–2091.

(246) Leontyev, I.; Stuchebrukhov, A. Accounting for electronic polarization in non-polarizable force fields.*Physical Chemistry Chemical Physics* **2011**, *13*, 2613.

(247) Liao, Q.; Fu, J.; Jin, X. Single-Chain Polystyrene Particles Adsorbed on the Silicon Surface: A Molecular Dynamics Simulation.*Langmuir* **1999**, *15*, 7795–7801.

(248) Wu, Y.; Chen, H.; Wang, F.; Paesani, F.; Voth, G. A. An Improved Multistate Empirical Valence Bond Model for Aqueous Proton Solvation and Transport†.*The Journal of Physical Chemistry B* **2008**, *112*, 467–482.

(249) Savoie, B. M.; Webb, M. A.; Miller, T. F. Enhancing Cation Diffusion and Suppressing Anion Diffusion via Lewis-Acidic Polymer Electrolytes.*The Journal of Physical Chemistry Letters* **2017**, *8*, 641–646.

Vita

Ke Li received his Bachelor of Science degree with a major of chemistry from Lanzhou University in 2015. After graduation, he went to the United States of America to pursue a doctorate degree in physical chemistry in Louisiana State University. He decided to join Dr. Revati Kumar's research group after the new graduate students lab rotation. During his doctoral program, he focused on studying battery electrolytes via molecular dynamics simulations. He plans to graduate with his Ph.D. degree in Fall 2020.